DOCTORAL THESIS

Experimental and Numerical Investigation of Spray-Control Appendages on Low-Planing Hard-Chine Hulls

Mikloš Lakatoš

TALLINNA TEHNIKAÜLIKOOL
TALLINN UNIVERSITY OF TECHNOLOGY
TALLINN 2026

TALLINN UNIVERSITY OF TECHNOLOGY
DOCTORAL THESIS
74/2026

Experimental and Numerical Investigation of Spray-Control Appendages on Low-Planing Hard-Chine Hulls

MIKLOŠ LAKATOŠ

TAL TECH PRESS

TALLINN UNIVERSITY OF TECHNOLOGY
School of Engineering
Department of Civil Engineering and Architecture
This dissertation was accepted for the defence of the degree 29/10/2026

Supervisor: Tenured Full Professor Kristjan Tabri
Department of Civil Engineering and Architecture
Tallinn University of Technology
Tallinn, Estonia

Opponents: Associate Professor Ermina Begovic
Department of Industrial Engineering
University of Naples Federico II
Naples, Italy

Associate Scientist Ashok Kumar
Centre for Naval Architecture, Ocean and Marine Engineering (NAOME)
Cyprus Marine and Maritime Institute (CMMI)
Larnaca, Cyprus

Defence of the thesis: 30/11/2026, Tallinn

Declaration:
Hereby I declare that this doctoral thesis, my original investigation and achievement, submitted for the doctoral degree at Tallinn University of Technology has not been submitted for doctoral or equivalent academic degree.

Mikloš Lakatoš

---
signature

Copyright: Mikloš Lakatoš, 2026
ISSN 2585-6898 (paperback)
ISBN 978-9916-80-590-9 (paperback)
ISSN 2585-6901 (PDF)
ISBN 978-9916-80-586-2 (PDF)
https://doi.org/10.23658/taltech.74/2026
Printed by Koopia Niini & Rauam

Lakatoš, M. (2026). *Experimental and Numerical Investigation of Spray-Control Appendages on Low-Planing Hard-Chine Hulls* [TalTech Press]. https://doi.org/10.23658/taltech.74/2026

TALLINNA TEHNIKAÜLIKOOL
DOKTORITÖÖ
74/2026

Pritsmeliistude eksperimentaalne ja numbriline uurimine aeglaselt glisseerivatel teravkimmilistel laevakeredel

MIKLOŠ LAKATOŠ

TAL TECH
KIRJASTUS

Contents

Contents 5
List of Publications 6
Author's Contribution to the Publications 7
Abbreviations 8
Symbols 8
1 Introduction 10
1.1 Spray rails 11
1.2 Chine strips 13
1.3 V-shaped spray interceptors 13
1.4 Numerical modelling of planing hulls 14
1.5 Problem statement (Research questions) 15
1.6 Scope 16
1.7 Limitations 17
1.8 Original features 17
2 Experimental study: MARTE spray rail test series 18
2.1 Experimental Series 18
2.1.1 Spray Rails (SR) 19
2.1.2 Chine strips (CS) 19
2.1.3 V-shaped spray interceptors (VSI) 20
2.2 Laboratory instrumentation and measurement 21
2.3 Experimental results 22
2.3.1 Spray rails 23
2.3.2 Chine strips 25
2.3.3 V-shaped spray interceptors 27
3 Numerical study 28
3.1 Numerical model 28
3.2 Verification & validation methodology 32
3.3 Verification and validation on the bare hull 32
3.4 Application of the numerical models to appended hull configurations 38
4 Conclusions 42
References 45
Acknowledgements 48
Abstract 49
Lühikokkuvõte 50
Appendix 1 51
Appendix 2 63
Appendix 3 85
Curriculum vitae 109
Elulookirjeldus 110

List of Publications

The list of author's publications, based on which the thesis has been prepared:

P1 Lakatos, M., Sahk, T., Kaarma, R., Tabri, K., Kõrgesaar, M., & Andreasson, H. (2019). Experimental testing of spray rails for the resistance reduction of planing crafts. In J. Puranov, & C. Guedes Soares (Ed.), Trends in the Analysis and Design of Marine Structures (pp. 334-343). London: Taylor & Francis Group. https://www.taylorfrancis.com/chapters/edit/10.1201/9780429298875-39/

P2 Lakatoš, M.; Sahk, T.; Andreasson, H. J. S.; Tabri, K. (2022). The effect of spray rails, chine strips and V-shaped spray interceptors on the performance of low planing high-speed craft in calm water. Applied Ocean Research, 122, 1−20. https://doi.org/10.1016/j.apor.2022.103131

P3 M. Lakatos, S. Mancini, R. Niazmand Bilandi, K. Tabri, (2025), Verification and Validation of Hard-Chine Hull Performance in Calm Water: Effects of Numerical Setups and Hull Configurations. Ocean Engineering. 329. https://doi.org/10.1016/j.oceaneng.2025.121056

Copies of the publications constituting the thesis are included in the appendix and marked in the text in [P1] – [P3] as presented above.

Other closely related publications:

P4 M. Lakatoš, K. Tabri, A. Dashtimanesh, H. Andreasson, (2020). Numerical Modelling of a Planing Craft with a V-Shaped Spray Interceptor Arrangement in Calm Water, in: E. Begovic (Ed.), 12th Symp. High Speed Mar. Veh. HSMV 2020, IOS Press, 2020: pp. 33–42. https://ebooks.iospress.nl/doi/10.3233/PMST200024.

P5 M. Lakatos, T. Sahk, H. Andreasson, K. Tabri, (2020). RESISTANCE TESTS OF A SERIES OF CHINE INTERCEPTORS ON A PLANING, in: Int. Conf. High Speed Vessel. 1st-2nd July 2020, The Royal Institution of Naval Architects, London, 2020: pp. 63–70.

Author's Contribution to the Publications

Contribution to the papers in this thesis are:

P1 **Mikloš Lakatoš**: Conceptualization, Investigation, Validation, Formal analysis, Visualization, Writing – original draft. **Tarmo Sahk**: Methodology, Investigation, Software, Data curation. **Risto Kaarma**: Formal analysis. **Henrik Andreasson**: Conceptualization, Methodology, Writing – review & editing. **Kristjan Tabri**: Supervision, Project administration, Funding acquisition, Writing – review & editing. **Mihkel Kõrgesaar**. Visualization, Writing – review & editing.

P2 **Mikloš Lakatoš**: Conceptualization, Investigation, Validation, Formal analysis, Visualization, Writing – original draft. **Tarmo Sahk**: Methodology, Investigation, Software, Data curation. **Henrik Andreasson**: Conceptualization, Methodology, Writing – review & editing. **Kristjan Tabri**: Supervision, Project administration, Funding acquisition, Writing – review & editing.

P3 **Mikloš Lakatoš**: Writing – original draft, Visualization, Validation, Methodology, Investigation, Formal analysis, Conceptualization. **Simone Mancini**: Writing – review & editing, Writing – original draft, Validation, Methodology, Formal analysis. **Rasul Niazmand Bilandi**: Writing – review & editing, Writing – original draft. **Kristjan Tabri**: Writing – review & editing, Supervision, Project administration, Funding acquisition, Conceptualization.

P4 **Mikloš Lakatoš**: Conceptualization, Investigation, Validation, Formal analysis, Visualization, Writing – original draft. **Abbas Dashtimanesh**: Writing – review & editing. **Henrik Andreasson**: Conceptualization, Methodology, Writing – review & editing. **Kristjan Tabri**: Supervision, Project administration, Funding acquisition, Writing – review & editing.

P5 **Mikloš Lakatoš**: Conceptualization, Investigation, Validation, Formal analysis, Visualization, Writing – original draft. **Tarmo Sahk**: Methodology, Investigation, Software, Data curation. **Henrik Andreasson**: Conceptualization, Methodology, Writing – review & editing. **Kristjan Tabri**: Supervision, Project administration, Funding acquisition, Writing – review & editing.

Abbreviations

AMR	Adaptive Mesh Refinement
BH	Bare Hull
C.INC	Chine inclination
CF	Correction Factor method
CFD	Computational Fluid Dynamics
CFL	Courant-Friedrichs-Lewy number
CG	Centre of Gravity
Con	Conventional spray rail profile
CSI	Chine spray interceptor
CSR	Chine spray rail
DFBI	Dynamic Fluid Body Interaction
EFD	Experimental Fluid Dynamics
GCI	Grid Convergence Index Method
HRIC	High-Resolution Interface Capturing
ITTC	International Towing tank Conference
LSR	Least Squares Root
MMP	Mixture Multiphase
NV	Numerical Ventilation
PMM	Planar Motion Mechanism
RANSE	Reynolds-averaged Navier–Stokes equations
RE	Richardson Extrapolation
Rec	Rectangular Spray rail profile
SR	Spray rail arrangement
Tri	Triangular Spray Rail profile
V&V	Verification and Validation
VOF	Volume of Fluid
VSI	V-Shaped Spray Interceptor

Symbols

b	Wetted half-width (m)
b_1	Actual wetted half-width (m)
b_{SR}	Width of the spray rail (m)
b_{CS}	Width of the chine strip (m)
B_{CT}	Chine beam at the transom
B_{OA}	Beam overall (m)
B_{WL}	Beam waterline (m)
BS	Base Size (m)
d	Parallel normal distance from stagnation line to VSI (m)
Fr	Froude number (-)
Fr_∇	Froude displacement number (-)

E	Comparison error (%)
KG	Vertical Centre of Gravity (m)
L_{CG}	Longitudinal Centre of Gravity (m)
L_{OA}	Length overall (m)
L_{PP}	Length between perpendiculars (m)
L_{WL}	Length waterline (m)
p_k	Estimated order of accuracy (-)
$p_{k\mathrm{th}}$	Theoretical order of accuracy (-)
R_k	Convergence ratio (-)
R_{TM}	Total resistance in model scale (N)
S_{WB}	Wetted bottom area, underway (m^2)
S_{WHE}	Wetted hull area, underway (m^2)
S_{WS}	Area wetted by Spray (m^2)
S_U	Maximum value for simulation result
S_L	Minimum value for simulation result
T	Draught (m)
U	Uncertainty
U_{SN}	Simulation uncertainty
U_{D}	Experimental data uncertainty
U_{V}	Validation uncertainty
U_{G}	Grid uncertainty
U_{I}	Iteration uncertainty
U_{TS}	Time-step uncertainty
V_{Hull}	Hull velocity (m/s)
z_{VCG}	Dynamic sinkage at CG (m)
β_T	Deadrise angle at the transom (deg)
$\beta_{0.5}$	Deadrise angle at 50% L_{DWL} (deg)
$\beta_{0.75}$	Deadrise angle at 75% L_{DWL} (deg)
δ	Bottom angle of the spray rail (deg); the thickness of the spray sheet (m)
δ_{SM}	Modelling error
δ_{SN}	Simulation error
Δt	Time step (s)
Δx	Cell size (m)
ε	Solution change
τ	Dynamic trim (deg)
∇	Displacement Volume (m3)
Ⓜ	Length-displacement ratio Ⓜ $= \frac{L_{WL}}{\sqrt[3]{\nabla}}$

1 Introduction

High-speed planing craft play an increasingly important role in both civilian and military maritime operations, where efficiency, stability, and seakeeping are critical. At high Froude numbers, planing hulls experience complex free-surface phenomena, including spray formation, ventilation, and dynamic instabilities, which strongly influence lift, trim, and resistance. Among the design features that affect these hydrodynamic characteristics, spray-control appendages—particularly spray rails, chine strips, and V-shaped spray interceptors—are known to have a significant influence on resistance and the running attitude of the craft.

Despite this, systematic studies examining the number, position, and geometry of spray rails on fully planing hulls remain limited. Prior research predominantly focused on semi-displacement vessels, where spray behaviour and flow regimes differ significantly from those of planing craft. Consequently, there is limited systematic experimental and validated numerical data for spray-control appendages operating on hard-chine hulls in the low- to moderate-planing regime, particularly under off-design loading conditions. This forms the focus of this dissertation.

This thesis addresses this gap through a combined experimental and numerical investigation (Figure 1) of a hard-chine planing hull equipped with spray rails, chine strips or V-shaped spray interceptors (VSIs). The experimental programme comprised towing-tank tests at multiple draughts, including off-design loading conditions, to quantify the effects of the investigated appendages on resistance and the running attitude of the craft. These measurements provide a robust empirical baseline for evaluating the hydrodynamic performance of different appendage configurations and for validating computational models. The numerical analysis employed Reynolds-averaged Navier–Stokes (RANS) equations with a Volume of Fluid (VOF) free-surface method, implemented in STAR-CCM+. Both two-degree-of-freedom (2DOF) and three-degree-of-freedom (3DOF) simulations were conducted to capture the dynamic equilibrium of the hull and investigate the sensitivity of predictions to motion definition. Verification and validation procedures were conducted in accordance with ITTC guidelines.

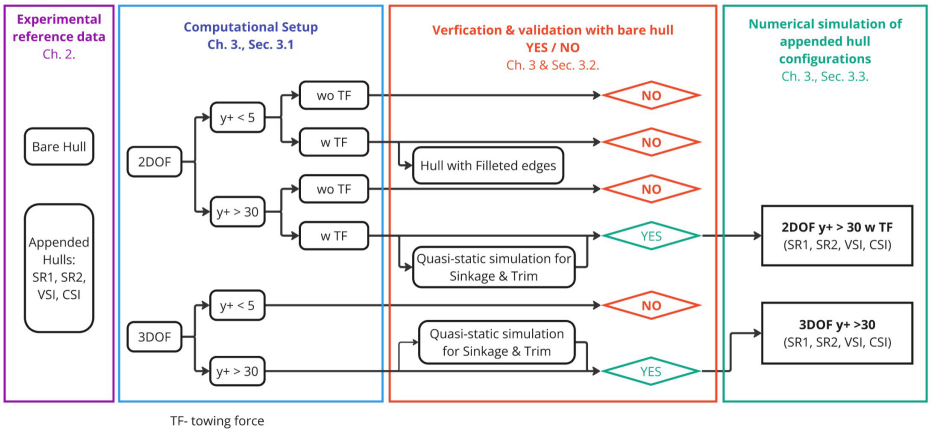

Figure 1. Flow chart of the investigation outlining the numerical modelling strategy, comprising motion configuration (2DOF and 3DOF), towing force (TF), and near-wall treatment ($y^+ < 5$ and $y^+ > 30$).

During the initial Computational Fluid Dynamics (CFD) validation, it became evident that the numerical model systematically underestimated trim and resistance relative to experimental measurements. This discrepancy highlighted the need to critically examine sources of error in the CFD setup, including turbulence modelling, wall treatment, mesh resolution, and the representation of degrees of freedom. As a result, the focus of the research shifted from merely evaluating appendage effects to a combined experimental–numerical study aimed at improving CFD predictive accuracy for planing hulls. This approach ensures that subsequent analyses and design recommendations are based on validated and reliable computational results.

The scientific novelty of this work lies in its integrated approach. It provides a systematic assessment of spray rail effects on planing hulls under multiple draught conditions, combining experimental and numerical investigations within a rigorous validation framework. The study also quantifies the influence of chine strips and V-shaped spray interceptors (VSIs) on hydrodynamic performance, offering insight into the mechanisms by which spray-control appendages affect resistance and running attitude. Moreover, the research contributes to understanding the limitations of conventional CFD methods for planing hulls and establishes guidelines for achieving reliable predictions, which is critical for both academic research and practical design applications.

The findings of this study are directly relevant to the Estonian high-speed marine vehicle (HSMV) sector, in which accurate prediction of vessel performance is essential for informed design decisions and optimisation. In recent years, Estonia has also developed unmanned surface vehicles (USV), or drones, for maritime surveillance and monitoring operations. The performance of these platforms—particularly speed, range, and onboard sensor functionality—is strongly influenced by hull hydrodynamics. Improved spray rail configurations can reduce resistance, increase speed and range, and mitigate vertical accelerations and motion amplitudes. These improvements enhance seakeeping, improve the performance of surveillance equipment, and contribute to safer, more effective operation. Beyond direct design benefits, the study strengthens national competence in experimental and numerical marine hydrodynamics, providing a foundation for future research and development.

The research findings have been documented through a series of publications. Preliminary experimental and numerical results on spray rails, chine strips, and VSIs were presented in P1, P4, and P5, providing the empirical foundation for the study. Integrated experimental and numerical investigations were later published in P2 and P3. Together, these publications establish the validated dataset and methodologies as schematically illustrated in Figure 1.

The following sections present a review of the current state of the art in spray-control appendages applied to planing hulls, with particular emphasis on spray rails, chine strips, and V-shaped spray interceptors. These sections summarise the established physical mechanisms, reported performance trends, and commonly cited design approaches for these devices, while identifying limitations in the available experimental and numerical literature. These identified gaps motivate the experimental programme and numerical investigations undertaken in this thesis.

1.1 Spray rails

Spray rails are structural elements commonly used on the hulls of high-speed marine vehicles, including semi-displacement and planing craft, as well as hydroplanes. Their main function is to detach spray from the hull surface and deflect it down and aft at semi-

displacement and planing speed. Spray is formed in the vicinity of the stagnation line (Figure 2), where the flow on the hull bottom is divided into forward- and aft-directed components and local pressure reaches a maximum (Savitsky & Morabito, 2011). The wetted bottom aft of the stagnation line is commonly referred to as the "*pressure area*", while the wetted bottom forward of it is referred to as the "*spray area*". Within the spray area, the direction of the fluid is such that the streamlines are nearly a reflection of the free stream about the stagnation line. As the spray sheet travels from the stagnation line across the bottom towards the chine, viscous forces are generated with an aft-directed component, contributing to the total resistance of the craft (Savitsky & Morabito, 2011).

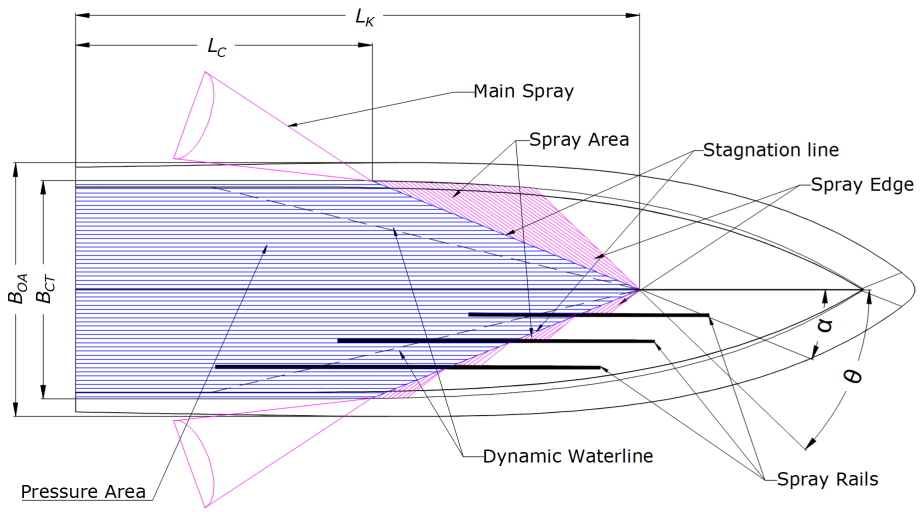

Figure 2. Principal characteristics of spray formation on a planing hull with and without spray rails.

Spray rails may be aligned with hull buttocks, waterlines, or diagonally, and their geometry is commonly characterised by their longitudinal extent l_{SR}, transverse width b_{SR} and bottom angle δ. Existing studies suggest that spray rails should be narrow in the forebody and inclined upwards rather than downwards, with typical proportions of $b_{SR} = 0.0055L_{WL}$ and $\delta \cong 8°$ (Larsson et al., 2014; Müller-Graf, 1991; Savitsky et al., 2007). It has been further recommended that spray rails be limited by the spray edge and the stagnation line or extend only slightly aft of it (Clement, 1964a). An exception is commonly noted when the stagnation line reaches the transom, in which case extending the outer spray rail may be beneficial for preventing chine walking (Larsson et al., 2014). To promote clean flow separation, the outer edge of the spray rail should be as sharp as practicable (Clement, 1964a; Savitsky et al., 2007), while the inner edge should be smoothly blended into the hull surface to avoid increases in resistance (Larsson et al., 2014).

Although whisker spray was recognised in the original Savitsky method (Savitsky, 1964), it was not explicitly accounted for until the introduction of an analytical model (Savitsky et al., 2007). The model indicated that depending on the speed and hull geometry, whisker spray may account for approximately 3–15% of total resistance.

Earlier studies have shown that spray rails can reduce total resistance by 6–25% when Froude displacement number Fr_∇ > 3.5 (Clement, 1964a, 1964b; Grigoropoulos & Loukakis, 1995). However, at displacement and semi-displacement speeds (Fr_∇ < 3), the spray rails may increase the resistance by 3% (Clement, 1964a). This is because, at low

speeds, spray rails increase lift in the forebody, which leads to an increase in running trim and total resistance, thereby negating the benefits of spray deflection (Clement, 1964a).

A more recent experimental investigation (Begovic & Bertorello, 2012) examined the wetted surface (pressure and spray area) of hard chine planing hulls using transparent bottoms across a range of $Fr_\nabla = 0.650 – 4.518$. By analysing the measured pressure and spray areas and applying Savitsky's resistance breakdown procedure (Savitsky et al., 2007), the authors reported spray-related resistance contributions of up to 6–12% of the total resistance at planing speeds $Fr_\nabla > 3$. However, at semi-displacement and low planing speeds, spray accounted for approximately 3%.

At lower speeds, higher running trim angles increase the stagnation line angle α and, consequently, the spray edge angle ($\theta \approx 2\alpha$). This results in a more transverse orientation of the spray flow relative to the hull. While the spray area increases under these conditions, the longitudinal component of the viscous force associated with the spray is reduced. Consequently, the contribution of whisker spray to the total resistance remains limited at low speeds.

Despite the widespread practical use, spray rails remain insufficiently characterised at low and moderate planing speeds. Consequently, the influence of key geometric parameters—including length, width, and bottom angle—on resistance and running attitude has not been systematically quantified for $Fr_\nabla \leq 3.3$, and existing design guidance remains predominantly qualitative.

1.2 Chine strips

Chine strips act similarly to stern interceptors (Avci & Barlas, 2019; De Luca & Pensa, 2012; Karimi et al., 2013; Mansoori et al., 2017; Mansoori & Fernandes, 2017; Park et al., 2019; Seok et al., 2020) by redirecting the spray flow nearly perpendicular to the hull surface at the chine–stagnation line intersection. This redirection increases dynamic lift, moves the centre of pressure aft, and consequently lowers the running trim and resistance.

Early investigations into chine strips are limited and predate most systematic research on spray control. Kapryan and Boyd (1953) examined the effect of vertical chine strips on two prismatic V-shaped hulls with deadrise angles of 20° and 40° (Chambliss & Boyd, 1953). Their findings were compared with tests on horizontal chine flares performed by Blanchard (1952) and by Kapryan & Weinstein (1952). All tests were conducted under captive conditions, meaning that the hull attitude was fixed. The results showed that vertical strips produced significantly greater lift enhancement than horizontal flares.

When combined with horizontal flares, chine strips form a chine configuration that may be regarded as functionally analogous to a transom interceptor arrangement, producing a sharp deflection of spray at the chine, increasing lift, and shifting the pressure distribution aft. Despite being recognized in practical naval design, systematic investigations of this configuration remain scarce. To the best of the author's knowledge, the studies conducted in the 1950s constitute the only dedicated investigations of the chine strips. As a result, their effect on resistance and running attitude remains insufficiently quantified.

1.3 V-shaped spray interceptors

V-shaped spray interceptors (VSIs), also referred to as spray deflectors, are innovative hydrodynamic devices designed to reduce drag on planing hulls by redirecting spray flow.

Positioned ahead of and aligned with the stagnation line, VSIs utilize the momentum of the spray to generate a forward-directed reaction force, thereby decreasing overall hull resistance. Multiple studies—including those by Castaldi et al. (2021), Molchanov et al. (2019), and Olin et al. (2016)—have investigated various VSI configurations, often mounted similarly to conventional spray rails.

In a numerical study, Olin et al. (2016) demonstrated that at high planing speeds (Fr_∇ = 6.24), VSIs reduced total resistance by up to 30% compared to a bare hull. Notably, only 4% of this reduction was attributed to the reaction force from spray deflection; the majority resulted from a decrease in spray area.

Molchanov et al. (2019) conducted experimental tests comparing two VSI designs—optimized for Fr_∇ values of 4.3 and 5.87—with traditional spray rails across a speed range of Fr_∇ = 3.5–6.65, in both calm water and irregular wave conditions. Their findings showed that while conventional spray rails reduced resistance by up to 9%, the VSI configurations achieved reductions ranging from 14.5% to 25%.

Further experimental work by Castaldi et al. (2021) evaluated three VSI setups tailored for Fr_∇ values of 3.65, 4.56, and 5.48. Across a planing speed range of Fr_∇ = 2.97–5.93, the VSIs reduced resistance by 1.5% to 2.5% at their design speeds, with peak reductions of up to 5% at lower speeds. The study also highlighted the importance of the distance between the stagnation line and the VSI, noting that increased separation enhances spray deflection efficiency.

Despite extensive research on the V-shaped spray interceptors (VSI), existing studies have largely focused on arrangements for high Froude displacement numbers ($Fr_\nabla \geq$ 3.65), where spray area reduction dominates the hydrodynamic effect. At lower planing speeds, the stagnation line shifts markedly with speed and displacement. Consequently, the performance and governing mechanisms of VSI arrangements designed for low planing speeds ($Fr_\nabla <$ 3.65) cannot be inferred reliably from existing literature and remain insufficiently understood.

1.4 Numerical modelling of planing hulls

Since planing involves significant changes in the running attitude of the craft, numerical simulation of this phenomenon requires employing more complex models such as the overset or the morphing mesh. However, it is established that CFD simulations of planing hulls tend to underestimate total resistance by up to 10% (Cui et al., 2021) or even 20% (Tavakoli et al., 2024). Therefore, naval architects rely primarily on model tests that are both time-consuming and resource intensive. In contrast, numerical simulations require significantly fewer resources and enable a significantly faster and more elaborate analysis of phenomena such as pressure distribution, centre of pressure, shear stress, and wetted area, which are challenging to evaluate experimentally. Several reasons have been suggested to account for the disparities between the numerical simulations and physical model tests. More specifically, three main reasons can be identified.

First, the variations in the geometry between the hull model tested and the one employed in simulations play a crucial role (Judge et al., 2020). Idealised 3D models used in numerical simulations have sharp edges, which can lead to more lift and less resistance. The real physical models used in model tests may appear to have sharp edges; however, their edges are rounded with radii typically ranging from 1–3 mm. Judge et al. (2020) reported the difference between simulations of hulls with sharp edges compared to those with rounded edges was about 1% in resistance. However, the sensitivity of

resistance and running attitude predictions to geometric fidelity has not been quantified for low-planing regimes ($Fr_\nabla < 3.65$).

Second, uncertainties in model ballasting and the positioning of the towing point and the centre of buoyancy may contribute to the differences in both resistance and running attitude (De Luca et al., 2014; Judge et al., 2020). Therefore, static equilibrium conditions should ideally be assessed prior to simulation, to evaluate initial biases in trim and sinkage.

Third, the lack of a trimming moment resulting from the towing force has been overlooked (De Luca et al., 2014). Commonly, resistance simulations employ a two-degree-of-freedom (2DOF) approach, where the hull is free to pitch and heave while the computational domain remains stationary and water flows through it at the prescribed velocity. An alternative approach proposed by Wheeler et al. (2021) prescribes the surge motion in addition to allowing heave and pitch and is referred to as a three-degree-of-freedom (3DOF) approach. In this formulation, surge is prescribed through movement of the computational domain (far-field and overset regions) relative to stationary water. This simplifies velocity specification and avoids wave generation associated with gradually accelerating the inflow in conventional 2-DOF simulations. The extent to which explicit modelling of the towing force improves agreement between CFD predictions and towing tank measurements remains insufficiently quantified, particularly for resistance and running-attitude predictions.

Furthermore, most studies employ wall functions (wall $y^+ > 30$) for the wall treatment since this requires fewer prism layers (6–9) compared to the models that solve the viscous sublayer directly (wall $y^+ < 5$) which require approximately 15 prism layers. Since the number of prism layers and therefore the cell count is smaller, the wall function approach is significantly less computationally demanding. However, direct, systematic comparisons of these wall-treatment approaches on a single hull configuration are limited, and their influence on the prediction accuracy remains insufficiently characterised.

Finally, it remains uncertain whether a comparative CFD study conducted during the early design phase would lead the designer to conclusions consistent with those derived from experimental results, or whether it could potentially misguide the design process. In particular, the ability of CFD to reliably capture experimentally observed differences between hull configurations under varying conditions remains an open question, especially at low to moderate planing speeds.

Taken together, previous studies have identified several modelling sensitivities in CFD simulations of planing hulls, including geometric representation, equilibrium conditions, towing force representation, and near-wall treatment. However, systematic evaluations of the influence of these modelling choices on a single hull configuration remain limited. These uncertainties are particularly relevant to the assessment of spray-control appendages, whose hydrodynamic effects are closely linked to changes in pressure distribution, spray formation, and running attitude. Consequently, key aspects governing the predictive accuracy of CFD for resistance and running attitude remain insufficiently clarified.

1.5 Problem statement (Research questions)

Although spray-control appendages such as spray rails, chine strips, and V-shaped spray interceptors (VSI) are commonly used in the design of planing hulls, their hydrodynamic effects—particularly at lower Froude numbers—are not yet fully understood. Existing

literature provides only general guidance, and several critical aspects remain unexplored or insufficiently validated.

In particular, the influence of appendage geometry and arrangement on resistance and running attitude has not been systematically quantified on a common hull form at moderate planing speeds. At the same time, the ability of CFD to reproduce appendage-induced trends under these conditions has not been sufficiently validated for design-relevant application. To address these gaps, the present study is guided by the following research questions:

Q1 ***How do the geometry and arrangement of spray-control appendages affect the resistance and running attitude of a hard-chine planing hull at moderate planing speeds (Fr_∇ < 3.65)?***

Q2 ***Under which modelling assumptions can CFD reliably reproduce experimentally observed appendage-induced trends, and how can such validated simulations be applied for comparative design assessment of appended planing hulls?***

Together, these questions establish a coherent experimental–numerical framework in which experimentally derived physical understanding is used to evaluate the capabilities and limitations of CFD as a design-support tool.

1.6 Scope

To address the identified gaps in current knowledge, this study undertakes a combined experimental and numerical investigation into the hydrodynamic performance of spray rails, chine strips, and V-shaped spray interceptors (VSI) on hard-chine planing hulls operating at volumetric Froude numbers $Fr_\nabla < 3.3$. The scope of the work is divided into two primary components: a towing tank test series, aimed at empirically evaluating the effects of these appendages on resistance and running attitude, and a CFD simulation campaign, designed to analyse and validate their hydrodynamic behaviour under controlled numerical conditions.

The experimental programme is conducted to quantify the influence of spray rails, chine strips, and VSI on the hydrodynamic performance of the hull, with particular emphasis on total resistance and running attitude (trim and sinkage). Key geometric parameters, including spray rail width, bottom angle, and length, are systematically varied to assess their effects. In addition, the experimental results are compared with existing design guidelines to evaluate their applicability within the low-planing regime.

The numerical study complements the experimental work by simulating the hydrodynamic behaviour of the same configurations under calm water conditions. Particular attention is given to the sensitivity of CFD predictions to numerical and modelling choices, including near-wall treatment strategies ($y^+ < 5$ and $y^+ > 30$), the selection of degrees of freedom (comparing 2DOF simulations, in which towing-induced trimming moments may be imposed, with a 3DOF formulation), uncertainties in model ballasting and towing point location, and the representation of geometric fidelity through sharp and rounded hull features. Finally, CFD predictions are validated against experimental data to assess the reliability of numerical methods for application in early-stage hull design.

1.7 Limitations

The study is limited to calm-water hydrodynamic behaviour of a hard-chine hull operating across a transitional speed range from semi-displacement to planing conditions (Fr = 0.79–1.4; Fr_∇ = 1.742–3.261). While the vessel transitions into the planing regime within this interval, the upper range does not represent high-speed planing conditions.

The exclusive focus on calm water means that the influence of the investigated appendages on seakeeping behaviour, including added resistance in waves, vertical accelerations, and dynamic stability phenomena such as porpoising, is not assessed. The study further relies on model-scale experiments and corresponding CFD simulations. Although validated within the investigated range, scale effects associated with Reynolds number, spray formation, and free-surface scaling may affect extrapolation to full-scale conditions.

Within these constraints, the findings are valid for a hard-chine hull operating in calm water at model scale over the range Fr = 0.79–1.4 and Fr_∇ = 1.742–3.261. Outside this domain—particularly at higher planing speeds, full scale, or in waves—the results should be interpreted with caution.

1.8 Original features

This thesis contributes to the understanding and modelling of spray-control appendages (SCA) on hard-chine planing hulls through a combined experimental and numerical investigation. The principal original features are summarised as follows:

1. A towing tank test series for spray rails, chine strips, and V-shaped spray interceptors on a single hard-chine hull operating across the transition from semi-displacement to fully developed planing. The work provides a systematic and internally consistent benchmark dataset enabling direct comparison of appendage performance and serving as validation data for CFD simulations.

2. A comparative characterisation of appendage behaviour is established showing that appendage effects depend on their interaction with the hull's running attitude and wetted surface. Spray rails influence resistance predominantly through changes in trim, with associated variations in wetted surface playing a secondary role, whereas chine strips act predominantly through changes in trim. V-shaped spray interceptors act through a spray-induced hydrodynamic reaction force and a reduction in spray area, with limited influence on trim.

3. A comparative analysis of numerical approaches for planing hull modelling identifies near-wall treatment and towing-force representation as the primary factors governing predictive fidelity. The validated numerical models reproduce the principal experimental trends within validation uncertainty, while exhibiting limited sensitivity for quantitative comparison between configurations.

2 Experimental study: MARTE spray rail test series

This chapter describes the experimental investigation conducted to establish reference hydrodynamic data for a hard-chine planing hull equipped with spray-control appendages in calm water. The experimental programme provides systematic measurements of total resistance, running trim, and sinkage over a range of speeds and loading conditions representative of the low- to moderate-planing regime. These measurements form the experimental basis for subsequent analysis and for the verification and validation of the numerical models presented later in the thesis.

2.1 Experimental Series

The spray-control appendages were investigated on a purpose-built test-case vessel (Figure 2) designed by the Marine Technology Competence Centre (MARTE) of Tallinn University of Technology (TalTech). The hull dimensions (Table 1) are representative of a high-speed patrol, Search-And-Rescue (SAR) vessel, or a large pleasure boat, designed for operation at a Froude number of Fr=1.355 and a volumetric Froude number of Fr_{∇}=3.108, corresponding to a displacement of 40 t and a speed of 35 knots.

The test series comprised fifteen configurations: seven spray rails, seven chine strips and a V-shaped spray interceptor (VSI). Each configuration was assessed at four speeds and four loading conditions, in a speed range of Fr_{∇}=1.742–3.261 (Table 2). The geometries of the investigated spray rails, chine strips and the VSI are briefly outlined in the following sub-sections, with further details reported in P2.

Table 1. Main particulars of the reference bare hull under design loading condition.

Parameter	Symbol	Model scale	Full scale
Scale factor	λ	10	1
Length overall	L_{OA}	1.921 m	19.21 m
Length between perpendiculars	L_{PP}	1.800 m	18.00 m
Length waterline	L_{DWL}	1.703 m	17.03 m
Beam overall	B_{OA}	0.581 m	5.810 m
Chine beam at the transom	B_{CT}	0.500 m	5.000 m
Draught	T_{DWL}	0.108 m	1.080 m
Vertical centre of gravity	KG	0.200 m	2.000 m
Longitudinal centre of gravity	L_{CG}	0.670 m	6.700 m
Deadrise angle at the transom	β_T	19.92 °	19.92 °
Horizontal position of the towing point (from transom)	TPH	0.36 m	N.A.
Vertical position of the towing point (from keel)	TPV	0.09 m	N.A.

Table 2. Hydrostatic characteristics and speed ranges of the craft in tested loading conditions.

L_{WL} [m]	B_{WL} [m]	T [m]	Δ_m [kg]	∇ [m³]	L_{CG} [m]	Ⓜ	L_{WL}/B_{WL}	B_{WL}/T	L_{CG}/L_{WL}	V_{CG}/B_{WL}	Fr	Fr_{∇}
1.682	0.503	0.093	30	0.030	0.663	5.411	3.341	5.425	0.394	0.397	0.801–1.402	1.864–3.261
1.693	0.507	0.099	35	0.035	0.666	5.174	3.341	5.120	0.393	0.395	0.798–1.397	1.816–3.178
1.703	0.510	0.108	40	0.040	0.670	4.978	3.338	4.737	0.393	0.392	0.796–1.393	1.776–3.108
1.712	0.513	0.115	45	0.045	0.674	4.812	3.336	4.470	0.394	0.390	0.794–1.390	1.742–3.048

2.1.1 Spray Rails (SR)

Two configurations were tested: SR1, ending at the dynamic waterline, and SR2, extending to the transom (Figure 3a). Rails followed vertical hull buttocks for simplicity and relevance to planing in calm water. Alternatives like waterline or diagonal alignments, or extensions to the bow stem, were excluded as they remain dry at planing speeds.

The conventional profile (Figure 3b) had a flat bottom (δ = 0°), tapering from 8 mm aft to 5 mm forward due to hull curvature. To isolate the effects of width and bottom angle, rectangular (Figure 3c, d) and triangular (Figure 3e, f) profiles were tested. Widths increased from 2 mm to 5 mm. Bottom angles varied from δ = -25° to δ = -70°. The bottom angle δ is measured relative to the horizontal reference, with positive values denoting an upward-inclined, flatter deflection surface and negative values denoting a downward-inclined, sharper deflection surface.

Profile selection prioritized ease of manufacturing: conventional rails were 3D printed, while square and triangular profiles were commercially available in 2x2 mm and 5x5 mm sizes. All tested widths (b_{SR} = 0.1% – 0.3% of L_{WL}) were within Müller-Graf's (1991) recommended limit of 0.5% L_{WL}.

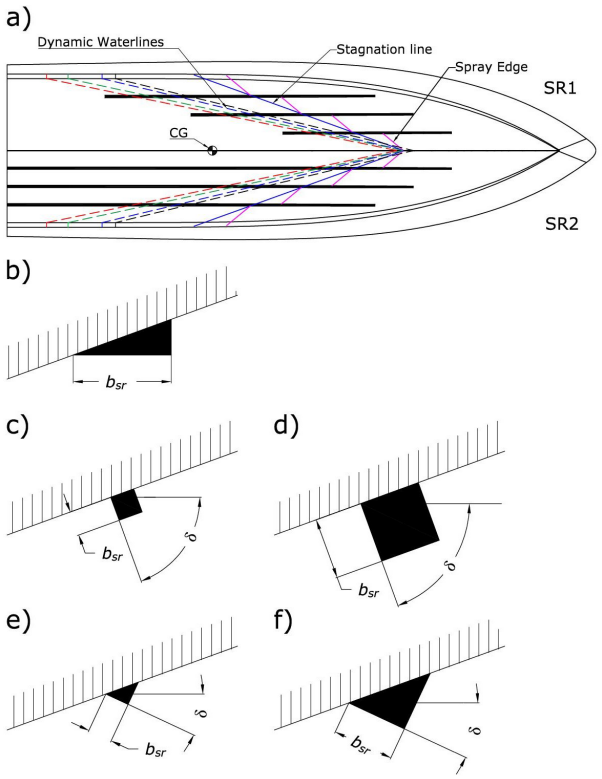

Figure 3. Tested spray rail configurations and shapes [P2].

2.1.2 Chine strips (CS)

Two hull setups were tested: bare hull (BH) and one with rectangular 5×5 mm spray rails limited by the dynamic waterline (SR1-Rec-5x5). First, the bare hull was fitted with an inclined chine (C.INC), i.e. the rails covered the whole chine (b_{CS} = 15 mm), resulting in a

new chine surface angled down by δ_{CS} = -8° (Figure 4a, f). Subsequently, the bare hull was fitted with rectangular (Figure 4b, c) and triangular (Figure 4d, e) chine strips. The rectangular strips (CSI1, CSI2) deflected spray at 90°, while triangular strips (CSR1, CSR2) deflected at 45°. Finally, the hull equipped with spray rails (SR1-Rec-5x5) was tested in combination with chine strips CSI1 (2×2 mm) and CSR2 (5×5 mm) (Figure 4b, e).

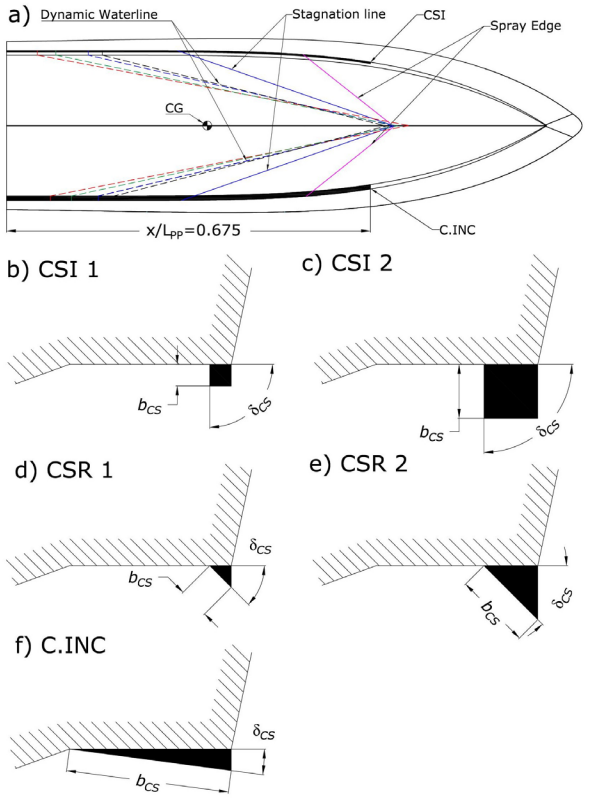

Figure 4. Tested chine strips [P2].

2.1.3 V-shaped spray interceptors (VSI)

The V-shaped spray interceptors (VSI) (Figure 5a) were designed for Ⓜ = 4.978, Fr = 1.393 and Fr_∇ = 3.108, equivalent to the craft's design displacement of Δ_{mS} = 40t and speed of V_S = 35 knots in full-scale. The position of the VSI was determined with reference to the dynamic waterlines of the bare hull, placing it slightly forward of the expected stagnation line.

To confirm that the VSI was tall enough, the spray sheet thickness δ was estimated following the Wagner's (1932) theoretical formulation, which has been shown to correlate well with numerical calculations by Olin et al. (2016). The spray-sheet thickness was estimated to vary within a range of δ = 1–5 mm. Accordingly, the VSI was modelled with triangular 5×5 mm profiles (Figure 5c), with deflection surfaces perpendicular to the hull to ensure full spray interception.

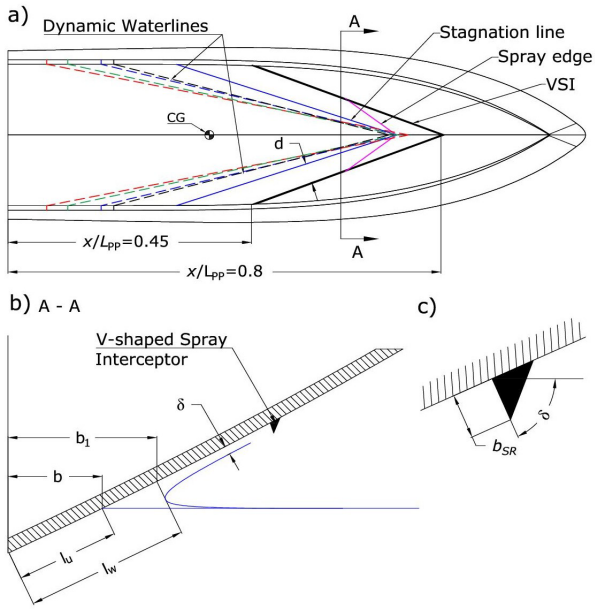

Figure 5. V-shaped spray interceptors [P2].

2.2 Laboratory instrumentation and measurement

Calm water towing tests were performed in the towing tank facility (Table 3) at the Marine Technology Competence Centre (MARTE) of Tallinn University of Technology (TalTech), in accordance with ITTC guideline 7.5-02-02-01 (ITTC, 2017a). The models were tested under semi-captive conditions, allowing freedom in pitch and heave motions (Figure 6).

During each test run, the total resistance R_{TM} and the vertical displacements at the fore and aft perpendiculars—denoted as z_{VF} and z_{VA}, respectively—were recorded at a sampling frequency of 200 Hz (Figure 7). The running trim angle τ was calculated using the measured values of as z_{VF} and z_{VA}. The number of repeated runs and the duration of data acquisition are detailed in Table 4. Further details on the calibration of the measurement equipment are provided in P2.

Table 3. Main dimensions of the MARTE towing tank.

Parameter		
Maximum tank length	*l*	60 m
Maximum tank breadth	*b*	5 m
Maximum tank depth	*h*	3 m
Maximum carriage speed	*V*	5.7 m/s

Table 4. Numbers of repeated runs and data acquisition times.

V_M [m/s]	No. of Repeated Runs	Data Acquisition Time [s]
3.254	2–4	9
4.067	2–4	6
4.880	2–5	4
5.694	2–6	3

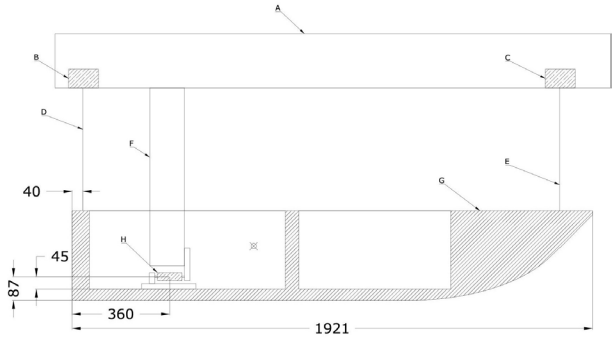

Figure 6. Semi-captive model test setup: A–carriage, B & C–wire encoder, D & E–linear measuring wire, F–carriage arm, G–test model, H–force gauge [P2].

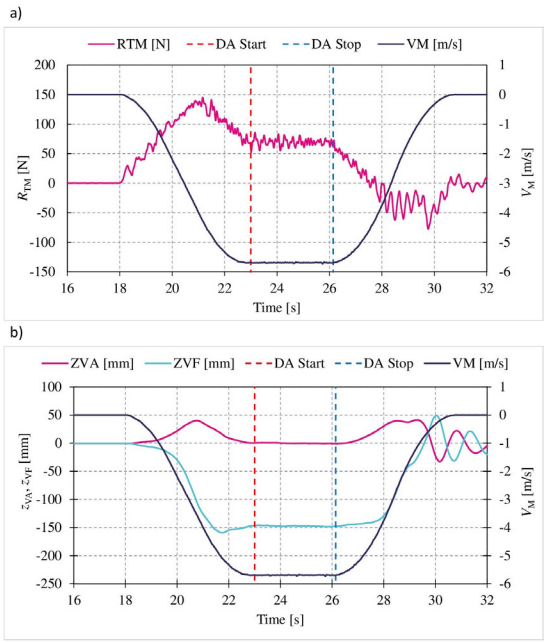

Figure 7. Time histories of data acquisition of measured quantities [P2]: a) resistance R_{TM} and speed V_M of the model, b) sinkage at the aft and the fore perpendiculars z_{VA} and z_{VF} and speed V_M of the model [P2].

2.3 Experimental results

This section presents the outcomes of the experimental campaign. Hulls equipped with spray rails, chine strips, or the VSI were compared to the bare hull using three nondimensional parameters: total resistance $\left(\frac{R_{TM}}{\Delta}\right)$, running trim (τ), and sinkage at the center of gravity $\left(\frac{z_{VCG}}{\nabla^{1/3}}\right)$. These results are summarized in P2 (Tables B.1–B.4), while baseline resistance and trim values for the unmodified hull are shown in Figure 8 with $\text{Ⓜ} = \frac{L_{WL}}{\sqrt[3]{\nabla}}$ designating different loading conditions.

The model was free to pitch and heave, making pitch–heave oscillation (porpoising) the only possible dynamic instability. No porpoising was observed during the entire campaign, confirming stable behaviour across all tested conditions. Measurement uncertainties were consistently low, with median values of 0.4% for resistance, 1.5% for sinkage, and 0.7% for trim. A detailed summary of uncertainty estimates for all measured quantities is provided in Table 5.

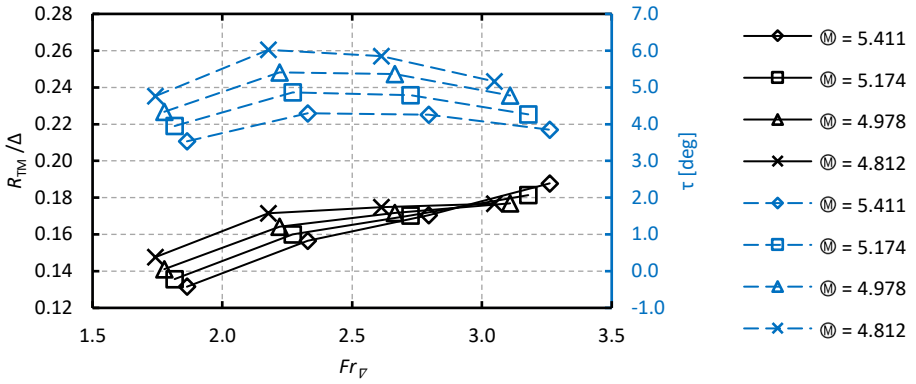

Figure 8. Resistance and trim of the bare hull with $Ⓜ = \frac{L_{WL}}{\sqrt[3]{\nabla}}$ *designating different loading conditions [P2].*

Table 5. Uncertainties of parameters measured through the test campaign.

	U_p' (R_{TM}/Δ)	U_p ($z_{VCG}/\nabla^{1/3}$)	U_p (τ) [deg]
Min	0.2%	0.001	0.027
Max	1.7%	0.004	0.085
Average	0.4%	0.002	0.035
Median	0.4%	0.001	0.032

2.3.1 Spray rails

Figure 9 compares the tested spray rail arrangements with the bare hull in terms of change in total resistance δRT_M, dynamic trim δτ and sinkage at the centre of gravity $\delta z_{VCG}/\nabla^{1/3}$. Photographic documentation of spray formation recorded during the model tests is provided in P2. Based on the comparative analysis, the key findings are summarised below.

Spray was deflected at all speeds except at Fr_∇ = 1.776, where the rails were submerged. This behaviour was consistent across different length-displacement ratios. Spray rails reduced the total resistance by up to 2.4% at planing speeds ($Fr_\nabla > 3$), but only at high length-displacement ratios (Ⓜ ≥ 5.174). At $Fr_\nabla < 2.5$, spray rails increased resistance by up to 8.3%. At semi-displacement speeds ($2.5 < Fr_\nabla < 3$), resistance increased by up to 2%, or remained within the uncertainty margin of 0.4%. These increases in resistance were generally attributed to increased running trim. Conventional spray rails (b_{SR} = 6–8 mm, δ= 0°) decreased the resistance by up to 1.3% at $Fr_\nabla > 3$ and Ⓜ >5.174 but increased it by up to 6% at $Fr_\nabla < 2.5$, due to added lift in the forebody, which shifted the centre of pressure forward and increased the running trim.

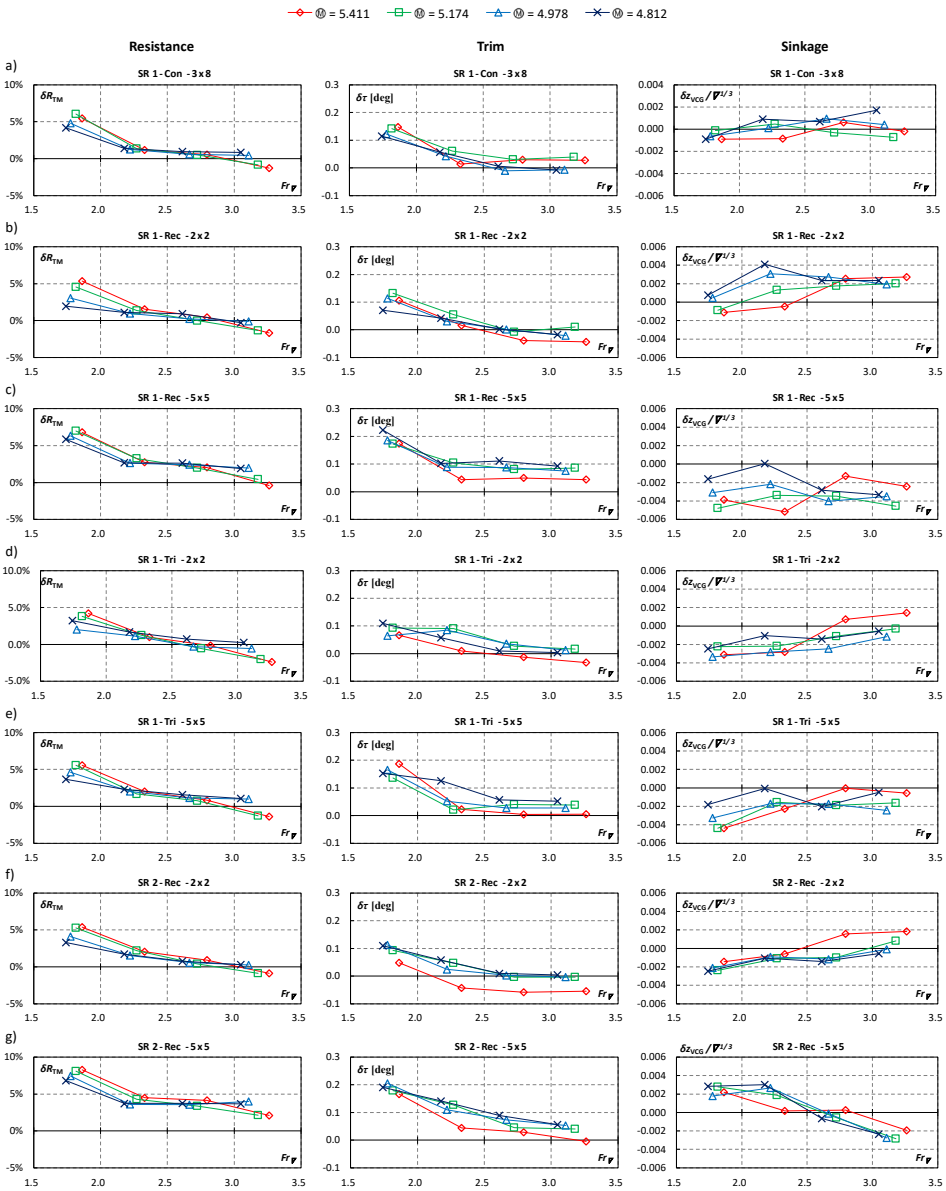

Figure 9. Change in resistance, trim and sinkage of the tested spray rail arrangements compared to the bare hull [P2].

Increasing the width from b_{SR} = 2 mm to b_{SR} = 5 mm raised resistance by 1.2–3.9% for rectangular profiles (Figure 9b, c), and 0.8–2.6% for triangular ones (Figure 9d, e). Wider rails generated more lift in the forebody, leading to increased trim and resistance. Changing the bottom angle from δ=–70° to δ=–25° (i.e., from rectangular to triangular) reduced resistance by 0.5–1.1% for narrow rails and 0.3–2.2% for wider ones. This was due to reduced lift and an aftward shift in the centre of pressure, which lowered trim.

Extending narrow spray rails (b_{SR} = 2 mm) to the transom increased resistance by 0.1–1.3%; for wider rails (b_{sr} = 5 mm), the increase was 1–2.5%. Longer rails (SR2) had

negligible impact on running attitude compared to shorter ones (SR1). At $Fr_\nabla > 3$, shorter rails already extended below the dynamic waterline, indicating that the added resistance was primarily due to increased wetted surface area and viscous drag.

Narrow triangular spray rails (b_{SR} = 2 mm, δ = –25°) consistently outperformed conventional horizontal spray rails, achieving the maximum reduction in resistance of 2.4% at $Fr_\nabla > 3$. Their improved performance is attributed to effective spray separation combined with reduced frictional resistance associated with their smaller width. This suggests that the vertical distance of the spray-rail outer edge from the hull bottom—governed jointly by the spray-rail width b_{SR} and bottom angle δ—is a key geometric parameter controlling spray-rail behaviour.

2.3.2 Chine strips

Figure 10 illustrates the effects of chine strips on the resistance and running attitude of the bare hull (a, b, c) and hulls equipped with spray rails (d, e). The chine strips CSI1, CSI2, CSR1, and CSR2 (Figure 10c) were tested at the end of the campaign and, due to time and resource constraints, only at the design displacement Ⓜ = 4.978. Photographic documentation of spray formation recorded during the model tests is provided in P2. Based on the comparative analysis, the key findings are summarised below.

Chine strips deflected spray between the chine-waterline intersection and the spray edge. At lower Froude displacement numbers ($Fr_\nabla < 2.5$), the stagnation line extends further forward, resulting in spray-induced pressure acting ahead of the centre of gravity. With increasing speed ($Fr_\nabla > 2.5$), the stagnation line moves aft, relocating the effective spray area behind the centre of gravity.

The influence of chine strips was strongly speed-dependent. At semi-displacement and low-planing speeds ($Fr_\nabla < 2.5$), all chine-strip configurations increased running trim by up to 0.8° and increased total resistance by as much as 9%. At planing speeds ($Fr_\nabla > 2.5$), the same configurations reduced trim by up to 0.3° and reduced resistance by up to 3%. The stagnation angle α therefore emerges as a governing parameter for chine-strip performance, as it determines whether the spray-induced lift increment acts forward or aft of the centre of gravity.

The magnitude of trim variations induced by chine strips was approximately three to four times larger than those observed for spray rails, which typically altered trim by less than ±0.1°. The substantially larger trim authority of chine strips compared to spray rails arises from their location at the chine–spray interaction region, where pressure forces directly contribute to the longitudinal trimming moment rather than primarily affecting spray separation.

Chine strip geometry also influenced performance. Triangular strips (CSR1, CSR2) generated more lift and greater trim reduction at planing speeds than rectangular strips (CSI1, CSI2). The larger triangular chine strip (CSR2) was consequently more effective than the smaller one (CSR1).

Interaction between chine strips and spray rails was also examined. When installed on hulls already equipped with spray rails, chine strips induced trim changes of ±0.3° and resistance changes of +3.2% at low speeds and –3% at high speeds. These effects were comparable to those observed on the bare hull, indicating that the hydrodynamic action of chine strips is largely independent of the presence of spray rails within the investigated speed range.

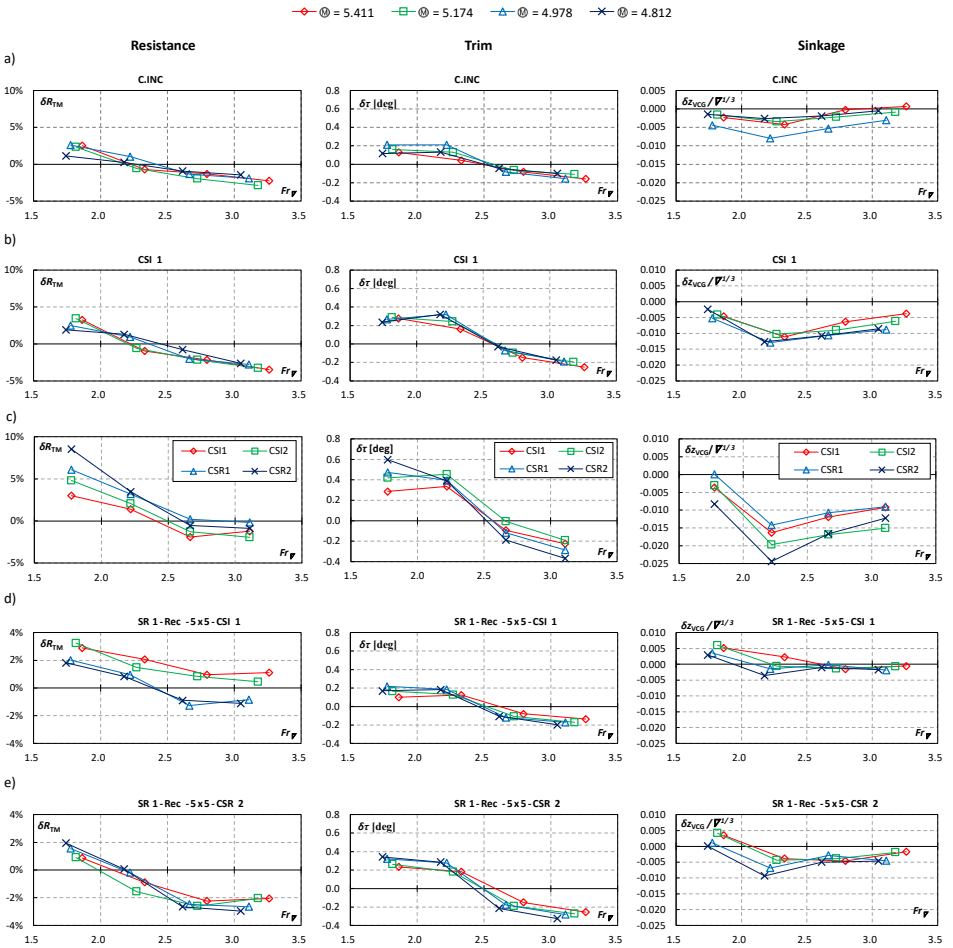

Figure 10. Change in resistance, running trim and sinkage of the tested chine strip arrangements [P2].

Retesting of the bare hull at the end of the experimental campaign revealed an increase in resistance of approximately 5%, attributed to surface degradation caused by repeated attachment and removal of appendages. While this degradation affected absolute resistance levels, trim measurements for configurations such as CSI1 remained consistent. Consequently, relative comparisons based on trim trends and resistance changes normalised by the contemporaneous bare-hull condition remain valid.

Overall, the results indicate that chine strips primarily affect hydrodynamic performance by shifting the longitudinal pressure distribution. At lower speeds, lift is generated forward of the CG, increasing trim and resistance, whereas at planing speeds lift shifts aft, reducing trim and resistance. The experimental evidence suggests that chine strips exhibit beneficial effects only within the planing regime, while their use outside this range entails clear hydrodynamic penalties. Thus, their forebody extent must be limited to avoid adverse trim and resistance penalties at semi-displacement speeds. Although chine strips provide measurable trim reduction at planing speeds, their

authority remains significantly lower than that of stern interceptors, and they should therefore be viewed as complementary rather than substitutive trim-control devices.

2.3.3 V-shaped spray interceptors

Figure 11 compares the changes in the total resistance, running trim and sinkage of the hull fitted with V-shaped spray interceptor (VSI) relative to the bare hull. Photographic documentation of spray formation recorded during the model tests is provided in P2. The principal findings are summarised below.

At planing speeds ($Fr_\nabla > 2.5$), the VSI consistently deflected spray across all tested length-displacement ratios. At semi-displacement speeds ($Fr_\nabla < 2.5$), no effective spray deflection was observed. Changes in trim and sinkage were negligible across all speeds, indicating that the VSI did not induce measurable change in lift or centre of pressure.

At planing speeds ($Fr_\nabla > 2.5$), the VSI reduced the resistance by 2.1–4.2%, with the greatest reductions occurring at a slightly lower planing speed and at a higher length-displacement ratio. At semi-displacement speeds ($Fr_\nabla < 2.5$), the VSI increased the resistance by 2.1–8.4%, with the greatest increases at Ⓜ = 5.174 and the smallest increases at Ⓜ = 4.812.

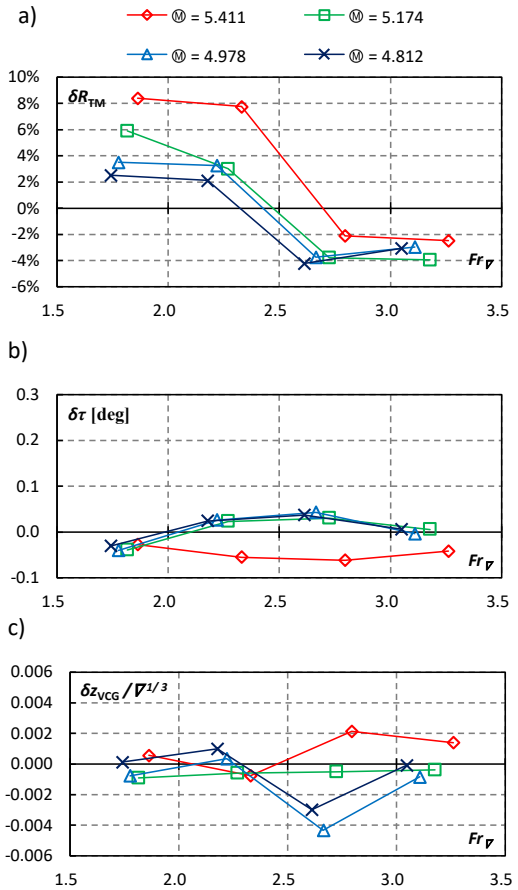

Figure 11. Change in resistance (a), trim (b), and sinkage (c) of the VSI compared to the bare hull [P2].

3 Numerical study

This chapter presents the numerical modelling approach adopted to simulate the calm-water performance of the investigated planing hull and its appended configurations. The numerical study examines the influence of modelling choices, including degrees of freedom, wall-treatment strategy, and towing-force representation, on the prediction of resistance and running attitude. Verification and validation are carried out through comparison with the experimental data, after which the validated numerical models are applied as analysis tools to investigate the hydrodynamic effects of spray rails, chine strips, and V-shaped spray interceptors.

3.1 Numerical model

The CFD simulations were performed by solving the incompressible Reynolds-Averaged Navier–Stokes (RANS) equations:

$$\frac{\partial u_i}{\partial t} + u_j \frac{\partial u_i}{\partial x_j} = -\frac{1}{\rho}\frac{\partial p}{\partial x_i} + \nu \frac{\partial^2 u_i}{\partial {x^2}_j} - \frac{\partial}{\partial x_j}\left(u_i' u_j'\right) \quad (1)$$

$$\frac{\partial u_i}{\partial x_i} = 0 \quad (2)$$

where u_i and u_j are the velocity components, p is the pressure, ρ the fluid density, ν the kinematic viscosity, and $u_i' u_j'$ the Reynolds stresses modelled using the Realizable $k-\epsilon$ turbulence model.

The air-water interface was captured using the Volume of Fluid (VOF) method through the volume fraction transport equation:

$$\frac{\partial \alpha}{\partial t} + \nabla \cdot (\alpha \mathbf{u}) + \nabla \cdot [\alpha(1-\alpha)\mathbf{u_r}] = 0 \quad (3)$$

where α is the volume fraction of water (with air being 1–α), and $\mathbf{u_r}$ is the relative velocity at the interface. The High-Resolution Interface Capture (HRIC) scheme was employed to maintain a sharp and stable interface (Gray-Stephens et al., 2019).

A variable time step, determined by local flow velocity and mesh size, ensured a Courant number below unity according to the Courant-Friedrichs-Lewy (CFL) condition:

$$\Delta t = \frac{CFL \cdot \Delta x}{V_{Hull}} = \frac{0.25 \cdot BS}{V_{Hull}} = \frac{0.008 \cdot L_{pp}}{V_{Hull}} \quad (4)$$

where Δx is the cell size (25% of the base size *BS* in the first level of refinement in the overset region), V_{Hull} is the hull velocity, and L_{pp} the length of the hull between perpendiculars. The condition satisfied the ITTC guidelines (ITTC 7.5-03-02-03 Rev 01, 2017) ensuring $\Delta t < 0.01\, L_{pp}/V_{Hull}$ across all simulated Froude numbers.

The towing force *T* was prescribed at the same location as in model tests (see TPH and TPV in Table 1) and defined as:

$$T = R_{TM} \cos(\tau)\,, \quad (5)$$

where R_{TM} is the model-scale resistance and τ the trim angle.

Hull motions were resolved using the Dynamic Fluid–Body Interaction (DFBI) model. Two configurations were tested: a two-degree-of-freedom (2DOF) setup allowing heave and pitch, and a three-degree-of-freedom (3DOF) setup allowing surge, heave, and pitch. In the 2DOF setup, the computational domain remained stationary and the prescribed hull speed was imposed through the incoming flow. In the 3DOF setup, surge velocity

was prescribed through the motion of the computational domain relative to stationary water. This approach simplifies velocity specification and avoids wave generation associated with gradual inflow acceleration in conventional 2DOF simulations (Wheeler et al., 2021).

The computational domain (Figure 12 and Figure 13) consisted of hexahedral control volumes with prism layers near the hull to resolve the boundary layer. Domain dimensions followed ITTC guidelines (ITTC 7.5-03-02-03 Rev 01, 2017d) and recent practices (Niazmand Bilandi et al., 2024; Wheeler et al., 2021). The domain comprised a stationary far-field region (velocity inlet, pressure outlet, and symmetry boundaries) and a moving overset region (wall, symmetry, and overset boundaries). A linear interpolation scheme was used between the two regions (De Luca et al., 2016). Wave-forcing was applied at the inlet, outlet, and lateral boundary to mitigate wave-reflection. A wave-forcing length of $2.5L_{PP}$ was adopted following recommendations reported in the literature (Lee et al., 2019; SIEMENS PLM, 2022; Wheeler et al., 2021).

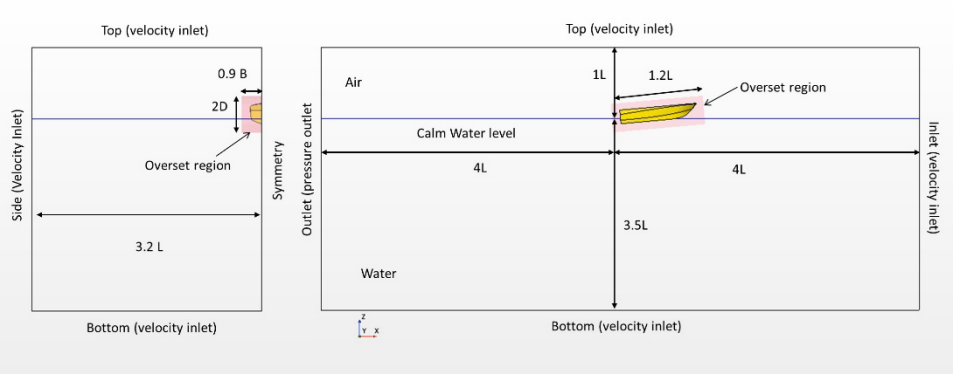

Figure 12. Computational domain and boundary conditions [P3].

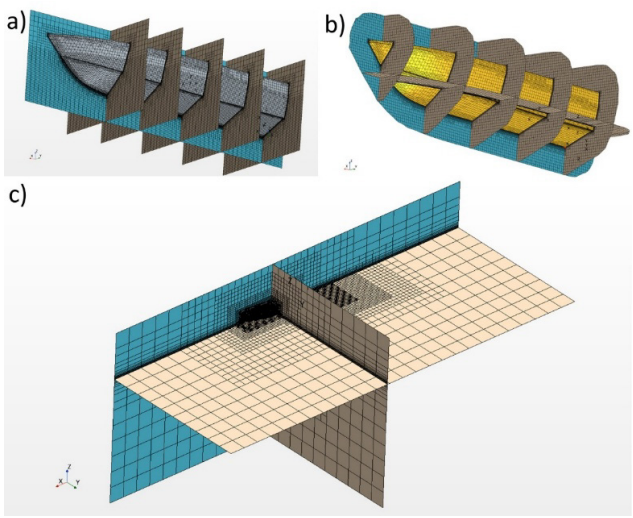

Figure 13. Domain mesh configuration: (a, b) Overset region mesh surrounding the hull, designed to move with the vessel and capture fine flow details, and (c) far-field region mesh, which remains stationary to simulate ambient flow conditions efficiently [P3].

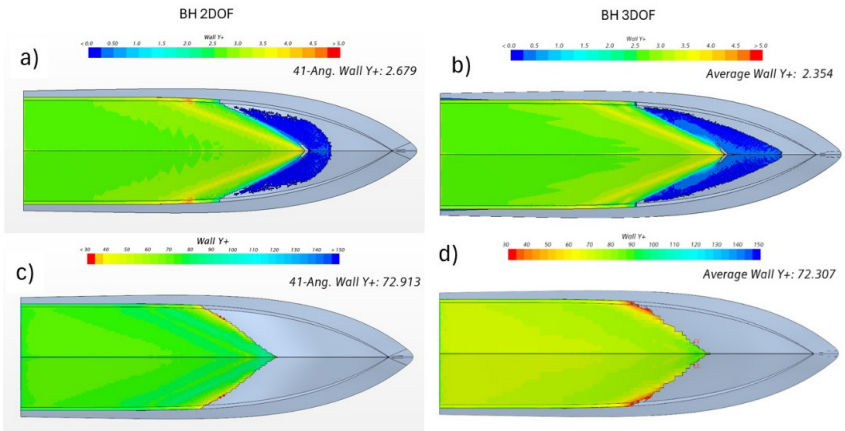

Figure 14. Wall y^+ Distribution — The upper region (a, b) shows $y^+ < 5$, indicating a fine mesh near the wall, while the lower region (c, d) exhibits $y^+ > 30$, suggesting a coarser boundary layer resolution [P3].

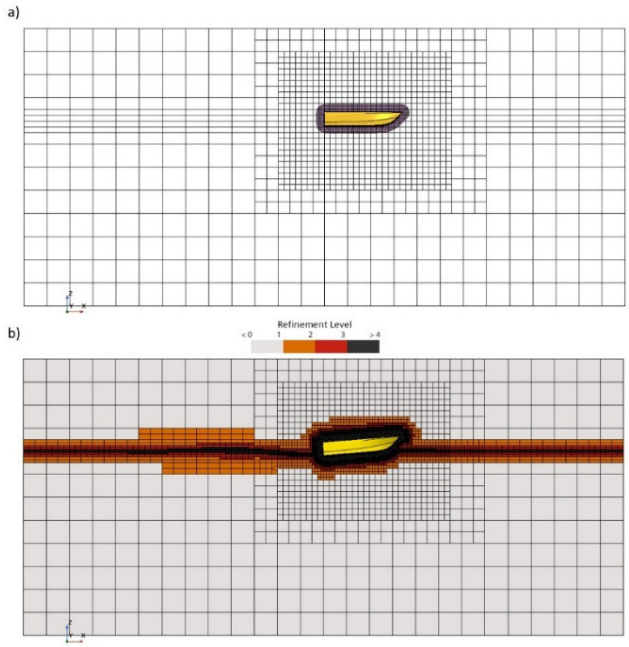

Figure 15. Computational domain of the 3DOF numerical model before (a) and after (b) the activation of AMR [P3].

Boundary layer resolution followed two meshing strategies: low-y^+ ($y^+ < 5$) with 15 prism layers and high-y^+ ($y^+ > 30$) with 8 layers (see Figure 14). Both setups used a uniform prism layer thickness and the Two-Layer All-y^+ wall treatment. Adaptive Mesh Refinement (AMR) was activated only in the 3DOF simulations to capture spray formation and free-surface deformation (Figure 15).

Numerical ventilation (NV)—air entrainment from interface smearing in the VOF model—was mitigated using several methods. The air-suction technique (Viola et al., 2012) was applied in most simulations, while the slip-velocity approach (Wheeler et al.,

2021) was employed for 3DOF high-y^+ cases. Additional measures included local refinement around the bow and free surface, optimized prism alignment, and High-Resolution Interface Capture (HRIC) for sharper phase definition (Gray-Stephens et al., 2019). These strategies minimized entrained air, ensuring stable predictions of resistance and pressure (see Figure 16). Further implementation details and solver settings are provided in P3.

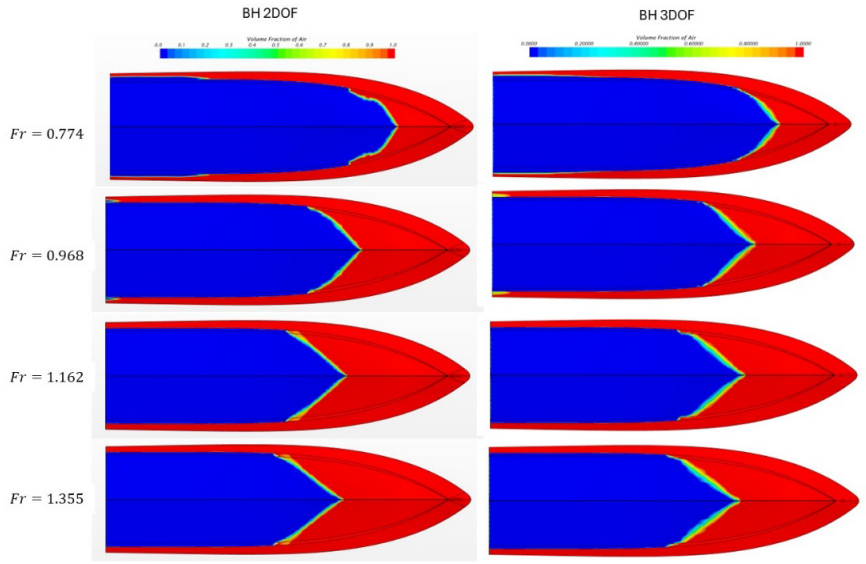

Figure 16. Volume fraction of air on the hull surface, displaying minimal ventilation across all simulated speeds [P3].

Table 6. Solver settings for the planing hull CFD simulation.

Item	2DOF $y^+ < 5$	2DOF $y^+ > 30$	3DOF $y^+ < 5$	3DOF $y^+ > 30$
DOF	2DOF	2DOF	3DOF	3DOF
Convection Term	2nd order	2nd order	2nd order	2nd order
Temporal Discretization	1st order	1st order	1st order	1st order
Time-step [s]	Function of velocity and mesh size	Function of velocity and mesh size	Function of velocity and mesh size	Function of velocity and mesh size
Inner iterations per time step	5	5	5	5
Turbulence model	Realizable k-ε	Realizable k-ε	Realizable k-ε	Realizable k-ε
Overset interpolation scheme	Linear	Linear	Linear	Linear
Iterations of 6-DOF solver per inner iteration	3	3	3	3
Wall treatment	Two-Layer All y^+	Two-Layer All y^+	Two-Layer All y^+	Two-Layer All y^+
Number of prism-layers	15	8	15	8
Prism Layer Thickness	0.012 m	0.012 m	0.012 m	0.012 m
NV treatment	Air Suction	Air Suction	Air Suction	Slip velocity
AMR	No	No	Yes	Yes
DFBI	Free motion	Free motion	General Planar motion	General Planar motion
DOF	Pitch and heave	Pitch and heave	Surge, Pitch, and heave	Surge, Pitch, and heave

3.2 Verification & validation methodology

This section defines the verification and validation (V&V) framework adopted in the numerical study. Its purpose is to establish how numerical uncertainty is quantified, how numerical predictions are compared with experimental measurements, and how validation success is defined. The framework presented here governs model admissibility in the subsequent analyses.

Verification evaluates simulation uncertainty (U_{SN}) arising from numerical errors associated with spatial and temporal discretisation, iterative convergence, and other modelling parameters (Stern et al., 2001). Simulation error (δ_{SN}) and uncertainty (U_{SN}) are decomposed into components for iteration (δ_I), grid (δ_G), timestep (δ_{TS}) and other parameters (δ_P):

$$\delta_{SN} = \delta_I + \delta_G + \delta_{TS} + \delta_P \tag{6}$$

$$U_{SN}^2 = U_I^2 + U_G^2 + U_{TS}^2 + U_P^2 \tag{7}$$

For ship-hydrodynamics applications, grid uncertainty is typically the dominant contribution to numerical uncertainty (De Luca et al., 2016; Wilson et al., 2006). Accordingly, in the present study the simulation uncertainty is approximated as

$$U_G^2 \approx U_{SN}^2 \tag{8}$$

Validation evaluates the agreement between numerical predictions *S* and experimental measurements *D.* The comparison error *E* and validation uncertainty U_V are defined as:

$$E = D - S = \delta_D - (\delta_{SM} + \delta_{SN}) \tag{14}$$

$$U_V^2 = U_D^2 + U_{SN}^2 \tag{15}$$

where U_D denotes experimental uncertainty. Thus, a numerical model is considered validated if the absolute comparison error satisfies $|E| \leq U_V$. Otherwise, the model or data accuracy needs improvement.

Grid-related discretisation uncertainty is estimated using systematic grid-refinement studies employing established procedures including the Grid Convergence Index (GCI) (Celik et al., 2008), the Correction Factor (CF) following ITTC recommendations (ITTC 7.5-03-01-01 Rev. 04, 2021; Stern et al., 2006), and GCI-LSR methods (Eça & Hoekstra, 2014, 2006). The full mathematical formulations and implementation details of these methods are reported in P3 and are not repeated here.

In the present work, these procedures are used to quantify discretisation uncertainty in support of the validation assessment. The V&V framework defined in this section establishes the rules governing model admissibility. Its application to the bare hull and to appended hull configurations is presented in Sections 3.3 and 3.4.

3.3 Verification and validation on the bare hull

This section applies the verification and validation methodology defined in Section 3.2 to the numerical models introduced in Section 3.1, using the bare hard-chine hull in calm water as a reference case. The purpose is to evaluate the performance of the different numerical formulations against experimental measurements of resistance and running attitude, and to determine which models satisfy the validation criteria within the established uncertainty bounds. The bare hull is selected to isolate numerical modelling

effects from appendage-induced flow phenomena. The results presented here establish the validated numerical models and the associated reference uncertainty limits used in the subsequent analysis of appended hull configurations.

Grid sensitivity is assessed to quantify discretisation uncertainty and to confirm that the numerical predictions are independent of further spatial refinement within the limits required for validation. The verification analysis is conducted under design condition (Fr = 1.355, Fr∇ = 3.108, Ⓜ = 4.978) using the GCI, CF, and GCI-LSR methods, following the framework outlined in Section 3.2. Four systematically refined grid structures—A (coarse), B (medium), C (fine), and D (very fine)—are generated around the hull with a constant refinement ratio of $r_G = \sqrt{2}$.

The GCI and CF methods, both based on Richardson extrapolation, are evaluated using the grid triplets A–B–C and B–C–D. In contrast, the curve-fitting approach of Eça and Hoekstra employs the Least Squares Root (LSR) of the solution over multiple grid levels and therefore requires a minimum of four systematically refined grids. Consequently, the LSR analysis is conducted using the complete grid sequence A–B–C–D. The corresponding mesh properties for all numerical setups are reported in Tables C.1–C.8 of P3. Figure 17 compares numerical predictions of resistance, sinkage, and trim with experimental measurements, forming the basis for the validation assessment of the bare hull. The results of the uncertainty analysis are presented in Tables 7–10.

Table 7. Results of the verification and validation analysis for the 2DOF $Y^+ < 5$ numerical model with towing force. Values marked with (*) indicate cases where the estimated order of accuracy was restricted to $p_G = 2$ in accordance with the recommendations of Eça and Hoekstra.

	Grids	R_G	p_G (RE)	p_G (LSR)	$\|1\text{-}C_G\|$	$\%U_G$ (GCI)	$\%U_G$ (CF)	$\%U_G$ (LSR1)	$\%U_G$ (LSR2)	$\%U_{SN}$	$\%U_D$	$\%U_V$	$\%\|E\|$	Validation (Yes / No)
R_{TM}	A-B-C	1.00	0.01	0.32	1.00	144	346	0.5*	0.8*	0.8	0.3	0.9	5.0	No
	B-C-D	0.43	2.46		0.35	0.15	0.21							
z_{VCG}	A-B-C	3.89	-3.92	1.41	1.74	N.A.	N.A.	1.8	2.6	2.6	0.8	2.8	9.8	No
	B-C-D	0.24	4.13		2.18	0.14	0.60							
τ	A-B-C	4.17	-4.12	12.5	1.76	N.A.	N.A.	0.6*	1.9*	1.9	0.6	2.0	14.6	No
	B-C-D	-2.47	N.A.		N.A.	N.A.	N.A.							
S_{WB}	A-B-C	-8.88	-6.30	1.41	1.89	N.A.	N.A.	1.0	3.7	3.7	1.0	3.8	2.3	Yes
	B-C-D	0.09	6.81		8.61	0.01	0.16							

The curve-fitting verification analysis published in P3 was carried out following the earlier Eça & Hoekstra methodology (Eça & Hoekstra, 2006). The current ITTC guidelines adopt the updated procedure (Eça & Hoekstra, 2014). Reevaluating the uncertainties following the revised procedure (designated as LSR2) yielded larger uncertainty bounds. Compared with LSR1, which applies a fixed safety factor of $F_S = 1.25$, LSR2 distinguishes between good and bad convergence based on the relationship between the data range parameter Δ_ϕ and standard deviation of the fit, σ. For cases exhibiting significant scatter ($\sigma \geq \Delta_\phi$), a safety factor of $F_S = 3$ is applied. In addition, LSR2 explicitly accounts for the deviation of the numerical solution from the fitted convergence curve, $|\phi_i - \phi_{fit}|$, in the uncertainty estimate. The uncertainty may be further amplified when the standard deviation of the fit becomes large relative to the data-range parameter through the factor $3\sigma/\Delta\phi$. Consequently, LSR2 provides a more conservative estimate of numerical uncertainty for solutions exhibiting significant scatter.

Table 8. Results of the verification and validation analysis for the 3DOF $Y^+ < 5$ numerical model.

	Grids	R_G	p_G (RE)	p_G (LSR)	$\|1\text{-}C_G\|$	$\%U_G$ (GCI)	$\%U_G$ (CF)	$\%U_G$ (LSR1)	$\%U_G$ (LSR2)	$\%U_{SN}$	$\%U_D$	$\%U_V$	$\%\|E\|$	Validation (Yes / No)
R_{TM}	A-B-C	-4.48	N.A.	1.96	N.A.	N.A.	N.A.	0.2	1.0	1.0	0.3	1.1	4.4	No
	B-C-D	0.16	5.25		4.18	0.01	0.11							
z_{VCG}	A-B-C	-0.26	3.83	0.58	1.78	0.32	1.18	1.2	1.9	1.9	0.8	2.1	0.5	Yes
	B-C-D	0.45	2.33		0.24	0.09	0.10							
τ	A-B-C	-1.17	N.A.	1.82	N.A.	N.A.	N.A.	0.1	1.0	1.0	0.6	1.2	10.9	No
	B-C-D	-0.95	N.A.		N.A.	0.06	0.06							
S_{WB}	A-B-C	-0.56	N.A.	8.61	N.A.	0.51	0.51	2.4*	4.2*	4.2	1.0	4.3	7.1	No
	B-C-D	9.6	-6.33		1.90	N.A.	N.A.							

Table 9. Results of the verification and validation analysis for the 2DOF $Y^+ >30$ numerical model with towing force.

	Grids	R_G	p_G (RE)	p_G (LSR)	$\|1\text{-}C_G\|$	$\%U_G$ (GCI)	$\%U_G$ (CF)	$\%U_G$ (LSR1)	$\%U_G$ (LSR2)	$\%U_{SN}$	$\%U_D$	$\%U_V$	$\%\|E\|$	Validation (Yes / No)
R_{TM}	A-B-C	-0.81	N.A.	0.003	N.A.	0.75	0.75	1.1*	10.5*	10.5	0.3	10.5	1.9	Yes
	B-C-D	-0.85	N.A.		N.A.	0.61	0.61							
z_{VCG}	A-B-C	-3.23	N.A.	0.04	N.A.	N.A.	N.A.	1.9*	2.2*	1.9	0.8	2.1	0.4	Yes
	B-C-D	0.11	6.26		6.74	0.05	0.59							
τ	A-B-C	-1.22	N.A.	3.11	N.A.	N.A.	N.A.	2.0*	16.2*	2.0	0.6	2.1	0.5	Yes
	B-C-D	-0.19	N.A.		N.A.	1.61	1.61							
S_{WB}	A-B-C	-2.17	N.A.	2.82	N.A.	N.A.	N.A.	1.2*	1.5*	1.2	1.0	1.6	10.7	No
	B-C-D	0.34	3.12		0.95	0.35	0.82							

Table 10. Results of the verification and validation analysis of the 3DOF $Y^+ >30$ numerical model.

	Grids	R_G	$p_{G,\,RE}$	$p_{G,\,LSR}$	$\|1\text{-}C_G\|$	$\%U_G$ (GCI)	$\%U_G$ (CF)	$\%U_G$ (LSR1)	$\%U_G$ (LSR2)	$\%U_{SN}$	$\%U_D$	$\%U_V$	$\%\|E\|$	Validation (Yes / No)
R_{TM}	A-B-C	-0.49	N.A.	11.6	N.A.	0.88	0.88	1.3*	9.6*	9.6	0.3	9.6	2.2	Yes
	B-C-D	1.97	-1.96		1.49	N.A.	N.A.							
z_{VCG}	A-B-C	-0.42	N.A.	0.58	N.A.	1.83	1.83	2.3*	21.8*	2.3	0.8	2.5	1.1	Yes
	B-C-D	1.58	-1.33		1.37	N.A.	N.A.							
τ	A-B-C	-0.64	N.A.	6.38	N.A.	2.35	2.35	3.0*	23.6*	3.0	0.6	3.0	0.9	Yes
	B-C-D	0.94	0.17		0.94	60.2	139							
S_{WB}	A-B-C	-0.45	N.A.	8.61	N.A.	1.72	1.72	3.5*	26.2*	26.2	1.0	26.2	10.5	Yes
	B-C-D	2.18	-2.25		1.54	N.A.	N.A.							

* Values marked with (*) indicate cases where the estimated order of accuracy was restricted to p_G = 2 in accordance with the recommendations of Eça and Hoekstra.

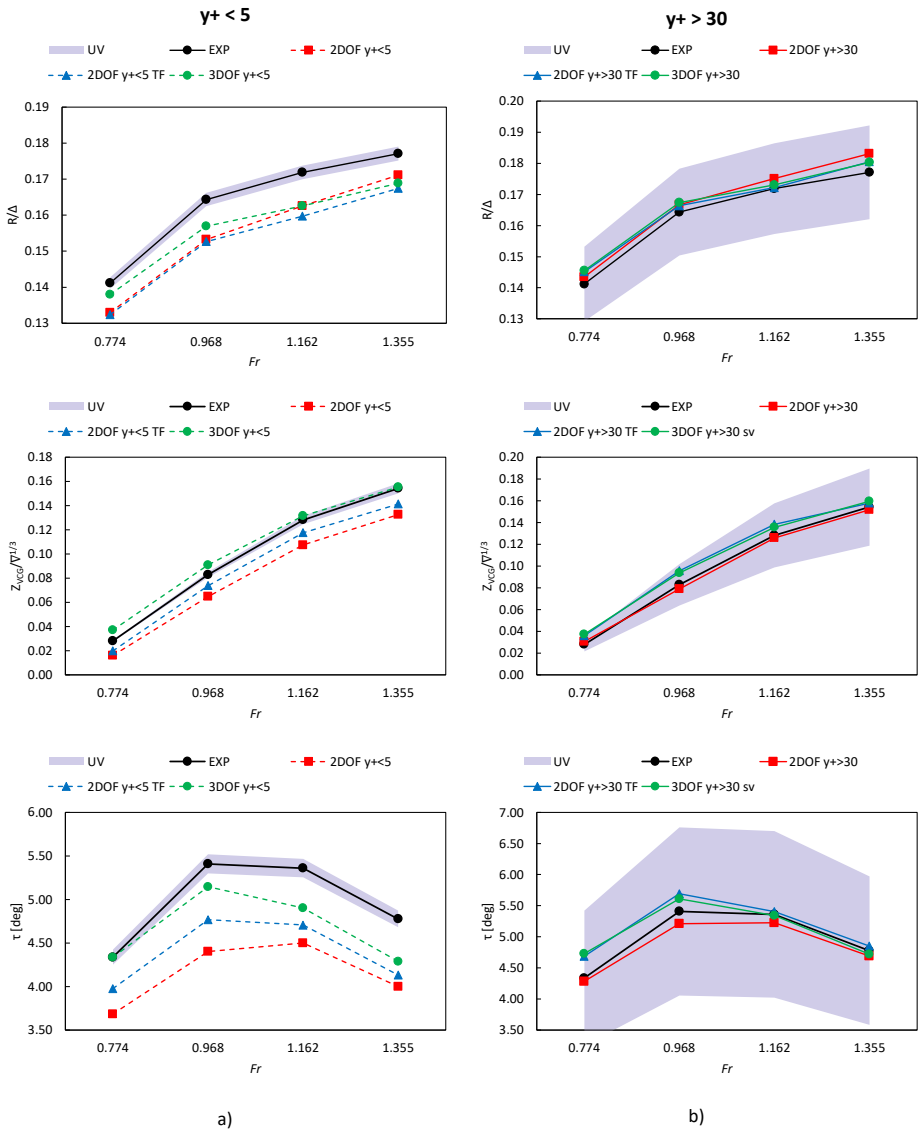

Figure 17. Comparison between CFD predictions and experimental measurements of bare hull resistance, sinkage, and trim with validation uncertainty bounds indicated by shaded bands.

Models with $y^+ < 5$, which directly resolve the viscous sub-layer, underestimated trim by 5–18%, leading to resistance being underestimated by 2–7%. These errors exceeded the validation uncertainty (see Tables 7–8) – and thus, these models were not validated. The relatively small scatter observed in the grid-refinement studies resulted in tight uncertainty bounds, making the validation criterion particularly stringent.

Models with $y^+ > 30$, which used wall functions, predicted resistance and running attitude within the validation uncertainty (see Tables 9–10) and were therefore validated. The 2DOF model was validated using the B mesh, and the 3DOF model using the A mesh. At lower speeds, the 2DOF simulations tended to underestimate trim by up to 8%, while the 3DOF simulations tended to overestimate trim by up to 9%. At planing

speeds, however, the agreement improved considerably, with trim predictions generally within ±1.5% of the measured values. Resistance was consistently overestimated by 1–4%, with the largest discrepancies occurring at the lower speeds.

A potential source of the elevated uncertainty values is the selected mesh refinement strategy. The mesh levels were generated to achieve a cell-count refinement ratio of approximately $r_G = \sqrt{2}$ between consecutive grids, resulting in a relatively small separation between mesh resolutions. This may have reduced the sensitivity of the grid-convergence study and increased the influence of numerical scatter. A more robust approach would be to apply the refinement ratio directly to the base mesh size, thereby increasing the separation between grid levels and improving the reliability of the uncertainty estimation.

A second contributor may be the AMR strategy. Mesh adaptation was performed every five time-steps throughout the simulation, although the planing-hull solution approaches a steady operating condition. Once sinkage, trim and resistance have converged, such frequent adaptation may introduce unnecessary mesh modifications and additional numerical scatter. Reducing the AMR frequency during the later stages of the simulation could improve solution stability and reduce the estimated uncertainty.

Figure 18 presents the accumulated pressure forces in the z-direction along the hull length. In the case with 15 prism layers ($y^+ < 5$), higher pressure is observed at the transom and lower pressure in the foreship region ($x/L_{PP} > 0.4$). The centroid of the area under these curves corresponds to the longitudinal centre of pressure. From the curve shapes, it can be deduced that with 15 prism layers ($y^+ < 5$), the centre of pressure shifts further aft. This shift increases the trimming moment, causing the bow to pitch downward and resulting in a lower trim angle compared to the case with 8 prism layers ($y^+ > 30$). Moreover, this effect is more pronounced in the 3DOF setup than in the 2DOF setup.

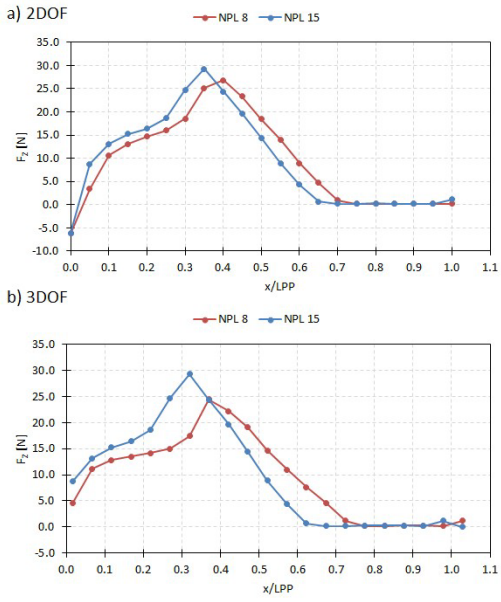

Figure 18. Accumulated pressure forces in the z-direction on the hull: blue, $y^+ < 5$; red, $y^+ > 30$ [P3].

To further investigate this behaviour, a captive simulation was run using the 2DOF y^+ < 5 setup with towing force applied, employing the A-level (coarse) mesh, and at a running attitude measured in the model test. The difference in resistance was less than 0.14%, which—assuming a validation uncertainty of ($U_V \leq 0.6\%$)—would be sufficient to consider the numerical model validated. However, the simulation also produced excess lift and a trimming moment, indicating that to achieve the observed running attitude, the model would need to be approximately 1.5 kg heavier (7%), and the centre of gravity (CG) shifted aft by 35 mm (2% L_{WL}). After applying these adjustments, the comparison error in resistance, sinkage, and trim was small enough for the model to be validated at top speed. Nevertheless, large discrepancies were observed at lower speeds, and therefore, this approach was not pursued further.

Potential errors arise from discrepancies between the CAD geometry and its discretised representation, affecting the centre of gravity (CG), longitudinal centre of gravity (LCG), and hull displacement. To quantify this effect, quasi-static simulations employing the coarse mesh were performed at near-zero speed ($Fr \approx 0$) to determine the initial sinkage and trim at rest. The results indicate small but measurable biases in the initial resting position. For the 2DOF setup, a sinkage of 0.001 m and a trim of –0.05° (bow up) were obtained, while the 3DOF setup yielded the same sinkage and a trim of +0.01° (bow down). Although small in absolute terms, these biases correspond to 2–9% of dynamic sinkage and 0.3–1% of dynamic trim within the investigated speed range ($Fr = 0.774 - 1.355$ and $Fr_\nabla = 1.776 - 3.109$). Their influence is therefore non-negligible in the context of tight validation uncertainties.

The inclusion of the towing force increased the running trim by 0.1°–0.4°, with the largest effect observed in the semi-displacement regime (Figure 17). It also increased the rise of the craft, improving the running attitude; however, this adjustment did not significantly improve the resistance prediction. Figure 19 displays the effects of the towing force at the craft's top speed (Fr=1.355, Fr_∇= 3.108). The towing force was applied after the simulation without the towing force had reached convergence. While the missing towing force contributes to the observed discrepancies, it is not the primary factor responsible for the differences between experimental and numerical results.

To assess whether discrepancies in resistance and trim arise from hull-edge geometry (Judge et al., 2020), a 3D model with 2–3 mm filleted edges was simulated using the 2DOF y^+ < 5 setup with towing force at the A-level mesh. The denser mesh required for the rounded edges made the simulation more computationally demanding. The comparison between sharp and rounded hull edges revealed minimal change in resistance—only a 0.1% reduction with fillets. However, the running attitude was notably affected: sinkage decreased by 10.7%, indicating reduced lift, while trim increased by 1.1%, suggesting a more bow-up attitude. The wetted bottom area also increased by 8.5%. These results, supported by pressure distribution visualizations in P3, demonstrate that even small geometric modifications can significantly influence the dynamic behaviour of planing hulls.

The verification and validation study on the bare hull confirms that numerical models employing wall-function-based near-wall treatment (with y^+ > 30) reproduce resistance, trim, and sinkage within the combined experimental and numerical uncertainty bounds. These models are therefore considered validated, and the associated uncertainty levels define the applicable confidence limits of the numerical predictions. Within these limits, the validated models are adopted unchanged in the following section to assess appendage-induced trends on the hard-chine hull.

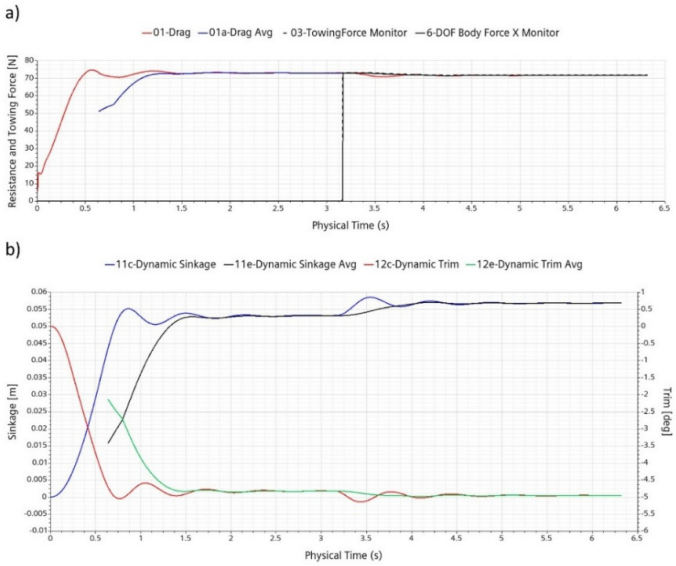

Figure 19. Influence of the towing force on the resistance (a) and the running attitude of the hull (b) at Fr = 1.355 [P3].

3.4 Application of the numerical models to appended hull configurations

The validated CFD models—2DOF (with towing force applied) and 3DOF—were applied to a hard-chine planing hull equipped with various appendages: spray rails (SR1, SR2), chine strips (CSI), and a V-shaped spray interceptor (VSI). Both models employed wall functions ($y^+ > 30$) and the A-mesh (coarse). The simulations were carried out to evaluate how accurately the numerical models reproduce the experimentally observed trends in resistance and running attitude across the tested Froude number range Fr = 0.774–1.355 and Fr_∇ = 1.776–3.109.

Figure 20 and Figure 21 show the pressure and shear stress distributions on the hull and appendage surfaces, respectively, while Figure 22 and Figure 23 present quantitative comparisons between CFD predictions and experimental measurements, with the corresponding numerical values summarised in Table D.1 in P3. The validation uncertainties determined for the bare hull (Sec. 3.3) were assumed to apply to all appended configurations.

Overall, both numerical models reproduced the principal hydrodynamic trends observed in the experiments. For the 2DOF setup, the mean comparison error E ranged from –5.6 % to +5.0 % for resistance, –32.6 % to +23.9 % for sinkage, and –9 % to +5.1 % for trim, with the largest deviations occurring in the semi-displacement regime (Fr =0.774–0.968). The 3DOF model consistently yielded results closer to the experimental data, with most deviations smaller than the validation uncertainty. This improvement is attributed to its dynamic force–moment equilibrium formulation, whereas the 2DOF setup relies on the averaged towing force from previous time steps.

For the spray-rail configurations, both SR1 and SR2 were generally validated, although the 2DOF model tended to underpredict resistance at low speeds and overpredict trim. The 3DOF model predicted resistance, sinkage, and trim within validation bounds across

most conditions. Wider spray rails increased the local pressure and frictional resistance, while the narrower SR2 effectively deflected spray with minimal trim penalty.

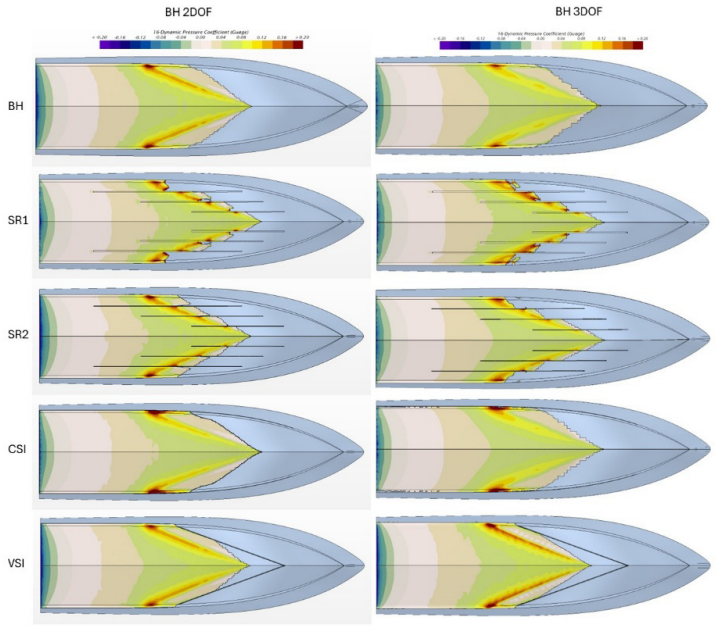

Figure 20. Pressure distribution on the tested hull configurations at Fr = 1.355 [P3].

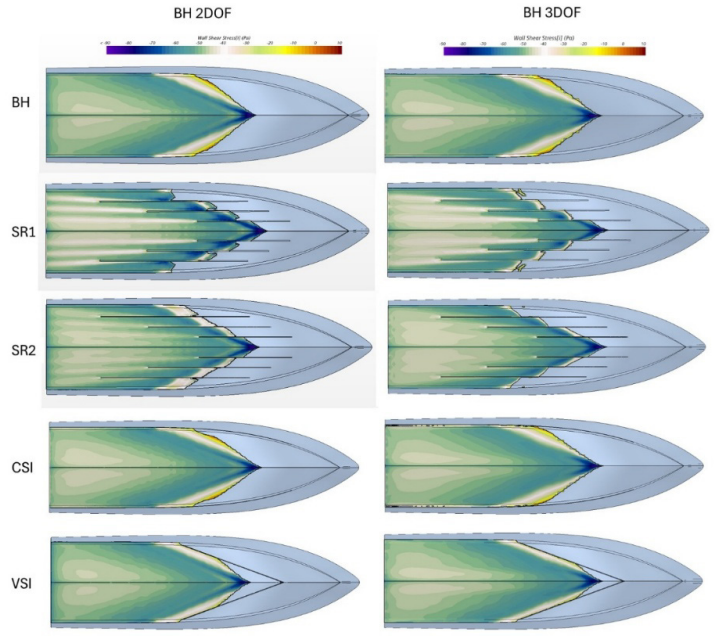

Figure 21. Shear stress distribution on the tested hull configuration at Fr = 1.355 [P3].

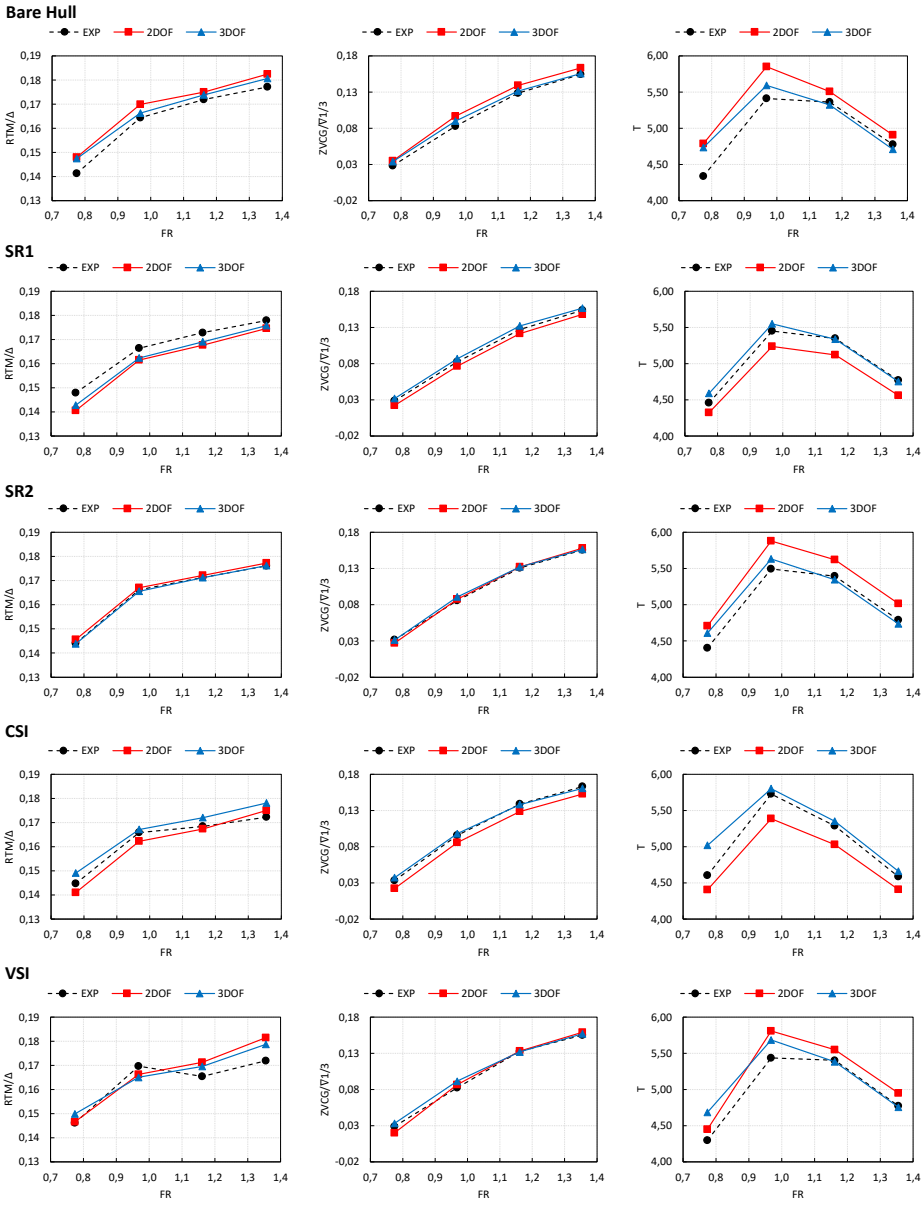

Figure 22. EFD vs CFD: resistance, sinkage, and trim [P3].

The chine-strip configuration (CSI) was also well captured, particularly by the 3DOF model, which produced validated results for all parameters except sinkage at the lowest speed. The 2DOF simulations matched resistance and trim trends but showed larger errors in sinkage.

For the V-shaped spray interceptor (VSI), both models reproduced the general behaviour, but the 3DOF predictions were again closer to the experiments. The VSI generated a modest reaction force that reduced resistance by approximately 1.6 % of total resistance, consistent with its position forward of the stagnation line. Most of the

remaining resistance reduction resulted from the absence of the pressure and frictional resistance contributions associated with spray rails, rather than from the reaction force generated by the VSI itself. This can be clearly observed in Figures 20 and 21.

Although both numerical models provided good qualitative agreement with the experiments, the quantitative improvements remained within the same order as the validation uncertainty, making the CFD results indicative rather than conclusive. The findings highlight the need for improved precision before the models can be applied for reliable appendage optimization at low planing speeds.

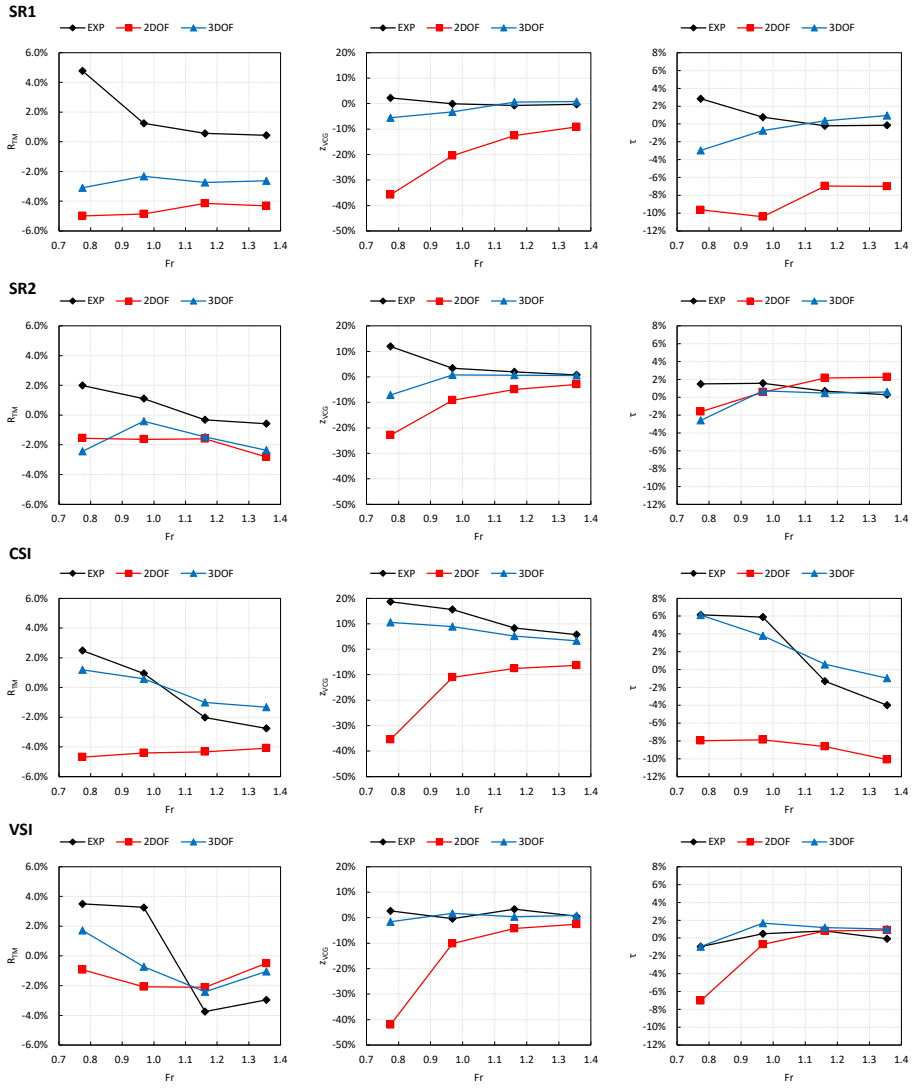

Figure 23. Comparison of EXP, 2DOF and 3DOF simulations: resistance, sinkage, and trim normalized by the bare hull [P3].

4 Conclusions

This study addressed key uncertainties in the hydrodynamic performance of spray-control appendages used on hard-chine planing hulls—namely, spray rails, chine strips, and V-shaped spray interceptors (VSI)—with particular emphasis on operation at lower volumetric Froude numbers ($Fr_\nabla < 3.65$). The work combined a systematic experimental campaign comprising 228 towing tests with a complementary numerical study using verified and validated CFD models. Together, these efforts provided a consistent understanding of how geometric details, flow regimes, and numerical modelling assumptions influence resistance and running attitude, and whether numerical tools can be relied upon in the early design stages of such craft.

The research is guided by the following questions:

Q1 ***How do the geometry and arrangement of spray-control appendages affect the resistance and running attitude of a hard-chine planing hull at moderate planing speeds ($Fr_\nabla < 3.65$)?***

Q2 ***Under which modelling assumptions can CFD reliably reproduce experimentally observed appendage-induced trends, and how can such validated simulations be applied for comparative design assessment of appended planing hulls?***

In response to RQ1, the experimental results quantify the influence of spray-rail geometry on hydrodynamic performance. The experimental findings showed that spray rails can both improve and impair hydrodynamic performance depending on the Froude number and geometric configuration. At higher length–displacement ratios ($Ⓜ \geq 5.174$) and planing speeds ($Fr_\nabla \geq 3$), spray rails reduced total resistance by up to 2.4%, confirming their potential to deflect spray and reduce wetted area in the planing regime. However, at lower speeds ($Fr_\nabla < 2.5$), the same appendages increased resistance by as much as 8.3%, primarily due to the increased running trim caused by additional lift in the forebody. Between $Fr_\nabla = 2.5$ and 3.0, their effect was negligible, often within the experimental uncertainty of 0.4%. Geometrically, increasing the spray rail width and the magnitude of its bottom angle tended to worsen performance by increasing forebody lift and running trim. In contrast, narrow triangular spray rails ($b_{SR} = 2$ mm, $\delta = -25°$) performed best, achieving effective spray separation without generating excessive lift. The combined findings confirm established design guidelines, emphasizing that spray rails should be small, short, and angled upward to avoid excessive lift and drag. The experiments further clarified that the critical geometric factor is the vertical distance between the rail's outer edge and the bottom surface, which depends jointly on the width and the angle of the rail—this parameter governs the effectiveness of spray deflection.

Further addressing RQ1, the results demonstrate that chine strips significantly affect resistance and running attitude through speed-dependent changes in lift distribution. At planing speeds ($Fr_\nabla > 2.5$), chine strips increased lift aft of the centre of gravity, reduced trim by up to 0.3°, and decreased resistance by as much as 3%. At semi-displacement speeds ($Fr_\nabla < 2.5$), the opposite occurred: the strips induced lift forward of the centre of gravity, increasing trim and total resistance by similar magnitudes. Thus, chine strips are beneficial only in the planing regime and should be geometrically limited to the aft region, extending only slightly forward of the spray edge line and no further than the dynamic waterline at maximum speed ($Fr_\nabla = 3.261$). While less effective than stern interceptors—which can reduce resistance by more than 15% and trim by over one

degree—chine strips offer a simpler and more cost-efficient solution for moderate trim control. However, they do not substitute for interceptors or trim tabs when performance improvements are required in semi-displacement conditions.

Finalising the analysis of RQ1, the behaviour of V-shaped spray interceptors was evaluated experimentally at low planing speeds. The experimental findings confirmed that VSIs can indeed reduce total resistance even below $Fr_\nabla = 3.3$. Positioned forward of the stagnation line, the interceptors deflected the oncoming spray and generated a reaction force in the direction of motion, leading to resistance reductions of up to 3% under the design condition ($Fr = 1.355$, $Fr_\nabla = 3.108$, Ⓜ = 4.978). However, the VSI induced reaction force only reduced resistance by approximately 1.6 %. The remaining resistance reduction resulted from the absence of the pressure and frictional resistance contributions associated with spray rails, rather than from the reaction force generated by the VSI itself. Comparable performance was observed across a range of length–displacement ratios, indicating robustness of the effect. These results extend the applicability of VSI devices to lower-speed planing regimes. However, resistance penalties of up to 8% under off-design (semi-displacement) conditions indicate that further optimisation of the VSI concept is required.

In response to RQ2, a systematic verification and validation study was conducted to evaluate the ability of CFD to reproduce experimentally observed trends. The verification and validation campaign provided a systematic assessment of this issue. Simulations resolving the viscous sublayer directly ($y^+ < 5$) consistently underestimated running trim by 5–18% and total resistance by 2–7%, failing to meet the validation criteria. Models employing wall functions ($y^+ > 30$), however, reproduced experimental resistance and trim within validation uncertainty, confirming the adequacy of such models for steady-state planing predictions under the investigated conditions. Furthermore, the study identified the omission of the towing force's trimming moment as a contributor to discrepancies in earlier CFD work. Including this force increased the predicted running trim by 0.1°–0.4°, particularly in semi-displacement regimes, thereby improving agreement with experiments. This highlights the necessity of correctly modelling towing setups when comparing CFD results to tank data.

Expanding on RQ2, additional analyses showed that CFD predictions are sensitive to geometric representation and initial conditions. Comparing hulls with sharp and rounded chines revealed that although total resistance differed by only 0.1%, the running attitude changed significantly: rounded edges reduced sinkage by roughly 10% and increased trim by 1%, suggesting a measurable impact on lift distribution despite minimal change in overall drag. Quasi-static analyses of different degrees of freedom (2DOF vs 3DOF) showed that small initial biases in sinkage and trim—on the order of 0.001 m or 0.05°—can influence validation results given the small uncertainty bounds and should therefore be explicitly accounted for.

Addressing the application aspect of RQ2, the study assessed the capability of CFD to support comparative design decisions. The comparative simulations of hulls equipped with spray rails, chine strips, and VSIs revealed that CFD generally predicted smaller resistance variations than the experiments. While experimental resistance differences between configurations reached 2–3%, CFD results often fell within or just above the numerical uncertainty bounds, rendering many observed changes statistically insignificant. Consequently, although the current CFD models reproduced the principal experimental trends, the quantitative differences between appended configurations remained indicative rather than conclusive. The overall conclusion is that CFD can be a

valuable comparative design tool at the concept stage, provided its limitations in sensitivity and accuracy at low Froude numbers are acknowledged and validation against representative experiments is available.

Synthesizing the experimental and numerical findings, several broader implications emerge. First, the hydrodynamic behaviour of appendages in the low-planing regime is highly sensitive to geometric detail and flow condition, underscoring the need for carefully scaled model testing or validated simulations. Second, while spray rails and chine strips offer modest resistance reductions individually (2–3%), their combined application is likely to provide greater resistance reductions under favourable planing conditions. However, benefits can diminish or reverse at lower speeds due to increased trim. Third, the inclusion of towing forces and appropriate near-wall modelling are critical for achieving CFD reliability comparable to physical testing. Finally, the study confirms that while experimental methods remain indispensable for quantitative evaluation, well-verified CFD can support early-stage design optimization by revealing relative trends and interactions among hull appendages.

In conclusion, this integrated experimental and numerical investigation provides quantitative evidence clarifying the hydrodynamic roles of spray rails, chine strips, and V-shaped spray interceptors in the low-planing regime. It resolves several open questions identified in the problem statement, confirms and refines established design guidelines, and delineates the operational and methodological limits of current CFD practice. These findings contribute to more informed and reliable early-stage design of planing craft, where subtle geometric and dynamic interactions strongly affect performance. Future work should extend these investigations to higher Froude numbers, incorporate dynamic seakeeping conditions, and explore optimization of combined appendage configurations using advanced CFD–experiment hybrid approaches.

References

Avci, A. G., & Barlas, B. (2019). An experimental investigation of interceptors for a high speed hull. *International Journal of Naval Architecture and Ocean Engineering*, *11*(1), 256–273. https://doi.org/10.1016/j.ijnaoe.2018.05.001

Begovic, E., & Bertorello, C. (2012). Resistance assessment of warped hull form. *Ocean Engineering*, *56*, 28–42. https://doi.org/10.1016/j.oceaneng.2012.08.004

Blanchard, U. J. (1952). *The Planing Characteristics of a Surface Having a Basic Angle of Dead Rise of 40 Degrees and Horizontal Chine Flare* (2842; NACA Technical Note). https://ntrs.nasa.gov/citations/19930083590

Castaldi, L., Osmak, F., Green, M., Fürth, M., & Bonoli, J. (2021). The effect of spray deflection on the performance of high speed craft in calm water. *Ocean Engineering*, *229*(April), 108892. https://doi.org/10.1016/j.oceaneng.2021.108892

Celik, I. B., Ghia, U., Roache, P. J., Freitas, C. J., Coleman, H., & Raad, P. E. (2008). Procedure for estimation and reporting of uncertainty due to discretization in CFD applications. *Journal of Fluids Engineering, Transactions of the ASME*, *130*(7), 0780011–0780014. https://doi.org/10.1115/1.2960953

Chambliss, D. B., & Boyd, G. M. (1953). *The Planing Characteristics of Two V-shaped Prismatic Surfaces Having Angles of Dead Rise of 20 Degrees and 40 Degrees* (2876; NACA Technical Note).

Clement, E. P. (1964a). *Effects of Longitudinal Bottom Spray Strips on Planing Boat Resistance* (1818; Report). https://dome.mit.edu/handle/1721.3/49089?show=full

Clement, E. P. (1964b). *Reduction of Planing Boat Resistance by Deflection of the Whisker Spray* (1929; Report). https://dome.mit.edu/handle/1721.3/49020?show=full

Cui, L., Chen, Z., Feng, Y., Li, G., & Liu, J. (2021). An improved VOF method with anti-ventilation techniques for the hydrodynamic assessment of planing hulls-Part 2: Applications. *Ocean Engineering*, *237*, 109505. https://doi.org/10.1016/j.oceaneng.2021.109505

De Luca, F., Mancini, S., Miranda, S., & Pensa, C. (2016). An extended verification and validation study of CFD simulations for planing hulls. *Journal of Ship Research*, *60*(2), 101–118. https://doi.org/10.5957/JOSR.60.2.160010

De Luca, F., Mancini, S., Pensa, C., & Staiano, G. (2014). Numerical evaluation (CFD) of Wake and Thrust deduction fraction of a Warped Hard Chine Hulls Systematic Series. *10th RINA High Speed Marine Vehicles Symposium*, (October 2014), 1–8.

De Luca, F., & Pensa, C. (2012). Experimental Investigation on Conventional and Unconventional Interceptors. *Transactions RINA, International Journal of Small Craft Technology*, *154*(B2), 65–72. https://doi.org/10.3940/rina.ijsct.2012.b2.129

Eça, L., & Hoekstra, M. (2014). A procedure for the estimation of the numerical uncertainty of CFD calculations based on grid refinement studies. *Journal of Computational Physics*, *262*, 104–130. https://doi.org/10.1016/j.jcp.2014.01.006

Eça, Luis., & Hoekstra, M. (2006). Discretization Uncertainty Estimation based on a Least Squares version of the Grid Convergence Index. *Proceedings of the Second Workshop on CFD Uncertainty Analysis*, (October), 1–27.

Gray-Stephens, A., Tezdogan, T., & Day, S. (2019). Strategies to minimise numerical ventilation in CFD simulations of high-speed planing hulls. *Proceedings of the International Conference on Offshore Mechanics and Arctic Engineering - OMAE*, *2*, 1–10. https://doi.org/10.1115/OMAE2019-95784

Grigoropoulos, G., & Loukakis, T. (1995). Effect of Spray Rails on the Resistance of Planing Hulls. *3rd Intl. Symposium on Fast Sea Transportation FAST'95*, (September).

ITTC. (2017a). 7.5-02-02-01 Resistance Test. *28th International Towing Tank Conference, Recommended Procedures and Guidelines, Procedure 7.5-02-02-01*. https://www.ittc.info/media/8001/75-02-02-01.pdf

ITTC. (2017b). 7.5-03-02-03 Practical Guidelines for Ship CFD Applications. *28th International Towing Tank Conference, Recommended Procedures and Guidelines*, 1–15.

ITTC. (2021). 7.5-03-01-01 Uncertainty Analysis in CFD Verification and Validation, Methodology and Procedures. *29th International Towing Tank Conference, Recommended Procedures and Guidelines*, 1–15. https://www.ittc.info/media/9765/75-03-01-01.pdf

Judge, C., Mousaviraad, M., Stern, F., Lee, E., Fullerton, A., Geiser, J., Schleicher, C., Merrill, C., Weil, C., Morin, J., Jiang, M., & Ikeda, C. (2020). Experiments and CFD of a high-speed deep-V planing hull—Part I: Calm water. *Applied Ocean Research*, *96*, 102060. https://doi.org/10.1016/j.apor.2020.102060

Kapryan, W. J., & Boyd, G. M. (1953). *The Effect of Vertical Chine Strips on the Planing Characteristics of V-Shaped Prismatic Surfaces Having Angles of Dead Rise of 20 Degrees and 40 Degrees* (3052; NACA Technical Note). https://ntrs.nasa.gov/citations/19930083704

Kapryan, W. J., & Weinstein, I. (1952). *The Planing Characteristics of a Surface Having a Basic Angle of Dead Rise of 20 Degrees and Horizontal Chine Flare* (2804; NACA Technical Note). https://ntrs.nasa.gov/citations/19930083524

Karimi, M. H., Seif, M. S., & Abbaspoor, M. (2013). An experimental study of interceptor's effectiveness on hydrodynamic performance of high-speed planing crafts. *Polish Maritime Research*, *20*(2), 21–29. https://doi.org/10.2478/pomr-2013-0013

Larsson, L., Eliasson, R. E., & Orych, M. (2014). *Principles of Yacht Design* (4th Revise). Adlard Coles nautical.

Lee, Y. G., Kim, C., Park, J. H., Kim, H., Lee, I., & Jin, B. (2019). Numerical simulations of added resistance in regular head waves on a container ship. *Brodogradnja*, *70*(2). https://doi.org/10.21278/BROD70204

Mansoori, M., & Fernandes, A. C. (2017). Interceptor and trim tab combination to prevent interceptor's unfit effects. *Ocean Engineering*, *134*(March), 140–156. https://doi.org/10.1016/j.oceaneng.2017.02.024

Mansoori, M., Fernandes, A. C., & Ghassemi, H. (2017). Interceptor design for optimum trim control and minimum resistance of planing boats. *Applied Ocean Research*, *69*, 100–115. https://doi.org/10.1016/j.apor.2017.10.006

Molchanov, B., Lundmark, S., Fürth, M., & Green, M. (2019). Experimental validation of spray deflectors for high speed craft. *Ocean Engineering*, *191*(April), 106482. https://doi.org/10.1016/j.oceaneng.2019.106482

Müller-Graf, B. (1991). The Effect of an Advanced Spray Rail System on Resistance and Development of Spray of Semi-Displacement Round Bilge Hulls. In K. O. Holden, O. M. Faltinsen, & T. Moan (Eds.), *FAST '91, 1st Intl Conf on Fast Sea Transportation* (pp. 125–141). Tapir Publishers.

Niazmand Bilandi, R., Mancini, S., Dashtimanesh, A., & Tavakoli, S. (2024). A revisited verification and validation analysis for URANS simulation of planing hulls in calm water. *Ocean Engineering*, *293*, 116589. https://doi.org/10.1016/J.OCEANENG.2023.116589

Olin, L., Altimira, M., Danielsson, J., & Rosén, A. (2016). Numerical modelling of spray sheet deflection on planing hulls. *Proceedings of the Institution of Mechanical Engineers, Part M: Journal of Engineering for the Maritime Environment*, *231*(4), 811–817. https://doi.org/10.1177/1475090216682838

Park, J. Y., Choi, H., Lee, J., Choi, H., Woo, J., Kim, S., Kim, D. J., Kim, S. Y., & Kim, N. (2019). An experimental study on vertical motion control of a high-speed planing vessel using a controllable interceptor in waves. *Ocean Engineering*, *173*(February 2018), 841–850. https://doi.org/10.1016/j.oceaneng.2019.01.019

Savitsky, D. (1964). Hydrodynamic Design of Planing Hulls. *Marine Technology and SNAME News*, *1*(04), 71–95. https://doi.org/10.5957/mt1.1964.1.4.71

Savitsky, D., DeLorme, M. F., & Datla, R. (2007). Inclusion of Whisker Spray Drag in Performance Prediction Method for High-Speed Planing Hulls. *Marine Technology*, *44*(1), 35–56.

Savitsky, D., & Morabito, M. (2011). Origin and Characteristics of the Spray Patterns Generated by Planing Hulls. *Journal of Ship Production & Design*, *27*(2), 63–83.

Seok, W., Park, S. Y., & Rhee, S. H. (2020). An experimental study on the stern bottom pressure distribution of a high-speed planing vessel with and without interceptors. *International Journal of Naval Architecture and Ocean Engineering*, *12*, 691–698. https://doi.org/10.1016/j.ijnaoe.2020.08.003

SIEMENS PLM. (2022). *Simcenter STAR-CCM+ 2210 Build 17.06.007 User Guide*.

Stern, F., Wilson, R., & Shao, J. (2006). Quantitative V&V of CFD simulations and certification of CFD codes. *International Journal for Numerical Methods in Fluids*, *50*(11), 1335–1355. https://doi.org/10.1002/fld.1090

Stern, F., Wilson, R. V., Coleman, H. W., & Paterson, E. G. (2001). Comprehensive approach to verification and validation of CFD simulations—Part 1: Methodology and procedures. *Journal of Fluids Engineering, Transactions of the ASME*, *123*(4), 793–802. https://doi.org/10.1115/1.1412235

Tavakoli, S., Zhang, M., Kondratenko, A. A., & Hirdaris, S. (2024). A review on the hydrodynamics of planing hulls. In *Ocean Engineering* (Vol. 303). Elsevier Ltd. https://doi.org/10.1016/j.oceaneng.2024.117046

Viola, I. M., Flay, R. G. J., & Ponzini, R. (2012). CFD analysis of the hydrodynamic performance of two candidate America's Cup AC33 hulls. *Transactions of the Royal Institution of Naval Architects Part B: International Journal of Small Craft Technology*, *154*(PART B1). https://doi.org/10.3940/rina.ijsct.2012.b1.113

Wagner, H. (1932). Über Stoß- und Gleitvorgänge an der Oberfläche von Flüssigkeiten. *ZAMM - Journal of Applied Mathematics and Mechanics / Zeitschrift Für Angewandte Mathematik Und Mechanik*, *12*(4), 193–215. https://doi.org/10.1002/zamm.19320120402

Wheeler, M. P., Ryan, P., & Cimolin, F. (2021). Using VOF Slip Velocity to Improve Productivity of Planing Hull CFD Simulations. *SNAME International Conference on Fast Sea Transportation 2021. FAST 2021*, (October), 26–27. https://doi.org/10.5957/FAST-2021-013

Wilson, R. V., Carrica, P. M., & Stern, F. (2006). Unsteady RANS method for ship motions with application to roll for a surface combatant. *Computers and Fluids*, *35*(5), 501–524. https://doi.org/10.1016/j.compfluid.2004.12.005

Acknowledgements

I wish to express my sincere appreciation to all individuals and institutions whose support has contributed to the successful completion of this doctoral dissertation. Their guidance, expertise, and encouragement have been invaluable throughout the research process.

This work was supported by the Estonian Research Council through grants PRG83 (Numerical simulation of the FSI for the dynamic loads and response of ships) and PRG1820 (Dynamic response of offshore structures), and by the European Regional Development Fund grant F19042 (Small Craft Competence Centre – analysis of outer construction elements impact on the performance of a vessel, transition of know-how and information). The authors gratefully acknowledge this support.

I extend my deepest gratitude to my supervisor, Professor Kristjan Tabri, for his insightful guidance, unwavering support, and dedication to scientific rigor. His thoughtful feedback and commitment to academic excellence have significantly shaped the development and quality of this work.

My gratitude extends to the former and current Directors of TalTech Kuressaare College, Anni Hartikainen and Merit Kindsigo, whose contributions in project administration and funding acquisition were instrumental in enabling this research.

I would also like to acknowledge my co-authors Tarmo Sahk, Risto Kaarma, Henrik Andreasson, Professor Mihkel Kõrgesaar, Professor Abbas Dashtimanesh, Professor Simone Mancini, and Rasul Niazmand Bilandi Ph.D. Their scholarly contributions, constructive discussions, and collaborative engagement have been integral to the research outcomes and publications associated with this dissertation.

My sincere thanks go to Ruttar Teär and Tarmo Sahk, whose dedicated work on the experimental campaign — including the most demanding practical tasks — was essential to the successful progress of this research. Their commitment, reliability, and problem-solving ability made a substantial contribution to the experimental components of this study.

Finally, I wish to express my heartfelt gratitude to my family. Their patience, understanding, and unwavering encouragement have been fundamental to the completion of this dissertation. Their support has sustained me through both the challenges and achievements of this academic journey, and for this I am profoundly grateful.

Abstract

Experimental and Numerical Investigation of Spray-Control Appendages on Low-Planing Hard-Chine Hulls

The hydrodynamic role of spray-control appendages, particularly spray rails, remains insufficiently quantified despite their widespread use on planing craft. Existing design guidance is largely empirical, while systematic experimental studies are limited by the cost and duration of towing-tank testing. Although computational fluid dynamics (CFD) offers a potential means of reducing experimental effort, published simulations of planing hulls often exhibit resistance discrepancies of 10–20% relative to experiments, limiting their reliability for design applications.

This thesis presents a combined experimental and numerical investigation aimed at quantifying the hydrodynamic effects of spray-control appendages and establishing a CFD modelling strategy capable of reproducing experimentally observed resistance and running-attitude trends within validation uncertainty. Spray rails form the primary focus, while chine strips and a V-shaped spray interceptor (VSI) are also examined to assess a broader range of spray management concepts and to challenge the numerical models with geometrically diverse appendages.

A towing-tank campaign was conducted on a low-planing craft model operating from the semi-displacement to fully planing regime. The hull was tested in bare and appended configurations, including narrow and wide spray rails with varying bottom angles, chine strips, and a VSI. Total resistance, trim angle, and sinkage were measured for each configuration under calm-water conditions, producing a dataset of 228 test cases structured to enable direct experimental–numerical comparison.

The experiments indicate that, within the investigated speed range, resistance optimisation through spray rail design is limited. Under planing conditions, well-dimensioned spray rails reduced total resistance by approximately 2–3%, with negligible influence on trim, while oversized or excessively long rails increased resistance by up to 8% due to increased trim and wetted area. Narrow spray rails with downward-inclined deflection surfaces outperformed conventional horizontal designs, suggesting that rail breadth alone is not a dominant parameter. Chine strips reduced resistance by up to 3% and trim by approximately 0.3° at planing speeds but increased resistance in the semi-displacement regime. The VSI showed strong sensitivity to its position relative to the speed-dependent stagnation line, reducing resistance by up to 4.2% when located ahead of the stagnation line, and increasing resistance by up to 8.4% when located aft.

Complementary CFD simulations were performed using a Reynolds-Averaged Navier-Stokes free-surface approach. The results demonstrate strong sensitivity to force balance, motion modelling, and near-wall treatment. Wall-function-based models combined with appropriate representation of towing force and hull motion reproduced experimental resistance and trim within validation uncertainty, with three-degree-of-freedom motion providing the most consistent agreement across speeds.

Overall, the study shows that spray-control appendages can yield modest but measurable resistance reductions, while poorly designed configurations may incur significant penalties. It further demonstrates that CFD, when carefully validated against targeted experimental data, can serve as a reliable tool for comparative assessment and trend analysis of spray-control appendages on planing hulls.

Lühikokkuvõte

Pritsmeliistude eksperimentaalne ja numbriline uurimine aeglaselt glisseerivatel teravkimmilistel laevakeredel

Teravkimmiliste laevakerede pritsmekaitsmete, eriti pritsmeliistude, hüdrodünaamiline roll on vaatamata nende ulatuslikule kasutusele liugkeredel endiselt ebapiisavalt kvantifitseeritud. Olemasolevad projekteerimissuunised on valdavalt empiirilised, samal ajal kui süstemaatilisi uuringuid piiravad katsete maksumus ja kestus. Kuigi arvutuslik vedelikudünaamika (CFD) võimaldab vähendada katsete mahtu, esineb avaldatud liugkerede CFD uuringutes sageli 10–20% erinevusi kogutakistuse ennustustes võrreldes katsetulemustega, mis piirab nende kasutatavust projekteerimisel.

Käesolev väitekiri käsitleb kombineeritud eksperimentaal- ja numbrilist uurimistööd, mille eesmärk on kvantifitseerida pritsmekontrolli lisaseadmete hüdrodünaamilised mõjud ja määrata CFD-modelleerimise strateegia kogutakistuse ja käiguasendi trendide taastootmiseks valideerimismääramatuse piires. Põhirõhk on pritsmeliistudel, kuid võrdluseks käsitletakse ka kimmiliiste ja V-kujulisi pritsmeliiste, et hinnata erinevaid pritsme ohjamise lahendusi ning testida numbriliste mudelite sobivust erineva geomeetriaga lisaseadmete korral.

Eksperimentaalne uuring viidi läbi liugkere mudelil kiiruse vahemikus, mis hõlmab üleminekupiirkonda poolväljasurve- ja täieliku glisseerimise tingimuste vahel. Mudelit testiti nii paljaskerena kui ka erinevate pritsmekontrolli lisaseadmetega. Iga konfiguratsiooni kohta mõõdeti tasase vee tingimustes kogutakistust, trimmi ning vajumist. Saadud andmestik hõlmas 228 katsejuhtumit ning seda kasutati numbriliste tulemuste valideerimiseks.

Katsetulemused näitasid, et uuritud kiirusvahemikus oli takistuse optimeerimine pritsmeliistude abil piiratud. Glisseerimiskiirustel vähendasid väikeste mõõtmetega pritsmeliistud kogutakistust 2–3%, mõjutamata oluliselt trimmi. Ülemõõdulised pritsmeliistud suurendasid kogutakistust kuni 8% trimmi ja märgpinna suurenemise tõttu. Allapoole kaldu suunatud kitsad pritsmeliistud osutusid tõhusamaks kui tavapärased horisontaalsed lahendused, mis viitab sellele, et üksnes pritsmeliistu laius ei ole määrav parameeter. Glisseerimiskiirustel vähendasid kimmiliistud kogutakistust kuni 3% ja trimmi kuni 0,3°, kuid poolväljasurve režiimis suurendasid need takistust. V-kujuliste pritsmeliistude mõju sõltus nende asendist kiirusest sõltuva stagnatsioonijoone suhtes: sellest eespool paiknedes vähendasid need kogutakistust kuni 4,2%, samas kui stagnatsioonijoonest tagapool paiknedes suurendasid need kogutakistust kuni 8,4%.

Numbrilised simulatsioonid viidi läbi Reynoldsi keskmistatud Navier-Stokesi võrrandite alusel vabapinna modelleerimisega. Tulemused näitasid, et jõutasakaalu kirjeldus, liikumismudel ja seinalähedane modelleerimine mõjutavad CFD tulemusi märkimisväärselt. Seinafunktsioonidel põhinevad mudelid koos sobiva pukseerimisjõu ja liikumise modelleerimisega taastootsid eksperimendis mõõdetud kogutakistuse ja trimmi valideerimismääramatuse piires, kusjuures kolme vabadusastmega mudel pakkus kõige järjepidevamat vastavust kogu uuritud kiiruste vahemikus.

Kokkuvõttes näitab töö, et pritsmekontrolli lisaseadmete abil on võimalik saavutada tagasihoidlikke, kuid mõõdetavaid vähenemisi kogutakistuses, samas kui ebasobiv projekteerimine võib põhjustada märkimisväärseid jõudluskaotusi. Uuring kinnitab, et hoolikalt valideeritud CFD metoodika sobib pritsmekontrolli lisaseadmete võrdlevaks hindamiseks ja trendianalüüsiks.

Appendix 1

Publication P1

Lakatos, M., Sahk, T., Kaarma, R., Tabri, K., Kõrgesaar, M., & Andreasson, H. (2019). Experimental testing of spray rails for the resistance reduction of planing crafts. In C. G. Soares & J. Parunov (Eds.), *Trends in the Analysis and Design of Marine Structures* (pp. 334–343). CRC Press. https://doi.org/10.1201/9780429298875-39

Trends in the Analysis and Design of Marine Structures – Parunov & Guedes Soares (Eds)
© 2019 Taylor & Francis Group, London, ISBN 978-0-367-27809-0

Experimental testing of spray rails for the resistance reduction of planing crafts

M. Lakatos, T. Sahk, R. Kaarma, K. Tabri & M. Kõrgesaar
Tallinn University of Technology, Estonia

H. Andreasson
Flow Naval Architects AB, Sweden

ABSTRACT: Spray rails, as well as the whole topic of spray sheet deflection, have been generally disregarded since the 1960s. Therefore, a series of model tests has been conducted with a 19 m craft configured with different spray rail arrangements (operating in a range of Froude numbers $Fr = 0.77 \ldots 1.35$). The model test series comprises five spray rail configurations: two chine modifications, two conventional spray rail configurations (with 2×2 mm and 5×5 mm rails) and a V-shaped spray rail arrangement. A number of significant findings are reported. A simple rectangular interceptor rail on the chine reduces the resistance of a planing craft by more than 3%. A V-shaped spray rail on the hull can reduce the resistance by up to 4%. Conventional spray rail set up reduces the resistance by nearly 2% at planing speeds. This publication sheds new light on well-known as well as recent concepts in planing craft design.

1 INTRODUCTION

Whisker spray is a phenomenon that occurs on high-speed marine vehicles (semi-displacement crafts, planing craft and hydroplanes) when they operate at high speeds. It is created from the stagnation line (a line that separates the flow going under the hull from the flow going into the spray area) and it forms a thin sheet of fluid along the bottom surface above the stagnation line, which under low-speed operation would have been dry (Fig. 1). This spray sheet of water causes a frictional resistance along its streamline over the hull surface. The resistance of whisker spray has been shown to account for 10% – 25% of total resistance (at high speed, when $Fr_\nabla > 4$) by inference from a comparison of model test data with and without spray rails installed on the hull bottom (Clement 1964a, b, Grigoropoulos & Loukakis 1995, Grigoropoulos 1997). As the speed increases, the ratio of whisker spray resistance to the total resistance increases as well.

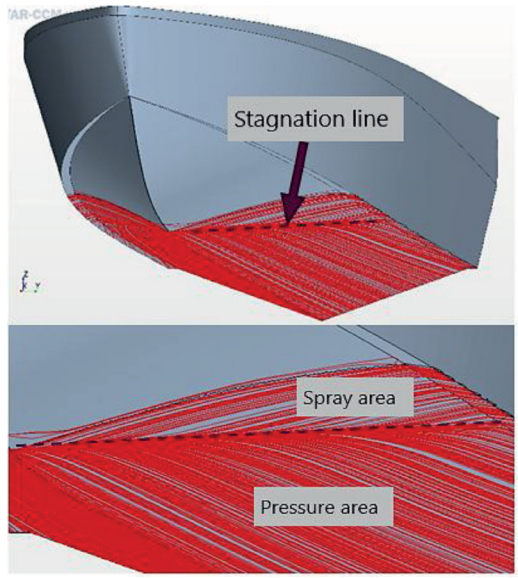

Figure 1. Bare Hull Streamlines at 5.7 m/s (full-scale 35 knots) 40 kg displacement.

In order to reduce the whisker spray resistance, two to four longitudinal stripes (also called rails, lifting strikes or deflectors) are usually installed on the hull. The main purpose of these appendages is to detach the spray from the hull surface and deflect it towards the sides or slightly down and aft-ward, thereby reducing the frictional resistance. Deflection of the spray also induces a lifting force that affects the running trim of the craft. Depending on the shape of the spray rail and the orientation of its deflecting surface, it is possible to generate different amount of lift form the spray. Since the running trim has a more significant effect on the total resistance than whisker spray, a spray rail will

reduce the resistance due to its lift producing qualities rather than due to its spray detachment abilities. On the other hand, the potential downside of spray rails is increasing vertical accelerations in waves and thus, reducing seakeeping properties.

At very high speeds the dynamic force from the water causes so much lift to the hull that the stagnation line reaches all the way to the transom.

With no clear chine, the hull can start to chine walk, i.e. wag from side to side or chine to chine. Chine walking is usually prevented by extending the outermost spray rail all the way to the transom. Then that spray rail acts as a second chine, producing a clear deflection line resulting in a more stable craft.

An analytical model (Savitsky et al. 2007) that predicts the viscous drag in the spray area as a function of deadrise angle, trim angle and speed has been added to the Savitsky method (Savitsky 1964), which previously only included the viscous and pressure drag components in the bottom area aft of the stagnation line.

In addition to whiskers spray, there is also a second spray pattern, called main spray (Savitsky & Breslin 2011), observed in planing crafts. It is a discharge of water in the form of a cone with its apex located near the intersection of the stagnation line and the chine. The outboard trajectory of the main spray is significantly elevated when compared to that of the whisker spray. Due to the large volume of water and the high trajectory angle of the main spray, it can impact the wings and propellers of seaplanes causing structural damage. It can also impact the tunnel between the hulls of a planing catamaran and thereby significantly increase in resistance. Savitsky & Morabito (2007) developed and experimentally verified an analytical model that predicts the geometry of the main spray as a function of deadrise angle, trim angle and speed.

Although the spray rails have a significant impact on the performance of high-speed marine vehicles, to the best knowledge of the authors, the shape and location of spray rails have been systematically investigated only by Müller-Graf (1991). Combined with a stern wedge, the advanced spray rail system (ASRS) proposed by the author reduced the resistance by 6% – 10% at $Fr > 0.4$. This concept was tested further by Grigoropoulos & Damala (1999), Bojovic & Sahoo (2000) and Bojovic et al. (2004). However, the aforementioned study concentrated on semi-displacement vessels, where spray formation and deflection phenomena are different from those of planing crafts.

A few studies featuring spray rails on planing hulls have been published within the last fifteen years. However, in most of those studies, the focus was on either on the validation of numerical models of planing hulls in calm water (Fu et al. 2010) and waves (Seo et al. 2016) or on the evaluation of new hull form concepts (Kim et al. 2013). Another recent study (Olin et al. 2016) suggests that by redirecting the flow on the bottom of the craft, spray energy can be recovered in order to propel the craft forward, thereby significantly reducing the total resistance compared to conventional spray rail set-up. However, only a prismatic hull shape (not a real craft hull) was considered in this study, while the influence of spray rails on craft's heave and pitch motion was neglected. In order to fill some of these gaps, a series of experiments has been conducted to show the influence of the shape and orientation of spray rails on the resistance and trim of a planing craft.

2 EXPERIMENTAL PROGRAMME

A test case craft has been designed and manufactured by the Small Craft Competence Centre (SCC) in Kuressaare, Estonia in order to compare conventional and novel spray rail configurations. The main particulars (Table 1) of the hull design are common for a high-speed patrol, search and rescue (SAR) craft or a larger pleasure craft. The craft is designed to operate at a displacement of 40 t and speed of 35 knots.

The spray rail series comprises five configurations (Table 2): two chine modifications, two conventional spray rail configurations (with 2×2 mm and 5×5 mm rails) and a V-shaped spray rail arrangement. Each configuration has been tested at four speeds corresponding to full scale (20, 25, 30 and 35 knots) at the model scale of 1:10 and four loading conditions (30 kg, 35 kg, 40 kg and 45 kg displacement).

In case of the first chine modification, a rectangular rail is attached to the hull along the outer edge of the chine (Fig. 2a), while in the second case, the rail covers the whole chine, resulting in a new chine surface angled down (Figs. 2b, 3).

Table 1. Main Dimensions of the naked hull.

Parameter		
Length overall	L_{OA}	1.921 m
Length between perpendiculars	L_{PP}	1.800 m
Length waterline	L_{WL}	1.703 m
Beam overall	B_{OA}	0.581 m
Beam waterline	B_{WL}	0.581 m
Draught	T	0.108 m
Displacement mass	Δ_m	40 kg
Displacement volume	∇	0.040 m^3
Longitudinal Centre of Gravity	L_{CG}	0.669 m
Vertical Centre of Gravity	KG	0.200 m

Table 2. Test matrix of the spray rail series.

Fr [–]	Δ_m [kg]	Spray rail type	Spray rail profile	Size [mm]
0.769	30	Chine spray rail (CSR)	Rectangular	2 × 2
0.961	35			
1.153	40	Chine inclination (C.INC)	Triangular	2 × 15
1.345	45			
		Spray Rail 1 (SR1)	Rectangular	2 × 2
				5 × 5
			Triangular	2 × 2
				5 × 5
		Spray Rail 1 (SR1)	Rectangular	2 × 2
				5 × 5
			Triangular	2 × 2
				5 × 5
		V-shaped Spray Rail (VSR)	Triangular	5 × 5

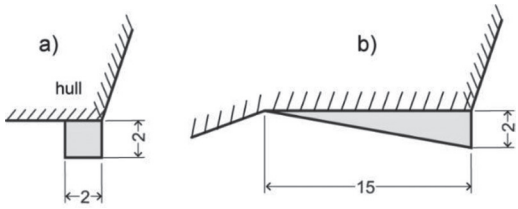

Figure 2. Profiles of the chine spray rail (a) and the chine inclination (b).

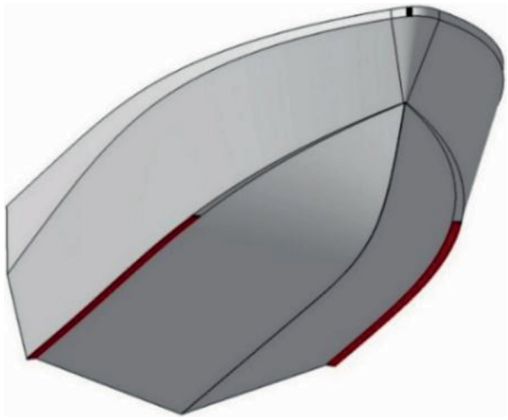

Figure 3. Chine spray rail.

In the first conventional arrangement, the spray rails are limited by the dynamic waterline (Fig. 4a) while in the second arrangement, the spray rails extend up to the transom (Fig. 4b). The spray rails are modelled with two different profiles: a rectangular profile (Fig. 5a) with the deflection surface perpendicular to the hull and a triangular (Fig. 5b) profile with the hypotenuse being attached to the hull.

The V-shape arrangement (Fig. 4c) is modelled with a triangular profile (Fig. 5c) with the deflection surface perpendicular to the hull. The V-shaped spray rail has been designed for the displacement of 40 kg and speed of 5.7 m/s, which is equivalent to 40 t and 35 knots in full-scale.

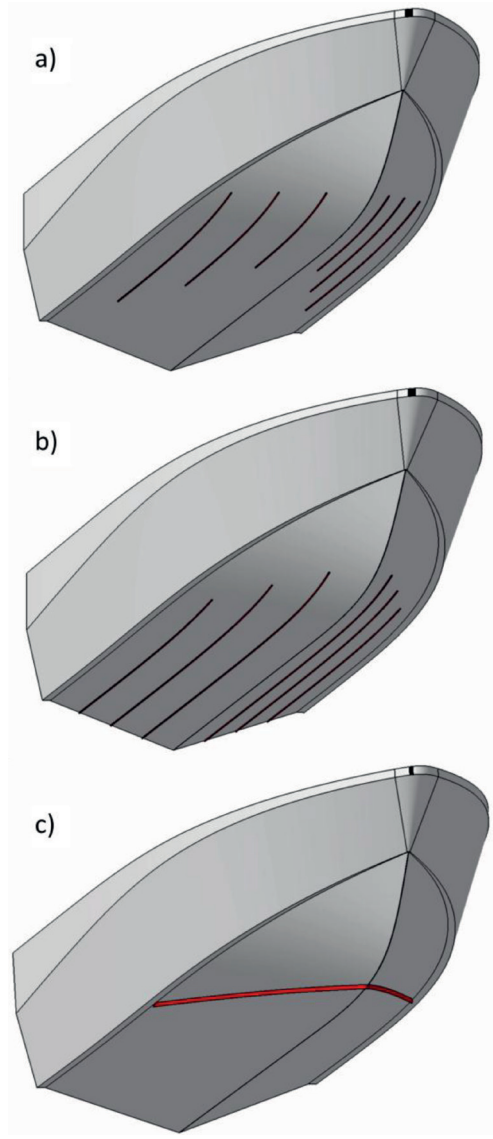

Figure 4. Conventional spray rail configurations: a) limited spray rails (SR1), b) spray rails extending to the transom (SR2) and c) V-shaped spray rail (VSR) configuration.

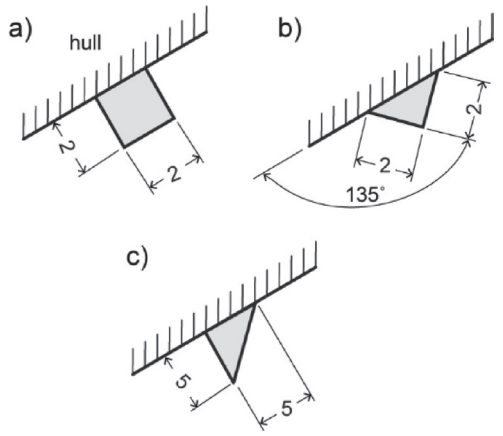

Figure 5. Spray rail profiles: a) rectangular, b) triangular and c) triangular profile with the deflection surface normal to the hull.

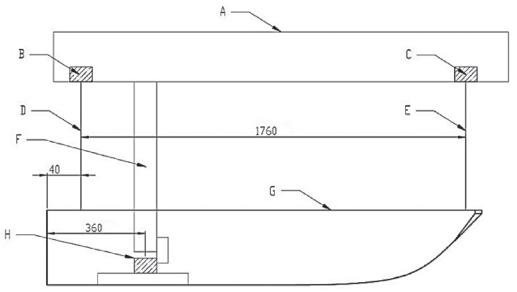

Figure 6. Semi-captive model test setup: A – carriage, B & C – wire encoder, D & E – linear measuring wire, F – carriage arm, G – test model, H – force gauge.

Table 3. Dimensions of the tank.

Parameter		
Maximum tank length	l	60 m
Maximum tank breadth	b	5 m
Maximum tank depth	h	3 m

2.1 *Test setup*

The models were tested in semi-captive condition (Fig. 6), i.e. the models were free to heave and pitch. During the tests, resistance and draught changes were measured. The trim of the craft was evaluated from the readings of draught change in the aft and the bow. The resistance is measured at 20 Hz sampling frequency, with 2–3 repeated runs at low speeds and 3–4 repeated runs at high speeds. The dimensions of the model test tank are given in Table 3 while the properties of the measurement equipment are given in Table 4.

Table 4. Properties of the measurement equipment.

Device	Max value	Absolute accuracy	Relative Accuracy
Kübler Sendix 5000	15 m/s	± 0.03 m/s	± 0.2%
Kübler Draw Wire Encoder A50 (Fig. 6b, c)	1250 mm	± 0.625 mm	± 0.05%
Tecsis S-beam load cell F2211 (Fig. 6h)	0.2 kN	± 0.4 N	± 0.2%

3 RESULTS

The bow views of the model planing at the Froude number of Fr = 1.345 at 40 kg displacement are shown in Figure 7. The total resistance and trim are presented in Figures 8–13 and 15–16 as functions of Froude number Fr, which is based on the craft's length between perpendiculars L_{PP} = 1.8 m for the purpose of better visualisation.

The spray rail arrangements are compared to the bare hull in terms of total resistance and trim in semi-displacement ($Fr < 1$) and planing ($Fr > 1$) regimes. In addition, total resistance and trim are analysed in light (Δ_m = 30 kg and Δ_m = 35 kg) and heavy (Δ_m = 40 kg and Δ_m = 45 kg) loading conditions. The uncertainty of resistance at a speed point varies in a range of 0.3% – 1.91% with an average of 0.7%.

3.1 *Chine modifications*

The total resistance and trim of the chine spray rail (CSR) and chine inclination (C.INC) are compared to those of the bare hull (BH) in Figures 8 and 9 respectively.

3.1.1 *Chine spray rail*

The chine spray rail (CSR) (Figs. 2a, 3) has a rather beneficial influence on the performance of the craft through the most part of the range of speeds and loading conditions.

Compared to the bare hull, in light loading conditions, the chine spray rail increases the total resistance (Fig. 8) by 2.5% – 2.9% in the semi-displacement regime and reduces it by up to 2.5% when the craft is planing. However, when operating in heavy loading conditions the resistance change is negligible in the semi-displacement regime and by 3.5% lower when the craft is planing.

The chine spray rail increases the running trim (Fig. 9) in the semi-displacement regime and reduces it in planing, which to some extent explains the effect on the resistance. However, the

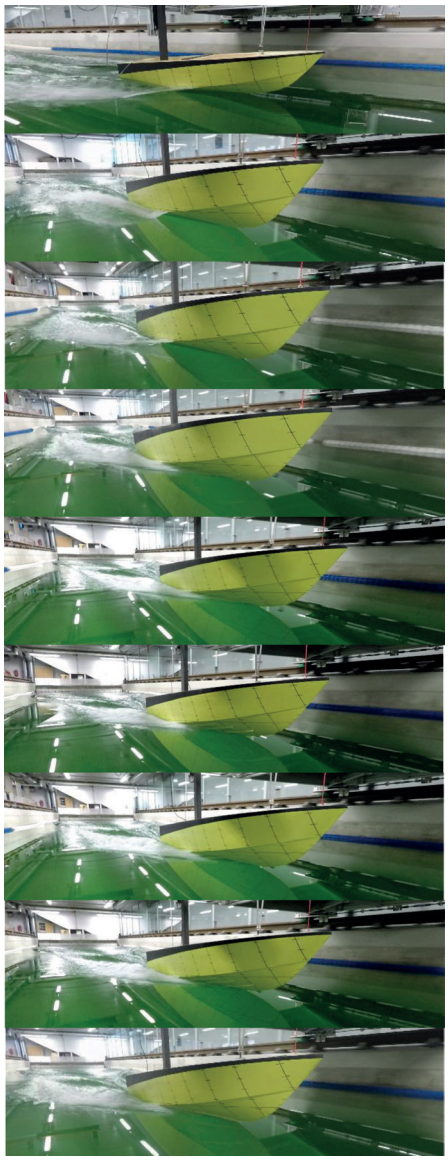

Figure 7. Spray formation of the model planing at the Froude number of $Fr = 1.345$ at 40 kg displacement (top to bottom: Bare hull, Chine Spray Rail, Chine Inclination, Spray rail SR1 with rectangular 2×2 mm profile, Spray rail SR2 with rectangular 2×2 mm profile Spray Rail SR1 with rectangular 5×5 mm profile, Spray Rail SR1with triangular 2×2 mm profile, Spray rail SR1 with triangular 5×5 mm profile, V-shaped spray rail).

trim change is dependent on the displacement. The heavier the craft, the smaller is the trim change. Lower running trim is expected to reduce resistance in the investigated speed range.

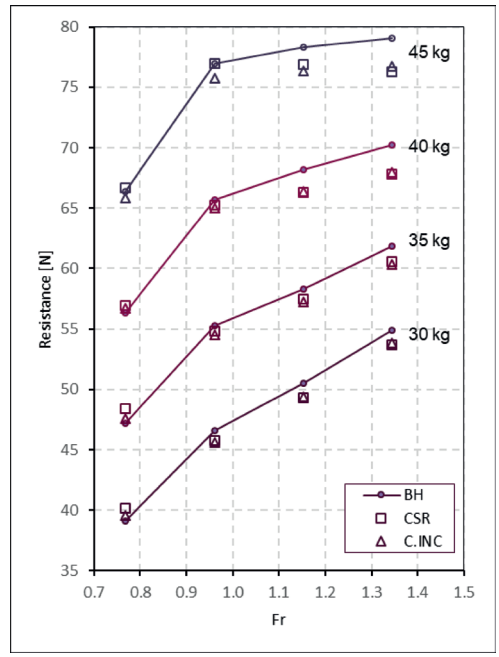

Figure 8. Resistance data for chine spray rail (CSR) and chine inclination (C.INC) compared to the bare hull (BH).

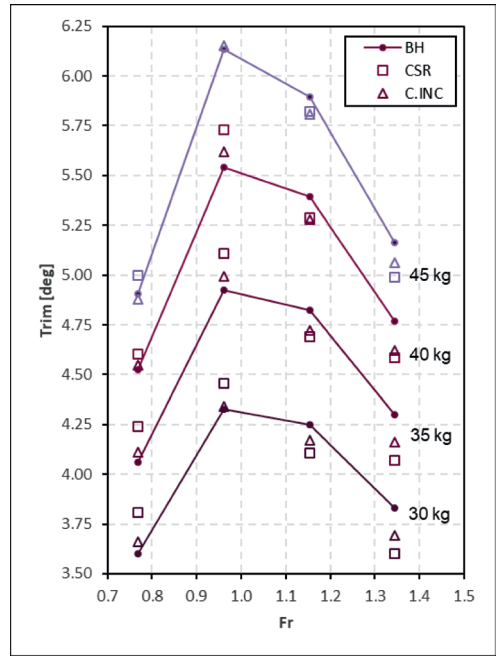

Figure 9. Trim data for chine spray rail (CSR) and chine inclination (C.INC) compared to the bare hull (BH).

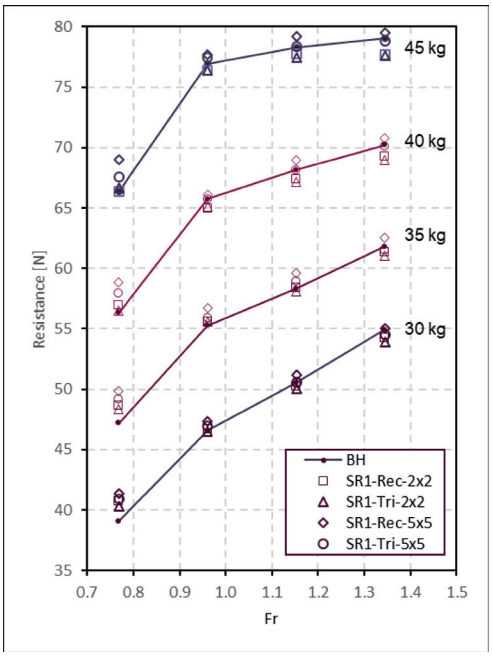

Figure 10. Resistance data of the spray rail arrangement SR1 with rectangular (Rec) and triangular (Tri) 2×2 mm and 5×5 mm profile compared to the bare hull (BH).

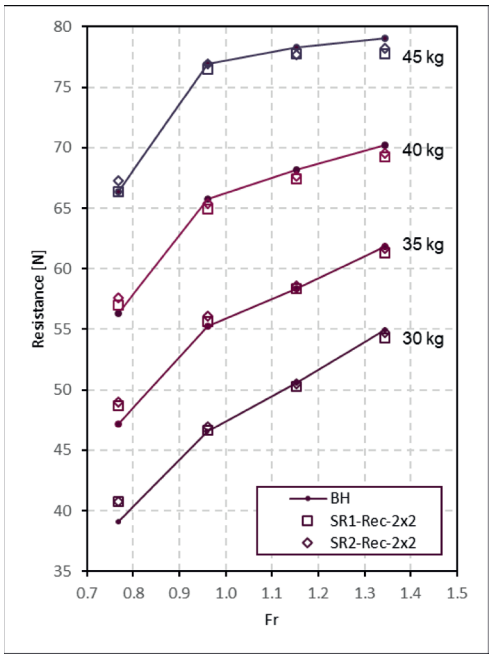

Figure 12. Resistance data of the spray rail arrangements SR1 & SR2 with rectangular 2×2 mm profile compared to the bare hull (BH).

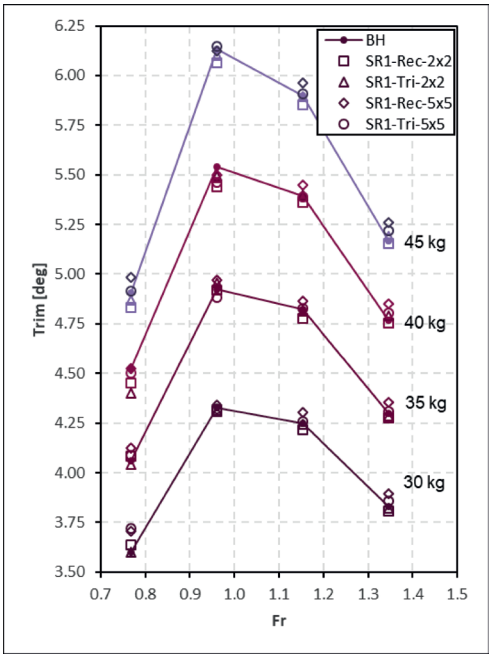

Figure 11. Trim data of the spray rail arrangement SR1 with rectangular (Rec) and triangular (Tri) 2×2 mm and 5×5 mm profiles compared to the bare hull (BH).

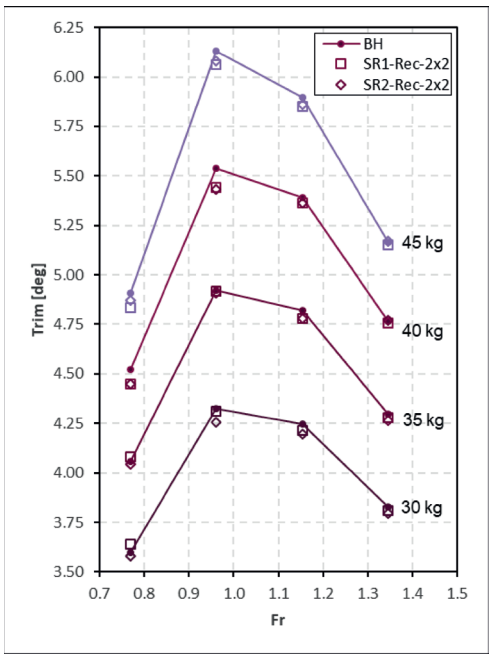

Figure 13. Trim data of the spray rail arrangements SR1 & SR2 with rectangular 2×2 mm profile compared to the bare hull (BH).

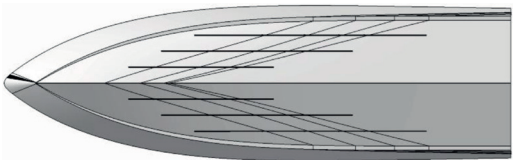

Figure 14. Waterlines of the hull with spray rail arrangement SR1 at tested speeds at 40 kg displacement.

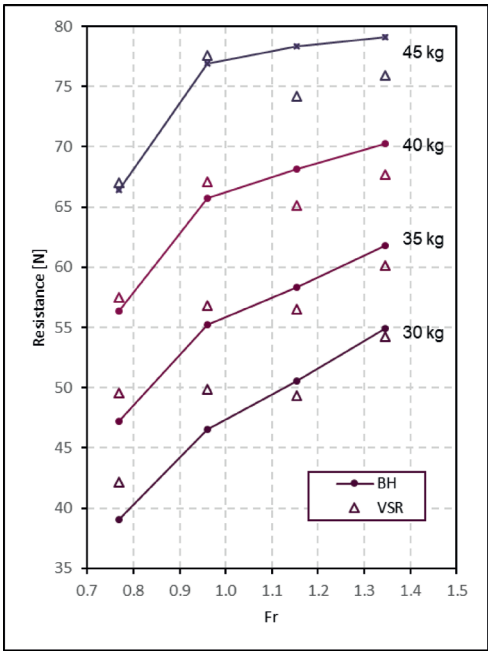

Figure 15. Resistance data of the V-shaped spray rail (VSR) compared to the bare hull (BH).

3.1.2 *Chine inclination*

Compared to the bare hull, in light loading conditions, the chine inclination (C.INC) (Figs. 2b, 3) increases the total resistance (Fig. 8) by 0.9% – 1.3% in the semi-displacement regime and reduces it by up to 2.3% when the craft is planing. However, when operating in heavy loading conditions the resistance change is negligible in the semi-displacement regime and by 3% lower when the craft is planing. Furthermore, while in planing regime and in heavy loading conditions the resistance decrease is negligible or the same (about 3%) as in case of chine spray rail, the increase of total resistance at slower speeds and in light loading conditions is considerably smaller (up to 1.3%, compared to 2.9% in case of chine spray rail).

The influence of the chine inclination on the running trim (Fig. 9), unlike that of the chine spray rail, is negligible in the semi-displacement regime. On the other hand, in planing regime, the chine inclination reduces the running trim less than the chine spray rail does. The trim changes are also more or less the same for all loading conditions. That explains the smaller changes in resistance mentioned before.

3.2 *Conventional spray rails*

The total resistance and trim of the SR1 (Fig. 4a) spray rails with rectangular (Rec) and triangular (Tri) profiles (Fig. 5a, b) of seizes 2 × 2 mm and 5 × 5 mm are compared to the bare hull (BH) in Figures 10 and 11 respectively. The total resistance and trim of the hulls equipped with spray rail arrangements SR1 (Fig. 4a) and SR2 (Fig. 4b) with rectangular 2 × 2 mm profiles (Fig. 5a) are compared to those of the bare hull (BH) in Figures 12 and 13 respectively.

3.2.1 *Comparison by spray rail size & shape*

Compared to the bare hull, in light loading conditions, the spray rail with a rectangular 2 × 2 mm profile (SR1-Rec-2 × 2) (Figs. 4a, 5a) increases the total resistance (Fig. 10) by 3.1% – 4.2% in the semi-displacement regime and reduces it by 0.5% – 1.3% in planing mode. When operating in heavy loading conditions, the resistance change is negligible in the semi-displacement regime and by 1.7% lower when the craft is planing.

In light loading conditions, the spray rail with the rectangular 5 × 5 mm profile (SR1-Rec-5 × 5) (Figs. 4a, 5a) increases the total resistance by up to 5.9% in semi-displacement regime while the change of resistance is negligible when the craft is planing. In heavy loading conditions, the total resistance increases by 3.9% – 4.5% in the semi-displacement regime and by 0.5% – 1.2% when the craft is planing.

In light loading conditions, the triangular 2 × 2 mm profile (SR1-Tri-2 × 2) increases the total resistance by 2.5% – 3.2% in the semi-displacement regime and decreases it by 1.0% – 1.8% when the craft is planing. In heavy loading conditions, the spray rail SR1-Tri-2 × 2 reduces the total resistance by 1.1% – 1.8% when the craft is planing while the resistance change is negligible in the semi-displacement regime.

In light loading conditions, the triangular 5 × 5 mm profile (SR1-Tri-5 × 5) increases the total resistance by 4.3% – 4.6% in the semi-displacement regime and decreases it by 0.5% – 0.8%, i.e. the change is negligible when the craft is planing. In heavy loading conditions, the spray rail SR1-Tri-5 × 5 increases the total resistance by 1.8% – 2.8% in the semi-displacement regime and decreases it by 0.1% – 0.3%, i.e. the change is negligible when the craft is planing.

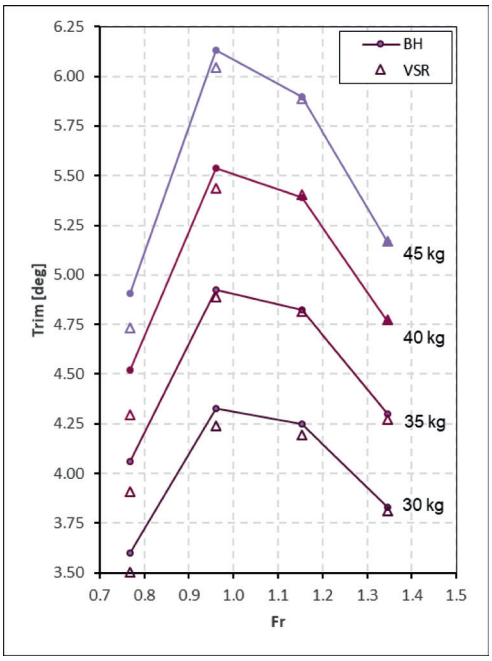

Figure 16. Trim data of the V-shaped spray rail (VSR) compared to the bare hull (BH).

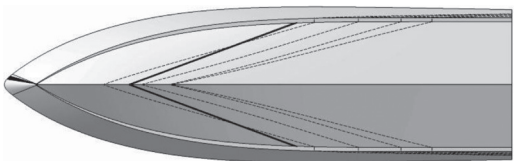

Figure 17. Waterlines of the hull equipped with V-shaped spray rail at tested speeds at 40 kg displacement.

In the discussion above, it is seen that the increase of the size of the deflection surface deteriorates the performance of the craft both in cases with rectangular and triangular profiles. The total resistance increases even more in the semi-displacement regime and its reductions at planing speed are either negated or negligible.

As for the shape of the spray rails, the triangular profiles perform better both in 2 × 2 mm and in 5 × 5 mm size groups. Compared to the bare hull, in the semi-displacement regime, the increase of total resistance is about 1% less for the triangular profile than that of the rectangular profile. In planing regime, the triangular profile yields 0.1% – 0.5% higher decrease of total resistance than the rectangular profile does. However, this difference is probably within the error margin of 0.7% and are therefore inconclusive.

3.2.2 *Comparison by spray rail arrangement*

The total resistance and trim of the hulls equipped with spray rail arrangements SR1 (Fig. 4a) and SR2 (Fig. 4b) with rectangular 2 × 2 mm profiles (Fig. 5a) are compared to those of the bare hull (BH) in Figures 12 and 13 respectively.

Compared to the bare hull, in light loading conditions, the spray rail SR2 with the 2 × 2 mm rectangular profile (SR2-Rec-2 × 2) (Figs. 4b, 5a) increases the total resistance (Fig. 12) by up to 4.3% in the semi-displacement regime and the resistance change is negligible when the craft is planing. However, in heavy loading conditions, this spray rail setup (SR2-Rec-2 × 2) increases the total resistance by up to 2.2% in the semi-displacement regime and reduces it by up to 1.1% when the craft is planing.

Comparing these results to those of short spray rails (SR1-Rec-2 × 2) discussed in the previous section, it is seen that increasing the length of the spray increases the resistance by up to 1.3% in semi-displacement and by 0.8% when the craft is planing. However, since the uncertainty of resistance is around ± 1% in semi-displacement and about ± 0.4% in planing mode, the result presented above are rather inconclusive.

The influence of the spray rail SR1 on the running trim (Fig. 13) is rather small, with few exceptions in the semi-displacement regime. The influence of the spray rail SR2 on the running trim is smaller than that of the spray rail SR1. Since each spray rail extends below the water line (Fig. 14), lengthening the spray rails increases the wetted surface and therefore the viscous resistance. The total resistance of SR2 is likely to be higher than that of SR1 due to the presence of vortices generated and maintained near the extended rails, that otherwise are "smoothed" out by the flow.

3.3 *V-shaped spray rail*

The total resistance and trim of the hulls equipped with V-shaped spray rails (VSR) are compared to those of the bare hull (BH) in Figures 15 and 16 respectively. The waterlines at different speeds are presented for the hull equipped with V-shaped spray rail in design displacement of 40 kg in Figure 17.

At Froude number $Fr > 1$, when the V-shaped spray rail is located above the stagnation line the interceptor starts to deflect the whisker spray as intended, which reduces the resistance by 4% – 5%, with an uncertainty of ± 0.5–0.7%. However, at low speeds when the V-shaped spray rail is below the stagnation line, i.e. submerged, it causes an increase of up to 7.9% in resistance, with an uncertainty of ± 1–2%.

In addition, the resistance increase is dependent on the displacement. The smaller the displacement, the larger the change of total resistance.

The V-shaped spray rail does not seem to affect the running trim in planing regime and reduces it in the semi-displacement regime. Furthermore, the V-shaped rail deflects the whisker spray back and to the side. This, in turn, produces a reaction force on the rail with a considerable x-directional component that propels the craft forward. Since the trim does not change, the reaction force of the V-shaped spray rail seems to be the main cause of the resistance reduction.

Judging by the effect of the V-shaped spray rail in at planing speeds, it is reasonable to assume that one or two additional interceptors would significantly improve the craft's performance in semi-displacement mode and light loading conditions. The considerable differences in the total resistance of the V-shaped spray rail compared to that of the conventional spray rail arrangements are primarily due to the axial component of the reaction force on the rail, which propels the craft forward.

4 CONCLUSIONS

The results of an experimental series comprising 9 spray rail variations and 144 resistance tests are published in this paper. The models were tested in a range of significantly lower speeds (Fr_∇ = 1.86 … 3.05) than in (Clement 1964a, 1964b). Therefore, the influence of the spray rails on the total resistance is also subtler than in the earlier studies. Nonetheless, a few remarkable observations can be made based on the figures of resistance and trim:

1. Chine modifications have a beneficial influence on the performance of the craft, particularly at high speed and in heavy loading condition.
2. A simple rectangular interceptor on the chine reduces the total resistance nearly as much and in some cases more as a more complex chine inclination modification does.
3. Conventional spray rails increase the total resistance of the craft by up to 4% in semi-displacement mode and decrease it by nearly 2% when the craft is planing.
4. Spray rails limited to the vicinity of the dynamic waterline perform in calm water marginally better than those extended to the transom do.
5. In the speed range of Fr = 1.15…1.35, a sharper bottom angle of the spray deflector increases the lift and thereby trim of the craft, which increases the total resistance.
6. If the whisker spray is separated from the hull, increasing the size of the deflection area of spray rails increases the running trim and therefore the total resistance of the craft.
7. When placed above the stagnation line and properly aligned with it, a V-shaped spray rail can reduce the total resistance by up to 4%.

Future studies will address a number of questions regarding this series. Firstly, whether the influence of a chine modification would be the same on a hull equipped with V-shaped or a conventional spray rails set up. Secondly, what are the optimum number and orientation of spray rail for V-shaped arrangement?

ACKNOWLEDGEMENTS

This research work has been financially supported by the Estonian Research Council via grant PRG83 (Numerical simulation of the FSI for the dynamic loads and response of ships). This help is here kindly appreciated.

REFERENCES

Bojovic, Predrag, and Prasanta K. Sahoo. 2000. "Effect of Stern Wedges and Advanced Spray Rail System on Calm Water Resistance of High-Speed Displacement Hull Forms." *Sea Australia 2000.* Sydney.

Bojovic, Predrag, Prasanta K. Sahoo, and Marcos Salas. 2004. "A Study on Stern Wedges and Advanced Spray Rail System on Calm Water Resistance of High-Speed Displacement Hull Forms." Edited by Laurie Prandolini. *Proceedings of Pacific 2004 International Maritime Conference.* Sydney. 170–179.

Clement, Eugene P. 1964. "Effects of Longitudinal Bottom Spray Strips on Planing Boat Resistance, Report No.1818." David Taylor Model Basin, Department of the Navy, Washington, DC.

Clement, Eugene P. 1964. "Reduction of Planing Boat Resistance by Deflection of the Whisker Spray, Report No.1929." David Taylor Model Basin, Department of The Navy, Washington, DC.

Fu, T.C., T. Ratcliffe, T.T. O'Shea, K.A. Brucker, R.S. Graham, D.C. Wyatt, and D.G. Dommermuth. 2010. "A Comparison of Experimental Measurements and Computational Predictions of a Deep-V Planing Hull." *28th Symposium on Naval Hydrodynamics.* Pasadena, California. 17.

Grigoropoulos, Gregory. 1997. "The use of Spray Rails and Wedges in Fast Monohulls." *IV High-Speed Vehicles Intl. Conf. HSMV'97.* Naples, Italy.

Grigoropoulos, Gregory, and Dimitra Damala. 1999. "Effect of spray rails and wedges on the performance of semi—displacement hulls." *V Intl. Conf. on High-Speed Marine Vehicles HSMV'99.* Capri, Italy.

Grigoropoulos, Gregory, and Theodore Loukakis. 1995. "Effect of Spray Rails on the Resistance of Planing Hulls." *3rd Intl. Symposium on Fast Sea Transportation FAST'95.* Travenmuende, Germany.

Kim, Dong Jin, Sun Young Kim, Young Jun You, Key Pyo Rhee, Seong Hwan Kim, and Yeon Gyu Kim. 2013. "Design of high-speed planing hulls for the improvement of resistance and seakeeping performance." *International Journal of Naval Architecture and Ocean Engineering* 5 (1): 161–177.

Müller-Graf, B. 1991. "The effect of an advanced spray rail system on resistance and development of spray of semi-displacement round bilge hulls." Edited by K.O. Holden, O.M. Faltinsen and T. Moan. *FAST'91.* Trondheim, Norway: Tapir Publishers. 125–141.

Olin, Linus, Mireia Altimira, Jonas Danielsson, and Anders Rosén. 2016. "Numerical modelling of spray sheet deflection on planing hulls." *Proceedings of the Institution of Mechanical Engineers, Part M: Journal of Engineering for the Maritime Environment* 231 (4): 811–817.

Savitsky, Daniel. 1964. "Hydrodynamic design of planing hulls." *Marine Technology.* Vol. 1. no. 1. 71–94.

Savitsky, Daniel, and John P. Breslin. 1958. "On the Main Spray Generated by Planing Surfaces." Stevens Institute of Technology, Experimental Towing Tank, Hoboken, New Jersey, 44.

Savitsky, Daniel, and Michael Morabito. 2011. "Origin and Characteristics of the Spray Patterns Generated by Planing Hulls." *Journal of Ship Production & Design* 27 (2): 63–83.

Savitsky, Daniel, Michael F DeLorme, and Raju Datla. 2007. "Inclusion of Whisker Spray Drag in Performance Prediction Method for High-Speed Planing Hulls." *Marine Technology* 44 (1): 35–56.

Seo, Jeonghwa, Hak Kyu Choi, Uh Cheul Jeong, Dong Kun Lee, Shin Hyung Rhee, Chul Min Jung, and Jaehoon Yoo. 2016. "Model tests on resistance and seakeeping performance of wave-piercing high-speed vessel with spray rails." *International Journal of Naval Architecture and Ocean Engineering* 8 (5): 442–455.

Appendix 2

Publication P2

Lakatoš, M., Sahk, T., Andreasson, H., & Tabri, K. (2022). The effect of spray rails, chine strips and V-shaped spray interceptors on the performance of low planing high-speed craft in calm water. *Applied Ocean Research*, *122*(February), 103131. https://doi.org/10.1016/j.apor.2022.103131

Applied Ocean Research 122 (2022) 103131

Contents lists available at ScienceDirect

Applied Ocean Research

journal homepage: www.elsevier.com/locate/apor

The effect of spray rails, chine strips and V-shaped spray interceptors on the performance of low planing high-speed craft in calm water

Mikloš Lakatoš [a,*], Tarmo Sahk [a], Henrik Andreasson [b], Kristjan Tabri [a]

[a] Tallinn University of Technology, Tallinna 19, Kuressaare 93811, Estonia
[b] Flow Naval Architects AB, Sweden

ARTICLE INFO

Keywords:
Planing craft
Model test
Spray rail
Chine strip
V-shaped spray interceptor

ABSTRACT

The design of spray rails has been under-reported in recent decades; besides general guidelines, few studies focus on the design of spray rails on a planing craft. The influence of the breadth and the bottom angle of the spray rails on the performance of the craft is not clear yet. Although known to naval architects, few studies of chine strips have been conducted. V-shaped spray interceptors (VSI) are a novel concept of reducing the resistance of a planing craft by deflecting the spray forward of the stagnation line. Although the VSIs have been shown to reduce the resistance of a planing craft at $Fr_\nabla > 3.65$, it is not known whether they yield the same benefits at lower planing speeds. This study presents a series of model tests of a low planing craft ($Fr_\nabla = 1.742$–3.261) equipped with different spray rails, chine strips, and a V-shaped spray interceptor (VSI). At planing speeds $Fr_\nabla > 3$, the spray rails reduced the resistance by up to 2.4%, while at semi-displacement speeds $Fr_\nabla < 3$, spray rails did not improve the performance. At $Fr_\nabla > 3$, none of the spray rails changed the trim ($\pm$ 0.05°) significantly. Narrow spray rails with sharp bottom angles provided equal or better performance compared with conventional wide horizontal spray rails. Unnecessarily long spray rails increase the resistance, negating the benefits of spray deflection. Chine strips had a significant influence on the total resistance, trim and sinkage of both the bare hull and the hull equipped with spray rails. At the planing speed, chine strips reduced the running trim by up to 0.3° and the total resistance by up to 3%. However, at semi-displacement speeds, the effect of the chine strips was proportionally opposite. When the VSI was located forward of the stagnation line, it deflected the oncoming spray, thereby inducing a reaction force on its deflection surface in the direction of the craft's motion, hence reducing the total resistance by up to 4.2%. When the VSI was behind the stagnation line, it increased the total resistance by up to 8.4%.

1. Introduction

Spray is a phenomenon that occurs on high-speed marine vehicles, including semi-displacement craft, planing craft and hydroplanes. It is formed at the stagnation line (Fig. 1), "a locus of points on the bottom along which the flow is divided into forward and aft components and on which the pressure is a maximum and is developed from bringing to rest the component of free stream velocity normal to this line" (Savitsky and Morabito, 2011). Hence, the area of the wetted bottom aftward of the stagnation line is referred to as the pressure area while the wetted bottom forward of the stagnation line is referred to as the spray area. The direction of the fluid in the spray area is such that the streamlines are nearly a reflection of the free stream about the stagnation line (Savitsky and Morabito, 2011). As spray flows from the stagnation line across the bottom line towards the chine, it causes viscous force with an aft component that adds to the total resistance of the craft.

While observed and acknowledged in the original Savitsky method (Savitsky, 1964), whisker spray was not accounted for until an analytical model (Savitsky et al., 2007) was added to the method. The model showed that depending on the speed and the geometry of the craft, whisker spray accounted for 10-15% of total resistance. A more recent experimental study (Begovic and Bertorello, 2012) assessed the wetted surface (pressure and spray area) of hard chine planing hull forms with transparent bottoms at $Fr_\nabla = 0.650$–4.518. Based on the photographs of the transparent hull bottoms, consequent post-processing of the 3D models of the hulls, and on Savitsky's resistance breakdown procedure (Savitsky et al., 2007), the spray resistance was reported to account for up to 10% of the total resistance.

Spray resistance is usually reduced by installing on the bottom of the

* Corresponding author.
E-mail address: miklos.lakatos@taltech.ee (M. Lakatoš).

https://doi.org/10.1016/j.apor.2022.103131
Received 17 October 2021; Received in revised form 26 February 2022; Accepted 7 March 2022
Available online 23 March 2022
0141-1187/© 2022 The Authors. Published by Elsevier Ltd. This is an open access article under the CC BY license (http://creativecommons.org/licenses/by/4.0/).

Abbreviations

b	wetted half-width (m)
b_1	actual wetted half-width (m)
b_{SR}	width of the spray rail (m)
b_{CS}	width of the chine strip (m)
B_{CT}	chine beam at the transom (m)
B_{OA}	beam overall (m)
B_{WL}	beam waterline (m)
CG	centre of gravity
C_V	Froude number based on breadth B_{CT} (1)
d	parallel normal distance from stagnation line to VSI (m)
Fr	Froude number (1)
Fr_∇	Froude displacement number (1)
KG	vertical centre of gravity (m)
k_p	coverage factor for probability p (1)
l_w	wetted length up to the spray root line (m)
L_{CG}	longitudinal position of the centre of gravity from transom (m)
L_{OA}	length overall (m)
L_{pp}	length between perpendiculars (m)
L_{WL}	length waterline (m)
R_{TM}	total resistance in model scale (N)
T	draught (m)
u_c	combined standard uncertainty (1)
U_p	expanded uncertainty associated with confidence level p (1)
$z_{VCG}/\nabla^{1/3}$	non-dimensional dynamic sinkage at CG (1)
α	stagnation angle (deg)
β_T	deadrise angle at the transom (deg)
$\beta_{0.5}$	deadrise angle at 50% L_{DWL} (deg)
$\beta_{0.75}$	deadrise angle at 75% L_{DWL} (deg)
δ	bottom angle of the spray rail (deg), thickness of the spray sheet (m)
Δ	displacement force (N)
Δ_m	displacement mass (kg)
τ	dynamic trim (deg)
$\delta\tau$	change in dynamic trim compared to the benchmark (deg)
δR_{TM}	change in total resistance compared to the benchmark (%)
$\delta z_{VCG}/\nabla^{1/3}$	change in non-dimensional dynamic sinkage at CG compared to the benchmark (1)
∇	displacement volume (m3)
Ⓜ	length-displacement ratio $L_{WL}/\nabla^{1/3}$ (1)
BH	bare hull
CINC	chine inclination
Con	conventional spray rail profile
CSR	chine spray rail
CSI	chine spray interceptor
Rec	rectangular spray rail profile
SR1	spray rail arrangement 1
SR2	spray rail arrangement 2
Tri	triangular spray rail profile
VSI	V-shaped spray interceptor

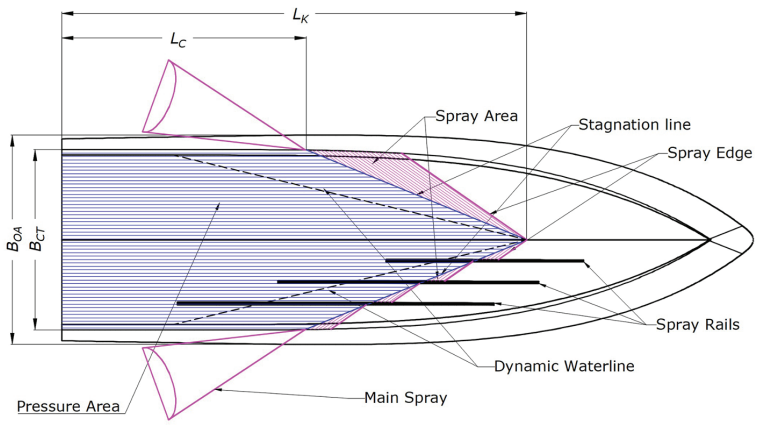

Fig. 1. Comparison of spray formation on a planing hull with and without spray rails.

craft two to four longitudinal spray rails that detach the spray from the hull and deflect it towards the sides or down and aftward (Fig. 1). Spray rails are usually aligned vertically, i.e. they follow the buttocks of the hull. They may also follow the waterlines or the diagonals or be extended up to the bow stem. Spray rails have been shown to reduce total resistance by 6–25% when Froude displacement number $Fr_\nabla > 3.5$ (Clement, 1964a, 1964b; Grigoropoulos and Loukakis, 1995). However, at displacement and semi-displacement speeds ($Fr_\nabla < 2.3$), the spray rails may increase the resistance by up to 3% (Clement, 1964a). This raises the question of whether the spray rails need to be installed on the semi- and low-planing craft that operate at $Fr_\nabla < 3.3$ at all. By excluding spray rails, it would be possible to lower labour costs and to reduce noise when the craft is planing. Furthermore, besides the general guidelines (see Section 2.2), there are few studies on the design of spray rails on planing hulls. The influence of the breadth and the bottom angle of the spray rails on the performance of the craft is still unclear.

Experimental data on the concept of deflecting the main spray is even more scarce than that on spray rails. An experimental study (Kapryan and Boyd, 1953) compared the effect of vertical chine strips (Fig. 2e,f) on the planing characteristics of two prismatic V-shaped hulls (Chambliss and Boyd, 1953) ($\beta = 20°$ & $\beta = 40°$) (Fig. 2a,b) with those of horizontal chine flares (Fig. 2c,d) (Kapryan and Weinstein, 1952; Blanchard, 1952). The hulls were tested in captive conditions, i.e. at a fixed running position. The study concluded that the vertical chine strips increase the lift of a V-shaped hull significantly more than horizontal chine flares do. When combined with horizontal chine flares, chine

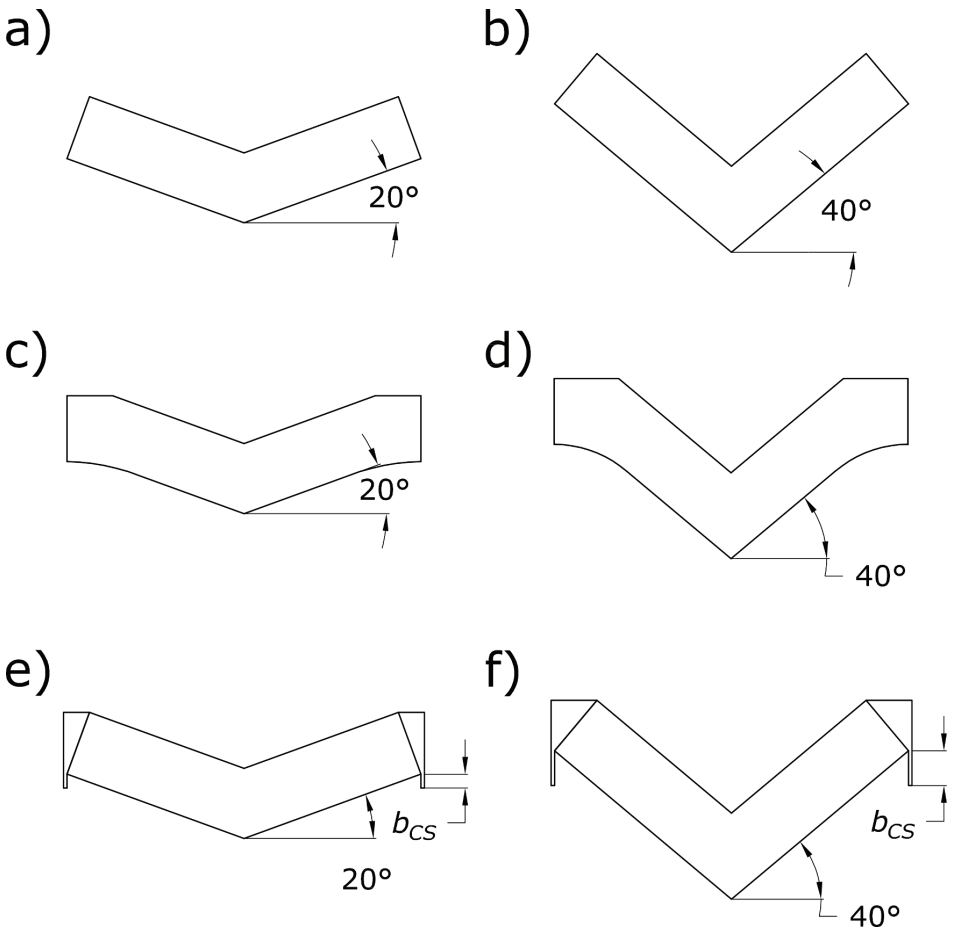

Fig. 2. (a) prismatic V-shape hull $\beta = 20°$ (Chambliss and Boyd, 1953), (b) prismatic V-shape hull $\beta = 40°$ (Chambliss and Boyd, 1953), (c) prismatic V-shape hull with horizontal chine flares $\beta = 20°$ (Kapryan and Weinstein, 1952), (d) prismatic V-shape hull with horizontal chine flares $\beta = 40°$[11], (e) prismatic V-shape hull with chine strips $\beta = 20°$ (Kapryan and Boyd, 1953), (f) prismatic V-shape hull with chine strips $\beta = 40°$ (Kapryan and Boyd, 1953).

Table 1
Main dimensions of the bare hull in the design condition.

Parameter		Model scale	Full scale
Scale factor	λ	10	1
Length overall	L_{OA}	1.921 m	19.210 m
Length between perpendiculars	L_{pp}	1.800 m	1.800 m
Length waterline	L_{DWL}	1.703 m	17.030 m
Beam overall	B_{OA}	0.581 m	5.810 m
Chine beam at the transom	B_{CT}	0.500 m	5.000m
Draught	T_{DWL}	0.108 m	1.080 m
Vertical centre of gravity	KG	0.200 m	2.000 m
Longitudinal position of the centre of gravity from the transom	L_{CG}	0.670 m	6.700 m
Deadrise angle at the transom	β_T	19.92 deg	19.92 deg
Deadrise angle at 50% L_{DWL}	$\beta_{0.5}$	22.78 deg	22.78 deg
Deadrise angle at 75% L_{DWL}	$\beta_{0.75}$	33.39 deg	33.39 deg

strips work similar to interceptors, i.e. they deflect the spray at a right angle and increase the lift at the intersection of the chine with the stagnation line. This in turn shifts the center of pressure aft-wards and reduces the trim. Although known to naval architects, no studies have addressed chine strips combined with horizontal chine flares. The extent of reduction in the trim by the chine strips and their performance in comparison with that of the stern interceptors are still unknown (De Luca and Pensa, 2012; Karimi et al., 2013; Mansoori and Fernandes, 2017; Avci and Barlas, 2019; Park et al., 2019; Seok et al., 2020; Mansoori et al., 2017).

V-shaped spray interceptors (VSIs), also known as spray deflectors (Olin et al., 2016; Molchanov et al., 2019; Castaldi et al., 2021), are a novel concept of spray deflection wherein the kinetic energy of the spray is utilized to reduce the resistance of a planing craft. The VSIs (Fig. 5a) are placed forward of the stagnation line, in parallel, such that they deflect the oncoming spray, thereby producing a forward reaction force that reduces the total resistance of the craft. The initial designs (Olin et al., 2016; Molchanov et al., 2019) of the VSI were essentially a further iteration of the stepped hull concept. Unlike previous models, where the step was either perpendicular to the keel (Taunton et al., 2010; Cucinotta et al., 2019), or the step had a forward sweep (De Marco et al.,

Table 2
Dimensions of the tested spray rails and chine strips.

V_M [m/s]	C_V	Ⓜ	Hull configuration	b_{SR}[mm]	b_{SR}/L_{DWL}	δ [deg]	b_{CS} [mm]	b_{CS}/L_{DWL}	δ_{CS} [deg]	β'[deg]
			BH							
			SR1-Con-3×8	7	0.5%	0				
			SR1-Rec-2×2	2	0.1%	-70				
			SR1-Rec-5×5	5	0.3%	-70				
3.254	1.469	5.411	SR1-Tri-2×2	2	0.1%	-25				
4.067	1.837	5.174	SR1-Tri-5×5	5	0.3%	-25				
4.880	2.204	4.978	SR2-Rec-2×2	2	0.1%	-70				
5.694	2.571	4.812	SR2-Rec-5×5	5	0.3%	-70				
			VSI-Tri–5×5	5	0.3%	-66				
			BH-C.INC				15	0.9%	-8	18.4
			BH-CSI 1				2	0.1%	-90	18.4
			BH-CSI 2				5	0.3%	-90	17.8
			BH-CSR 1				3	0.1%	-45	18.4
			BH-CSR 2				7	0.4%	-45	17.8
			SR1-Rec-5×5-CSI1	5	0.3%	-70	2	0.1%	-90	18.4
			SR1-Rec-5×5-CSR2	5	0.3%	-70	7	0.4%	-45	17.8

Table 3
Hydrostatic characteristics and speed ranges of the craft in tested loading conditions.

L_{WL} [m]	B_{WL} [m]	T [m]	Δ_m [kg]	∇ [m^3]	L_{CG} [m]	Ⓜ	L_{WL}/B_{WL}	B_{WL}/T	L_{CG}/L_{WL}	V_{CG}/B_{WL}	Fr	Fr_∇
1.682	0.503	0.093	30	0.030	0.663	5.411	3.341	5.425	0.394	0.397	0.801–1.402	1.864–3.261
1.693	0.507	0.099	35	0.035	0.666	5.174	3.341	5.120	0.393	0.395	0.798–1.397	1.816–3.178
1.703	0.510	0.108	40	0.040	0.670	4.978	3.338	4.737	0.393	0.392	0.796–1.393	1.776–3.108
1.712	0.513	0.115	45	0.045	0.674	4.812	3.336	4.470	0.394	0.390	0.794–1.390	1.742–3.048

2017), or there were two swept steps (Bilandi et al., 2019,2020), in the case of a VSI, the step was swept backwards and placed forward of the stagnation line. However, in more recent studies (Castaldi et al., 2021; Wielgosz et al., 2018; Lakatoš et al., 2020), the VSIs are attached to the hull similar to conventional spray rails (Fig. 5b,c).

In the numerical study by Olin et al. (2016), the VSI was found to reduce the total resistance by up to 30% compared to the bare hull at $Fr_\nabla = 6.24$. It was also shown that the reaction force due to the deflection of the spray is comparatively small, 4% of R_{TM} at $Fr_\nabla = 6.24$, while the rest of the reduction in resistance was due to a smaller spray area. The experimental study by Molchanov et al. (2019) compared two VSI arrangements (designed for $Fr_\nabla = 4.3$ and $Fr_\nabla = 5.87$) with conventional spray rails at $Fr_\nabla = 3.5$–6.65 in calm water and irregular waves. The study reported that while the conventional spray rail setup reduced the total resistance by up to 9%, the two VSI configurations reduced it by 14.5–25%. However, since the location of the VSI was determined using the Savitsky method that does not predict accurately the running position and the location of the stagnation line, the VSI increased the trim significantly (Molchanov et al., 2019; Castaldi et al., 2021).

The experimental study by Castaldi et al. (2021) addressed the effect of three spray VSI arrangements (designed for $Fr_\nabla = 3.65$, $Fr_\nabla = 4.56$ and $Fr_\nabla = 5.48$) across a range of planing speeds from $Fr_\nabla = 2.97$–5.93 (Castaldi et al., 2021). Since the location of the VSI was determined based on the underwater photos of the bare hull test, the change in the running position was negligible. The study reported that the VSI reduced the resistance by 1.5 and 2.5% at their design speeds, with peaks of up to 5% at lower speeds. This was due to a ventilation effect that originated at the intersection of the stagnation line and the VSI. The study also reported that the key factor in the efficiency of spray deflection was the distance between the stagnation line and the VSI, and increasing this distance proved beneficial. As previous studies focused on the VSI designed for speeds $Fr_\nabla \geq 3.65$, it is not known whether a VSI arrangement designed for $Fr_\nabla < 3.65$ would also yield similar reductions in total resistance.

This study aims to deepen the understanding of the various design parameters of spray rails, chine strips and VSI to find an optimum solution for a low-planing craft. Hence, this study has three objectives – firstly, to experimentally investigate the influence of the width, bottom angle and length of spray rail on the total resistance and running position of a craft operating at $Fr_\nabla < 3.3$ and to compare the results with the existing guidelines. Secondly, to examine the effect of chine strips on the resistance and running position of the craft and whether those can compensate for the negative effect of spray rails. Finally, to investigate the influence of the VSI on the resistance and running position of the craft at $Fr_\nabla < 3.3$.

2. Experimental tests

2.1. Test case

The object of this study was a planing craft with its main particulars (Table 1) common for a high-speed patrol, pilot, search and rescue (SAR) craft or for a planing yacht. The craft was designed to operate at a service speed of $Fr_\nabla = 3.108$ and at a maximum speed above $Fr_\nabla = 3.553$, equivalent to a displacement of 40 t, service speed of 35 knots and a top speed above 40 knots in full scale ($\lambda = 10$). The test series comprised 15 configurations (Table 2): seven conventional spray rail configurations, a V-shaped spray interceptor (VSI) arrangement and seven chine strips. Each configuration was tested at four speeds and four loading conditions (Table 3). The geometries of the tested spray rails, chine strips and the VSI are described in more detail in Sections 2.2–2.5.

The calm water towing tests were conducted in the towing tank of SCC (see Table A.1) following the ITTC guidelines (28th ITTC, 2017). The models were tested in semi-captive conditions (Fig. A.1), i.e. the models were free to pitch and heave. During the tests, total resistance R_{TM} and running sinkage at the aft and fore perpendiculars z_{VF} and z_{VA} were measured at a sampling frequency of 200 Hz. The running trim angle τ of the craft was derived from the readings of running sinkage at the aft (z_{VA}) and the bow (z_{VF}) perpendicular. The sinkages at the aft and fore perpendicular were used to generate the running waterline using a 3D model of the craft. This allowed measuring the wetted keel length L_K and the distance from the transom to the intersection of the chine and the undisturbed water surface (wetted chine length at the waterline). The uncertainty analysis was carried out following the ITTC guidelines (27th ITTC, 2014a, 2014b). The laboratory instrumentation and

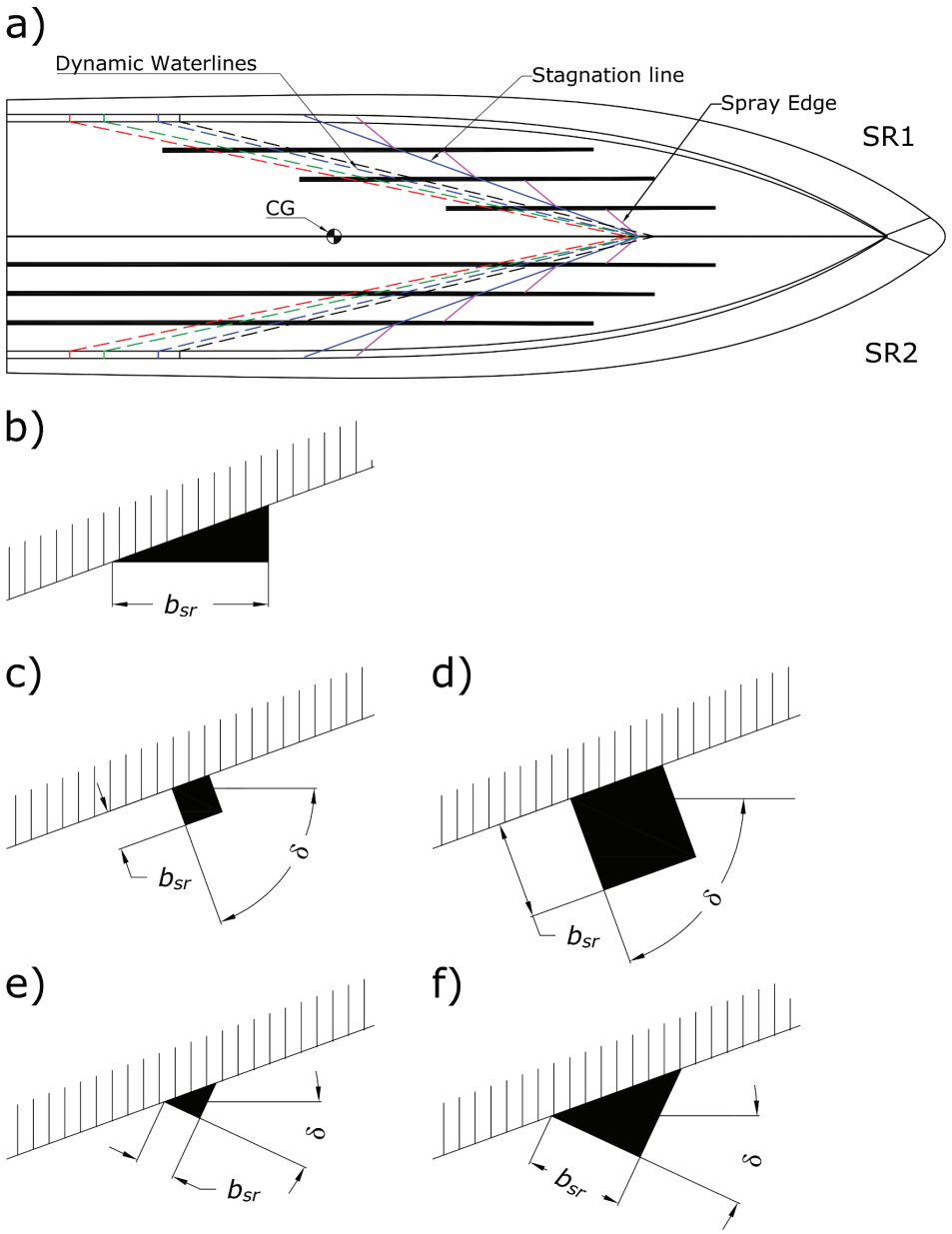

Fig. 3. Tested spray rail configurations: (a) limited spray rails (SR1) and spray rails extending to the transom (SR2), (b) conventional (Con-3×8), (c) rectangular (Rec-2×2), (d) rectangular (Rec-5×5), (e) triangular (Tri-2×2), (f) triangular (Tri-5×5).

uncertainty analysis are reported in more detail in Appendix A.

2.2. General guidelines for spray rail design

Although there are no precise procedures for designing spray rails, a few general guidelines have been provided in literature. First, since the deflection of the spray induces a lifting force that affects the running trim of the craft, spray rails should not produce too much lift in the forebody. This would shift the center of effort forward and, consequently, would increase the trim, which in turn would increase the resistance. Furthermore, if a large lift is produced when the forebody hits the waves, larger accelerations will occur reducing the seakeeping properties of the V-shape hull. Therefore, the spray rail should be small in the forebody and their deflection surface should be inclined upwards rather than downwards (Larsson et al., 2014). Although there is no accurate procedure developed for the extra lift generated by the spray rails, it can be roughly accounted for by measuring the deadrise angle from the keel to the outer edge of the active spray rail. This angle is

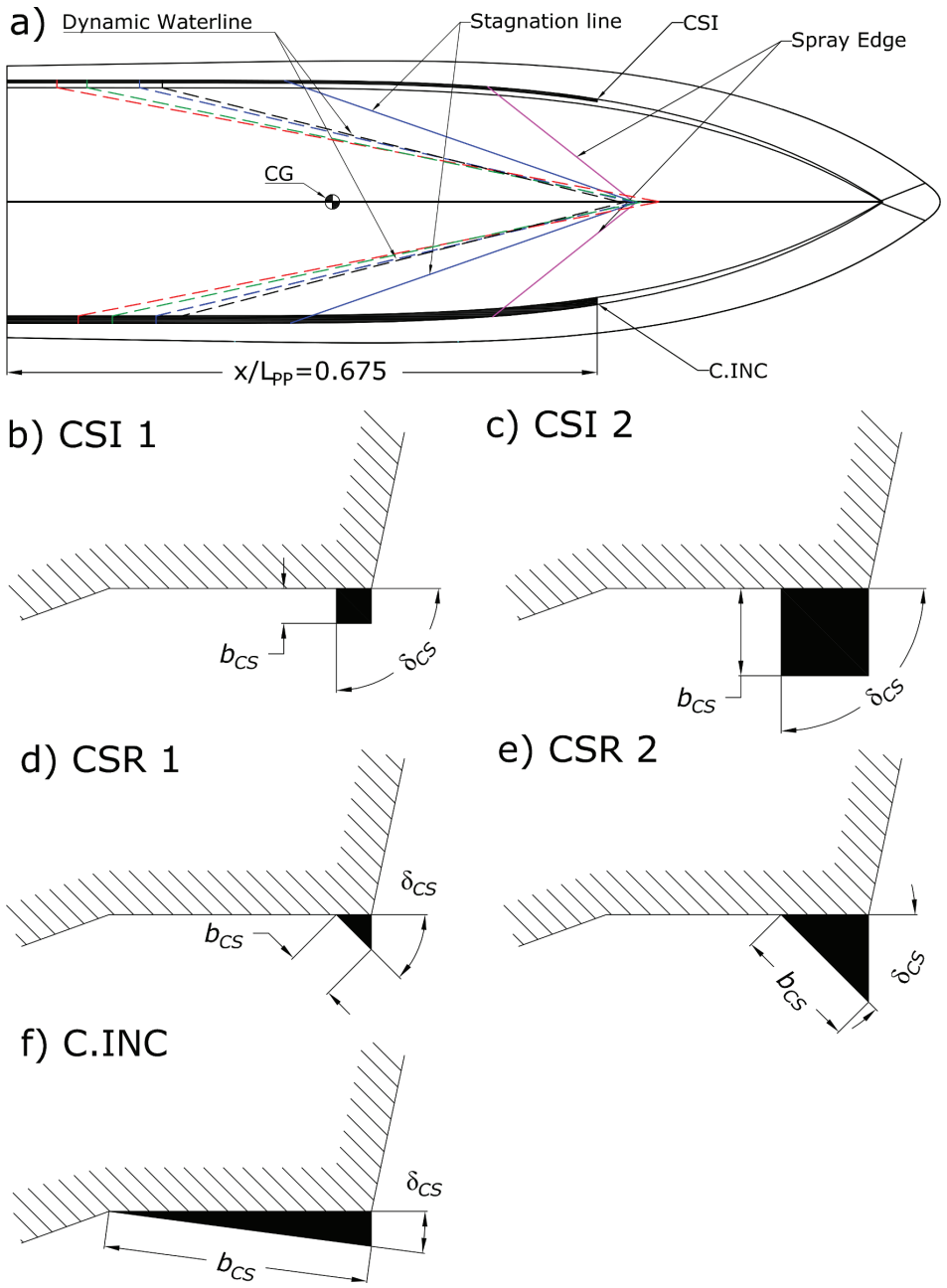

Fig. 4. Tested chine strips: (a) Position of the chine strips, (b) CSI1, (c) CSI2, (d) CSR1, (e) CSR2, (f) C.INC.

smaller than the one measured along the bottom of the hull and thus yields a higher lift (Larsson et al., 2014).

Second, since aftward of the stagnation line the flow is mostly parallel with the keel, the spray rails should be limited by the stagnation line and the spray edge line (Clement, 1964a). However, if the craft is intended to operate at high speeds, at the point where the stagnation line reaches the transom, the outer spray rail can be extended to the transom to prevent chine walking (Larsson et al., 2014).

Third, the spray rail should be as sharp as possible at the outer edge where the water leaves the hull and it should be smoothly blended into the hull to reduce resistance (Larsson et al., 2014). The sharpness of the outer edge of the spray rail is particularly important since its rounding may cause the spray sheet to remain attached to the deflection surface, thus significantly reducing its ability to deflect the spray sheet (Savitsky et al., 2007). A rounded outer edge of the spray rail (ca. 6 mm radius, full scale) nearly negated the effectiveness of the spray rails compared to

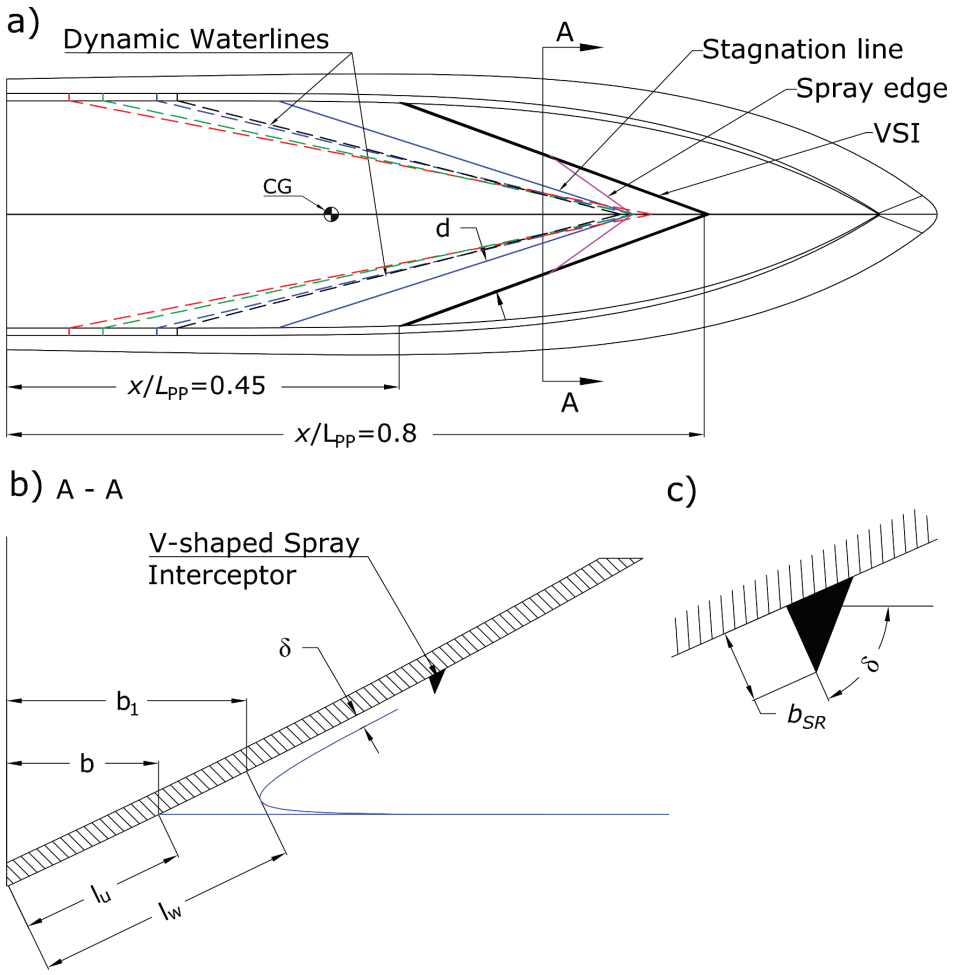

Fig. 5. V-shaped spray interceptors: (a) layout, (b) cross-section of the hull and dimensions of the spray sheet at $x/L_{WL} = 0.65$, c) profile of the VSI at $x/L_{WL} = 0.65$.

Table 4
Estimation of spray sheet thickness.

x [mm]	x/L_{WL}	β_x [deg]	b [m]	b_1 [m]	l_w	δ/l_w	δ [m]
852	0.500	22.700	0.106	0.17	0.180	0.028	0.0050
1022	0.600	24.900	0.065	0.10	0.113	0.034	0.0039
1064	0.625	25.600	0.055	0.09	0.096	0.037	0.0035
1107	0.650	26.400	0.044	0.07	0.077	0.039	0.0030
1192	0.700	28.300	0.024	0.04	0.043	0.046	0.0020
1277	0.750	30.600	0.004	0.01	0.007	0.056	0.0004

those with a smaller rounding (ca. 3 mm radius, full scale) (Savitsky et al., 2007).

Although the spray rails have a significant impact on the performance of high-speed marine vehicles, to date, the study by Müller-Graf (1991) is the only systematic investigation of the size, shape and location of spray rails. The resulting optimum spray rail was found to have a break-off angle of the spray rail $\zeta > 90$ deg, a bottom angle of the spray rail $\delta = 8$ deg and the width of the spray rail $b_{SR} = 0.0055\, L_{WL}$. However, in this study, the author optimized spray rails for a semi-displacement vessel ($Fr = 0.3$–1.0), where spray deflection phenomena are different from those of the planing craft.

2.3. Spray rails

The conventional spray rails had two different layouts: SR1 with the spray rails limited by the dynamic waterline and SR2 with the spray rails extended up to the transom (Fig. 3a). The dashed lines in black, blue, green and red represent the dynamic waterlines of the craft at the top speed of $C_V = 2.571$ and length-displacement ratios of Ⓜ = 4.812, 4.978, 5.174, 5.411 ($Fr_\nabla = 3.048, 3.108, 3.178, 3.261$) respectively. The spray rails were aligned vertically, i.e. they followed the buttocks of the hull. Spray rails may also follow the waterlines or the diagonals, or extend to the bow stem. However, the spray rails extended to the bow stem remain dry at planing speeds and in calm water. Since the objective of this study was to investigate different spray rails at planing speeds in calm water, the authors selected the simpler vertical alignment.

The conventional profile (Fig. 3b) had a horizontal deflection surface, i.e. its bottom angle $\delta = 0°$. Due to the hull curvature (hull warp, increasing deadrise angle), the width of the deflection surface of the conventional spray rail Con-3×8 varied from $b_{SR} = 8$ mm in the aft to $b_{SR} = 5$ mm in the forebody. To examine the effect of increasing the

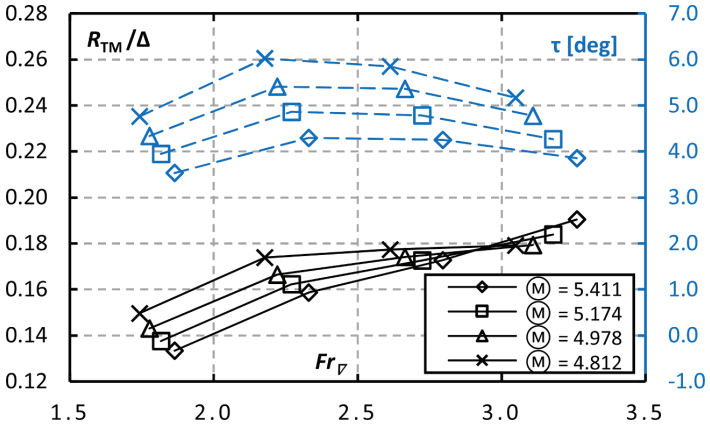

Fig. 6. Resistance and trim of the bare hull.

Table 5
Uncertainties of parameters measured through the test campaign.

	U_p' (R_{TM}/Δ)	U_p ($z_{VCG}/\nabla^{1/3}$)	U_p (τ) [deg]
Min	0.2%	0.001	0.027
Max	1.7%	0.004	0.085
Average	0.4%	0.002	0.035
Median	0.4%	0.001	0.032

width b_{SR} and the bottom angle δ of the spray rails independently, the spray rails were modeled with a rectangular (Fig. 3c,d) and a triangular profiles (Fig. 3e,f). The width of the spray rails was increased from b_{SR} = 2 mm to b_{SR} = 5 mm, replacing a 2 × 2 mm profile with a 5 × 5 mm profile. The bottom angle of the spray rail was reduced from $\delta = -25°$ to $\delta = -70°$, replacing the triangular profile with a rectangular one.

The choice of the spray rail profiles was governed by the ease of manufacturing. While the conventional spray rails had to be 3D printed, the square and triangular profiles were readily available in sizes 2 × 2 mm & 5 × 5 mm. Furthermore, rectangular and triangular profiles provided a constant width of the spray rails b_{SR}. The width of the tested spray rails b_{SR} = 0.1–0.3% L_{WL} is well within the recommendation b_{SR} = 0.5% L_{WL} proposed by Müller-Graf (1991).

2.4. Chine strips

The series includes two sets of hulls with modified chines: the bare hull (BH) and the hull equipped with the rectangular 5 × 5 mm spray rails limited by the dynamic waterline (SR1-Rec-5×5). First, the bare hull was tested with an inclined chine (C.INC), i.e. the rails covered the whole chine (b_{CS} = 15 mm), resulting in a new chine surface angled down by $\delta_{CS} = -8°$ (Fig. 4a,f). Then, the bare hull was tested with rectangular and triangular chine strips attached along the outer edge of the chine. Both rectangular and triangular chine strip profiles had two sizes: 2 × 2 mm and 5 × 5 mm.

Since the rectangular chine strips (Fig. 4b,c) deflected the spray at a right angle, they are referred to as chine spray interceptors designated as CSI1 and CSI2. The triangular chine strips (Fig. 4d,e) deflected the spray at an angle of 45°, hence they are referred to as chine spray rails designated as CSR1 and CSR2. The hull equipped with spray rails (SR1-Rec-5×5, Fig. 3a,d) was tested with rectangular 2 × 2 mm chine spray interceptors CSI1 (Fig. 4b) and with triangular 5 × 5 mm chine spray rails CSR2 (Fig. 4e). The widths b_{CS} and bottom angles δ_{CS} of the tested chine strips as well as the deadrise angles measured from the keel to the outer edge of the chine strips β' are reported in Table 3. The dashed lines in black, blue, green and red represent the dynamic waterlines of the craft at the top speed of C_V = 2.571 and length-displacement ratios of Ⓜ = 4.812, 4.978, 5.174, 5.411 (Fr_∇ = 3.048, 3.108, 3.178, 3.261), respectively.

2.5. V-shaped spray interceptors

The V-shaped spray interceptors (VSI) (Fig. 5a) were designed for Ⓜ = 4.978, Fr = 1.393 and Fr_∇ = 3.108, equivalent to the craft's design displacement of Δ_{mS} = 40 t and speed of V_S = 35 knots in full-scale. The dashed lines in black, blue, green and red represent the dynamic waterlines of the craft at the top speed of C_V = 2.571 and length-displacement ratios of Ⓜ = 4.812, 4.978, 5.174, 5.411 (Fr_∇ = 3.048, 3.108, 3.178, 3.261), respectively.

The position of the VSI was designed based on the dynamic waterlines of the bare hull, so that the VSI would be slightly forward of the stagnation line. To ensure that the VSI was high enough, the spray sheet thickness δ was estimated using equations proposed by Wagner (1932), which have been shown to correlate well with numerical calculations (Olin et al., 2016).

Following Wagner's approach (Wagner, 1932), the actual wetted half-width b_1 is $\pi/2$ times the wetted half-width b defined by the calm water intersection with the bottom, i.e. the dynamic waterline (Fig. 5b). The wetted length up to the spray root line $l_w = \frac{b_1}{\cos\beta}$ is calculated by dividing the wetted half-width by the cosine of the deadrise angle β. The ratio of the spray sheet thickness to the wetted length is calculated using equation $\frac{\delta}{l_w} = \frac{\tan^2\beta}{2\pi}$.

The resulting estimates of spray sheet thickness along the stagnation line are shown in Table 4. The spray sheet thickness was estimated to vary in a range of δ = 1–5 mm. Hence, the VSIs were modeled with triangular 5 × 5 mm profiles (Fig. 5c) with their deflection surfaces perpendicular to the hull. The 5 × 5 mm profile was used to ensure that the height of the interceptor b_{SR} = 5 mm was sufficient to deflect all of the spray in a direction normal to the hull.

3. Results and discussion

The hulls equipped either with spray rail, chine strips or the VSI were compared to the bare hull in terms of nondimensional total resistance R_{TM}/Δ, running trim τ and nondimensional sinkage at the centre of gravity $z_{VCG}/\nabla^{1/3}$ (Tables B.1–B.4). The values of resistance and trim of the bare hull are shown in Fig. 6.

One of the most important hydrodynamic characteristics of a planing craft is its running trim as it directly influences the total resistance and determines the location of the stagnation line. The running trim is

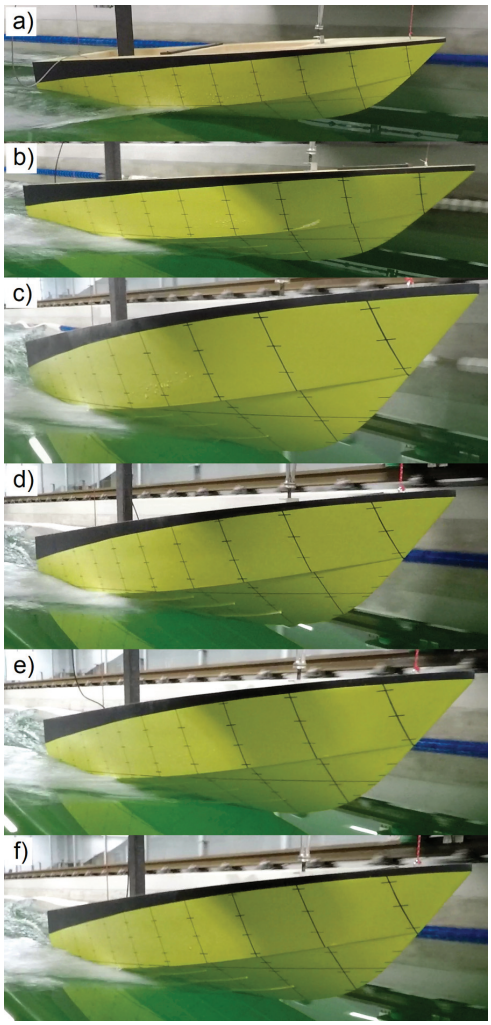

Fig. 7. Spray formation of the model planing at the design speed and displacement ($Fr_\nabla = 3.108$, Ⓜ = 4.978): (a) BH, (b) SR1-Con-3×8, (c) SR1-Rec-2×2 (d) Sr1-Rec-5×5, (e) SR1-Tri-2×2, (f) SR1-Tri-5×5.

determined by the equilibrium of the moments of the drag, lift and propulsive force (Savitsky, 1964). Similar to the angle attack of a foil, a higher trim will increase lift and drag.

Since the model was only free to pitch and heave, the only dynamic instability that could have occurred would have been dynamic pitch-heave oscillation, i.e. porpoising. However, no porpoising was detected through the whole experimental campaign. The median uncertainty of resistance, sinkage and trim was 0.4%, 1.5% and 0.7%, respectively Table 5. gives an overview of the uncertainty of measured items through the test campaign.

3.1. Spray rails

Fig. 7. compares the formation of spray on the tested spray rail configurations in the design condition ($Fr_\nabla = 3.108$, Ⓜ = 4.978) Fig. 8.. displays the spray formation on the model SR1-Rec-2×2 at Ⓜ = 4.978 and $Fr_\nabla = 1.776, 2.220, 2.664, 3.108$. The figure shows that the spray is

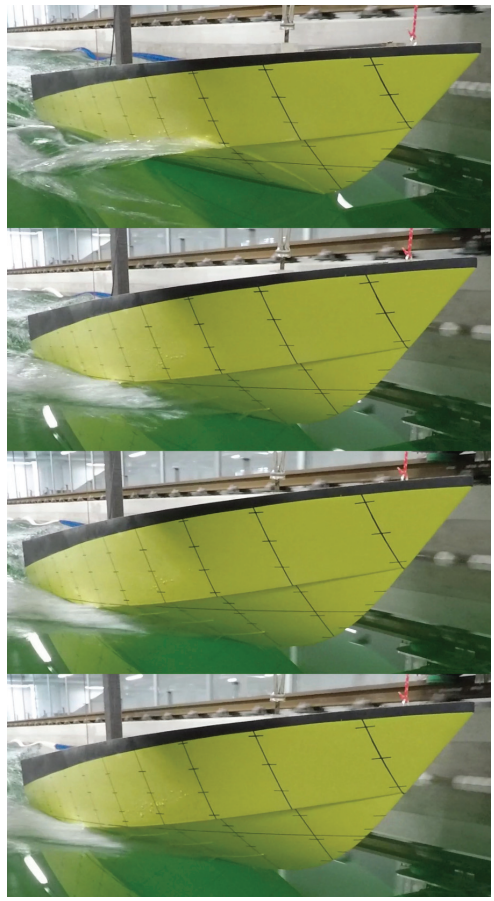

Fig. 8. Spray formation on the model SR1-Rec-2×2 at Ⓜ = 4.978 and $Fr_\nabla = 1.776, 2.220, 2.664, 3.108$.

deflected at all speeds except $Fr_\nabla = 1.776$ when the spray rails are covered with spray. The same behaviour of the spray rails was observed at higher and lower length-displacement ratios.

Fig. 9 compares the tested spray rail arrangements with the bare hull in terms of change in total resistance δR_{TM}, dynamic trim $\delta\tau$ and sinkage at the centre of gravity $\delta z_{VCG}/\nabla^{1/3}$. It shows that the spray rails reduced the total resistance by up to 2.4% at $Fr_\nabla > 3$. Furthermore, it can be seen that the spray rails reduced the total resistance only at high length-displacement ratios Ⓜ ≥ 5.174 and at planing speeds $Fr_\nabla \geq 3$. At $Fr_\nabla < 2.5$; the spray rails increased the total resistance by up to 8.3%. At $2.5 > Fr_\nabla < 3$, the spray rails increased the resistance by up to 2%, or their effect was within the uncertainty margin of 0.4%, hence negligible. In most cases, the increase in resistance resulted from an increase in the running trim.

Compared to the bare hull, the conventional spray rails (b_{SR} = 6–8 mm, $\delta = 0°$) decreased the resistance only by up to 1.3% at $Fr_\nabla > 3$ and high length-displacement ratios Ⓜ = 5.411–5.174 (Fig. 9a). At $Fr_\nabla < 2.5$, the conventional spray rails increased the resistance by up to 6%. The increase in resistance was primarily due to an increase in the running trim due to an additional lift from the spray rails in the forebody that shifted the center of pressure forward.

The narrow triangular spray rails (Fig. 9d) reduced the resistance at $Fr_\nabla > 3$ significantly more (2.4%) than the conventional spray rails.

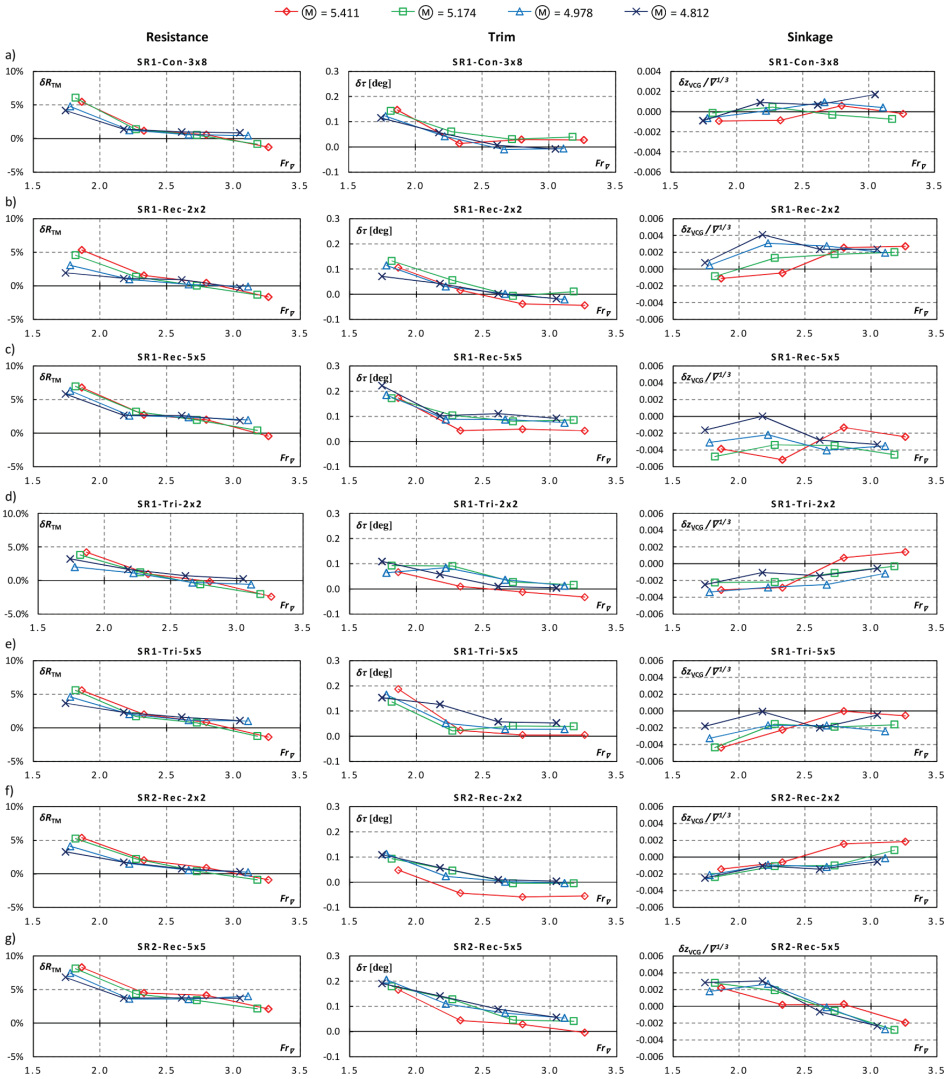

Fig. 9. Change in resistance, trim and sinkage of the tested spray rails arrangements compared to the bare hull.

They had a smaller spray rail width ($b_{SR} = 2$ mm) and a sharper bottom angle ($\delta = -25°$) compared to those of the conventional spray rails ($b_{SR} = 6$–8 mm, $\delta = 0°$).

Compared to the bare hull, the increase in the width of the spray rail from $b_{SR} = 2$ mm to $b_{SR} = 5$ mm increased the total resistance by 1.2–3.9% for the rectangular spray rails (Fig. 9b,c). In the case of triangular spray rails (Fig. 9d,e), the increase in resistance was smaller, 0.8–2.6%. The same applied to the spray rails extended to the transom (Fig. 9f,g): increasing the spray rail size also increased the total resistance by 3%. Larger spray rails produced more lift in the forebody shifting the centre of pressure forward, thereby increasing trim which caused the increase in resistance.

Increasing the bottom angle of the spray rail from $\delta = -70°$ to $\delta = -25°$, i.e. replacing the rectangular profile with the triangular one, decreased the total resistance by 0.5–1.1% in the case of narrow ($b_{SR} = 2$ mm) spray rails (Fig. 9b,d). With larger spray rails ($b_{SR} = 5$ mm, Fig. 9c, e), increasing the bottom angle of the spray reduced the resistance by 0.3–2.2%. The reason is that the spray rails with a larger bottom angle $\delta = -25°$ produced less lift in the forebody and therefore shifted the centre of pressure afterward, thereby decreasing trim, which caused the decrease in resistance.

Extending the narrow ($b_{SR} = 2$ mm) spray rails up to the transom resulted in an increase in the total resistance of 0.1–1.3% (Fig. 9b,f). Extending the wider ($b_{SR} = 5$ mm) spray rails up to the transom increased the resistance by 1–2.5% (Fig. 9c,g). Compared to the shorter spray rails (SR1), the influence of the longer spray rails (SR2) on the running position was negligible. Furthermore, at $Fr_\nabla > 3$, each of the shorter spray rails extended below the dynamic waterline (Fig. 3a). Hence, the most likely reason for the increase in resistance is increasing of viscous resistance due to a larger wetted surface of the longer spray rails.

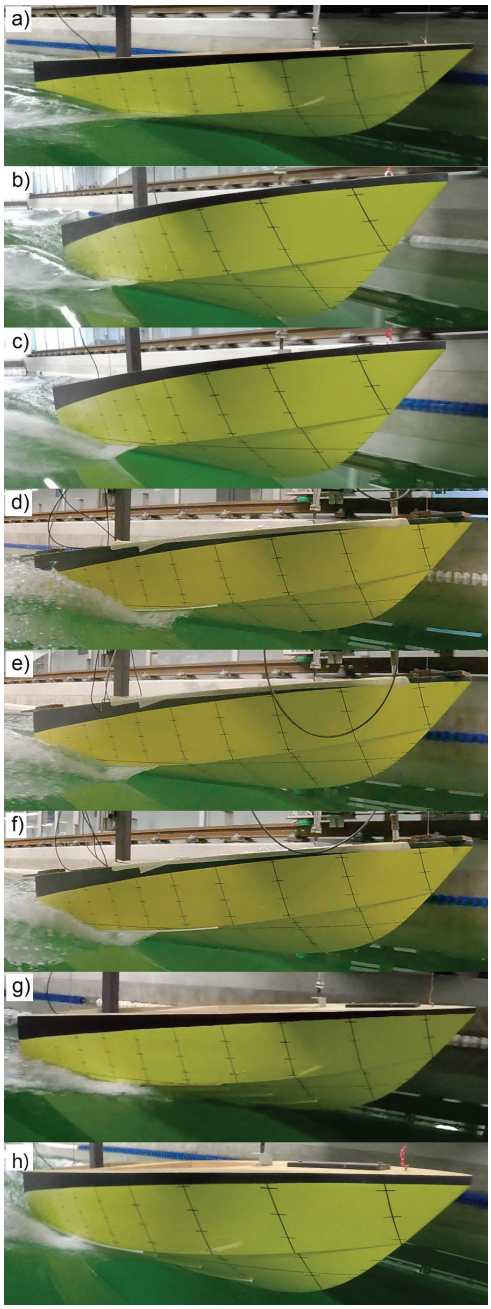

Fig. 10. Spray formation on the models equipped with chine strips at the design speed ($Fr_\nabla = 3.108$): (a) BH, (b) BH-C.INC, (c) BH-CSI1, (d) BH-CSI2, (e) BH-CSIR1, (f) BH-CSR2, (g) SR1-Rec-5×5-CSI1, (h) SR1-Rec-5×5-CSR2.

3.2. Chine strips

Fig. 10 compares the spray formation on the models equipped with chine strips at the design length-displacement ratio Ⓜ = 4.978 and the design speed of the craft $Fr_\nabla = 3.108$ Fig. 11. displays the change in the resistance and running position of the hulls with chine strips in comparison to the bare hull (Fig. 11a–c) and to the hull equipped with spray rails (Fig. 11c,d). The first two chine strips on the bare hull (C.INC and CSI1) (Fig. 11a,b) as well as the chine strips on the hulls equipped with spray rails (SR1-Rec-5×5-CSI1 and SR1-Rec-5×5-CR2, Fig. 11d,e) were tested at the beginning of the test campaign. Hence, they were tested at all four displacements Ⓜ = 4.812–5.411. The tests of the bare hull with the chine strips CSI1, CSI2, CSR1 and CSR2 (Fig. 11c) were run at the end of the test campaign and due to the lack of time and resources, these tests were only run at the design displacement Ⓜ = 4.978 (Table B.4).

Compared with the earlier tests (Fig. 11a,b,d,e), the chine strips tested at the end of the campaign (Fig. 11c) proved to increase the resistance significantly more at semi-displacement speeds and to reduce it less at the planing speed. After rerunning the bare hull at the end of the test campaign, it became evident that its surface had deteriorated due to multiple attachments of different spray rails. The total resistance of the bare hull had increased by 5%. However, the changes in the trim of the chine strip CSI1 (that had been tested twice) remained the same. Hence, the efficiency of the chine strips in Fig. 11c should be judged by the change in the trim rather than that in the resistance.

Unlike the spray rails on the bottom of the hull, the chine strips had a significantly more pronounced effect on the running position and therefore on the resistance of the craft. Compared to the bare hull, the chine strips reduced the running trim by up to 0.3° at planing speeds and increased it by up to 0.8° at semi-displacement speeds. That is 3-4 times more than in the case of spray rails on the bottom of the craft. These changes in the running trim were also accompanied by significant fluctuations in the total resistance. At semi-displacement speeds $Fr_\nabla < 2.5$, chine strips increased the resistance by up to 9%, while at planing speeds $Fr_\nabla > 2.5$, they reduced it by up to 3%. Furthermore, the change in the trim and resistance depended on the displacement: the higher the length-displacement ratio Ⓜ of the craft, the greater the reduction in the trim and resistance.

Compared to the rectangular chine strips (CSI1 and CSI2), the triangular chine strips (CSR1 and CSR2) increased the trim at semi-displacement speeds and decreased it more at planing speeds (Fig. 11c). This indicates that a larger effective chine surface and a sharper separation point of the spray of the triangular chine strips CSR1 and CSR2 yielded more lift. Also, the larger CSR2 reduced the trim more effectively than the smaller CSR1. The effect of the chine strips on the performance of the boat equipped with spray rails (Fig. 11d,e) was rather similar to that of the bare hull. Chine strips increased the running trim by up 0.3° at semi-displacement speeds and reduced it by up to 0.3° at planing speeds. Accordingly, the chine strips increased the resistance by up to 3.2% at semi-displacement speeds and reduced it by up to 3% at planing speeds.

The changes in the running position were most likely caused by the fact that the chine strips increased the lift and shifted the centre of pressure of the craft. Chine strips deflected the spray between the intersections of the chine with the dynamic waterline and the spray edge (Fig. 4a). At semi-displacement speeds $Fr_\nabla < 2.5$, the stagnation angle α is larger and therefore the spray area is located forward of the centre of gravity of the craft. At planing speeds $Fr_\nabla > 2.5$, the stagnation angle α is smaller and the spray area is located aft of the centre of gravity of the craft. Hence, at semi-displacement speeds, the chine strips shifted the centre of pressure forward, leading to an increase in the running trim. At planing speeds, the chine strips shifted the center of pressure aftward, causing a decrease in the running trim. This suggests that the chine strips could be shorter such that they would deflect the spray only at planing speeds. Also, at higher length-displacement ratios Ⓜ, the stagnation angle α is smaller and the spray area is located further aftward than at low length-displacement ratios. This explains the larger trim reductions at high length-displacement ratios.

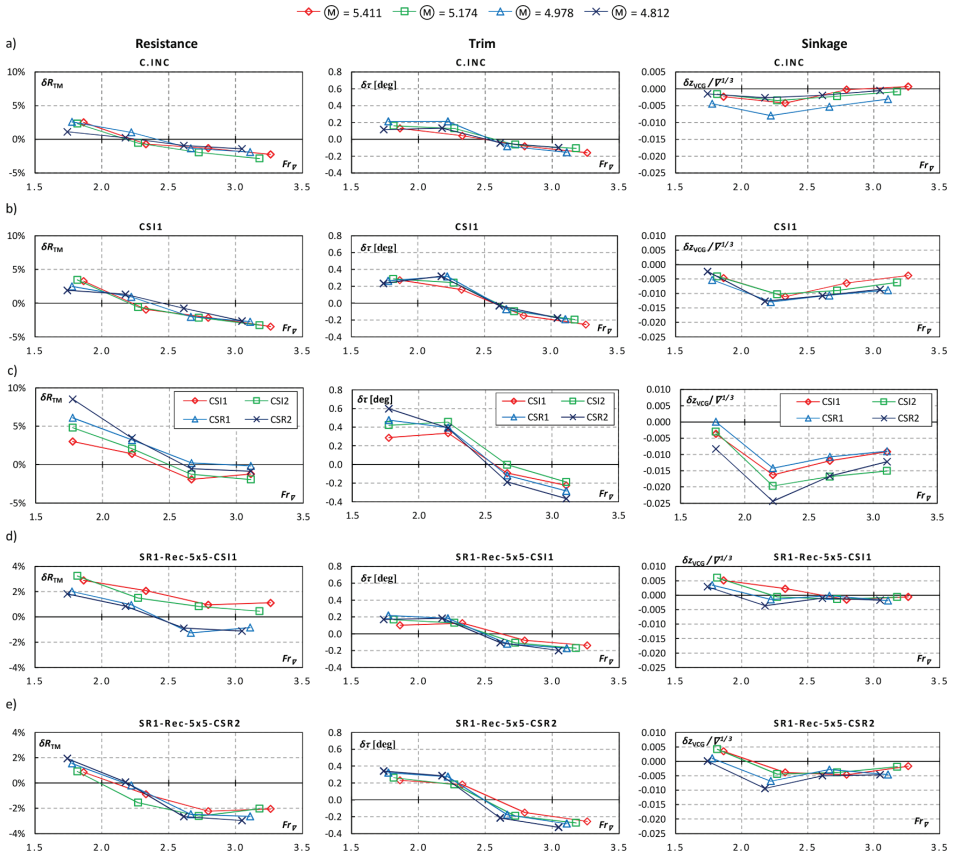

Fig. 11. Change in resistance, running trim and sinkage of the tested chine strip arrangements.

3.3. V-shaped spray interceptor

Fig. 12 compares the formation of spray on the model equipped with the VSI at the length displacement ratio Ⓜ = 4.978 and Fr_∇ = 1.776–3.108. The figures show that the VSI deflected the spray at planing speeds $Fr_\nabla > 2.5$ while at semi-displacement speeds $Fr_\nabla < 2.5$, spray deflection did not occur. Furthermore, a closer inspection of the spray deflection at lower and higher length-displacement ratios revealed that the VSI deflected the spray at all length displacement ratios at planing speeds Fig. 13. compares the change in the total resistance, trim and sinkage of the hull with VSI to those of the bare hull.

The effect of the VSI on the running trim and sinkage was either very small or within the uncertainty margins, hence negligible, which suggests that the changes in the lift and the position of the centre of pressure were negligible as well. At the planing speeds $Fr_\nabla > 2.5$, the V-shaped spray interceptors (VSI) reduced the total resistance by 2.1–4.2%, with the highest reductions occurring at a slightly slower speed and at a higher length-displacement ratio than those it was designed for (Fr_∇ = 3.108, Ⓜ = 4.978). At semi-displacement speeds $Fr_\nabla < 2.5$, the VSI increased the total resistance by 2.1–8.4%, with the highest and lowest increases in resistance occurring at high and low length-displacement ratios, respectively.

The negligible change in trim and sinkage indicates that at planing speeds ($Fr_\nabla > 2.5$), the VSI (located forward of the stagnation line and deflecting the spray as intended) produced on its deflection surface a forward reaction force that reduced the resistance. However, the change in the total resistance was dependent on the speed and length-displacement ratio. Compared with the design conditions (Fr_∇ = 3.108, Ⓜ = 4.978), the VSI was slightly more effective at reducing the resistance both at lower and higher Fr_∇. At lower Froude displacement numbers (Fr_∇ = 2.6–2.7, Ⓜ = 4.812–5.174), the stagnation angle α increases and the parallel normal distance *d* between the stagnation line and the VSI decreases. However, at a higher Froude displacement number (Fr_∇ = 3.178, Ⓜ = 5.174), the stagnation angle α is smaller and the parallel normal distance *d* between the stagnation line and the VSI increases. Similar effects were also observed in the study by Castaldi et al. (2021) that concluded that the parallel normal distance between the stagnation line and the VSI is the key factor influencing the performance of the VSI. Therefore, further investigations are required to identify the optimum position of the VSI.

The negligible change in trim and sinkage indicates that at semi-displacement speeds, the VSI increased the resistance primarily due to the high pressure on its front surface and the low pressure right behind it. Furthermore, the significantly lower increase in resistance at low length-displacement ratios Ⓜ = 4.812–4.978 could be explained by the fact that the VSI was located deeper, i.e. further away from the stagnation line and the undisturbed water surface. This increase in resistance at semi-planing speeds could be reduced by tapering the VSI from the chine to the keel and moving the leading edge forward, similar to the design proposed by Castaldi et al. (2021). Since the VSI does not deflect spray beyond the spray edge, it could be also limited in the vicinity of the keel, i.e. it could only slightly extend beyond the spray edge at the design speed.

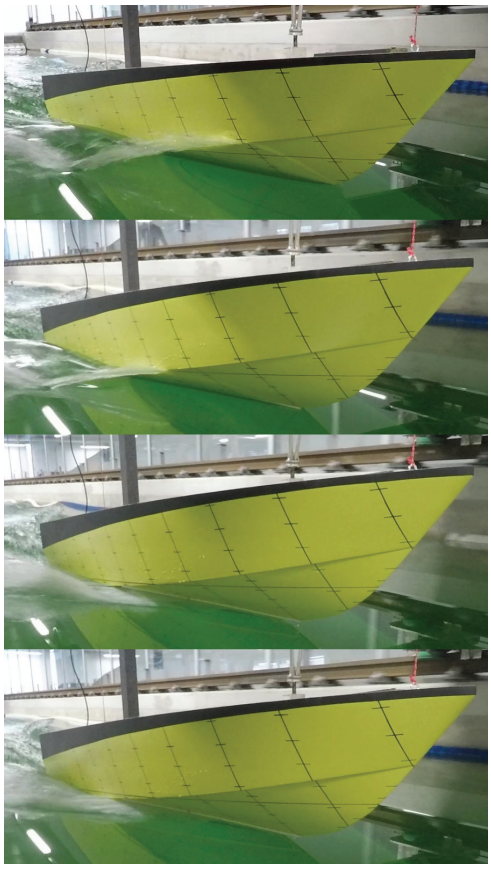

Fig. 12. Spray formation of the model with VSI at Ⓜ = 4.978 and Fr_∇ = 1.776, 2.220, 2.664, 3.108.

4. Conclusion

This study presents the results of an experimental series comprising a bare hull, seven spray rail arrangements, a V-shaped spray interceptor and seven chine strip variations on a slow planing craft (Fr_∇ = 1.742–3.261). The models were tested at four speeds and length-displacement ratios, totalling 228 individual test series.

4.1. Spray rails

Spray rails reduced the total resistance by up to 2.4% at high length-displacement ratios Ⓜ ≥ 5.174 and planing speeds $Fr_\nabla \geq 3$. At $Fr_\nabla < 2.5$, spray rails increased the total resistance by up to 8.3%. At $2.5 > Fr_\nabla < 3$, spray rails increased the resistance by up to 2% or their influence was within the uncertainty margin of 0.4%, hence negligible. In most cases, the increase in resistance resulted from an increase in the running trim.

Increasing the width b_{SR} and decreasing the bottom angle of the spray rails δ significantly increased the lift in the forebody and shifted the center of pressure forward, thereby increasing the running trim and the total resistance. This, in turn, negated any benefits gained from the deflection of the spray. These results confirm the general guidelines that the spray rails should not produce too much lift and that they should not extend aft of the stagnation line (Larsson et al., 2014). In other words, the spray rails should be as small in size and short as possible and they should be angled upward rather than downward.

However, spray rails with a smaller width and a sharper bottom angle (b_{SR} = 2 mm, $\delta = -25°$) performed better than horizontal spray rails with (b_{SR} = 7 mm, $\delta = 0°$). The most likely reason is that the sharper bottom angle ensured the separation (deflection) of the spray, while the smaller width of the spray rail caused less frictional resistance. This suggests that the distance of the outer edge of the spray rail from the bottom, which is a combination of the width b_{SR} and the bottom angle δ of the spray rail, is the key factor in the spray rail design.

4.2. Chine strips

Chine strips had a significant influence on the running position and the total resistance of both the bare hull and the hull equipped with spray rails. At planing speeds ($Fr_\nabla > 2.5$), the chine strips increased the lift aft of the centre of gravity and shifted the centre of pressure aftward, thereby reducing the running trim (up to 0.3°) and the total resistance (up to 3%). That is considerably less compared to the effect produced by the stern interceptors, which can reduce the running trim by more than 1 degree and the total resistance by more than 15% (De Luca and Pensa, 2012; Karimi et al., 2013; Avci and Barlas, 2019). At semi-displacement speeds ($Fr_\nabla < 2.5$), the chine strips increased lift forward of the centre of gravity and shifted the centre of pressure forward, thereby increasing the running trim (up to 0.3°) and the total resistance (up to 3%). Therefore, the chine strips should be designed to function only at planing speeds $Fr_\nabla > 2.5$, i.e. they should be shorter in the forebody, i.e. extend only slightly forward of the spray edge line. Aft of the stagnation line, the chine strips should be limited by the dynamic water line at the maximum speed and length-displacement ratio (Fr_∇ = 3.261, Ⓜ = 5.411). Chine strips are a simpler and possibly a more cost-efficient solution for trim reduction than stern interceptors or tabs. However, chine strips reduce the trim only at planing speeds $Fr_\nabla > 2.5$, while stern interceptors or tabs also reduce it at semi-displacement speeds $Fr_\nabla < 2.5$.

4.3. V-shaped spray interceptors

Since the VSIs were located forward of the stagnation line, they deflected the oncoming spray. This in turn induced a reaction force on the spray deflection surface of the VSI in the direction of the craft's motion, which reduced the resistance by up to 3% in the design condition (Fr_∇ = 3.108, Ⓜ = 5.411). The reduction in the total resistance was by up to 1.2% higher at a slightly lower speed and a higher length-displacement ratio. Furthermore, at planing speeds, the VSIs deflected the spray and reduced the total resistance also at higher and lower length displacement ratios.

4.4. Optimum design

Based on the findings in Sections 3.1 and 3.3, the optimum performance could be achieved if the craft is equipped both with narrow triangular spray rails (SR1-Tri-2×2, b_{SR} = 2 mm, $\delta = -25°$) and large triangular chine strips (CSR2, b_{CS} = 7 mm, $\delta_{CS} = -45°$). The spray rails and the chine strips should be optimized for $Fr_\nabla > 2$, i.e. they should be limited by the spray edge at Fr_∇ = 2.117. Then at $Fr_\nabla < 2$, the spray would be deflected only by the chine flare. Considering that the small triangular spray rails reduced the resistance by up to 2% and the chine strips CSR2 reduced it by 3%, when combined, they could reduce the resistance by up to 5%. However, if the goal is to deflect the spray also at semi-displacement speeds $Fr_\nabla < 2$ with the spray rails extended up to the stem, then chine strips are an insufficient means of reducing the trim. Thus, stern interceptors or tabs should be installed.

5. Future work

The optimum size of the spray rails for this particular craft is still unknown. The results of the present study suggest that the width of the spray rail should be minimized, while its bottom angle should be

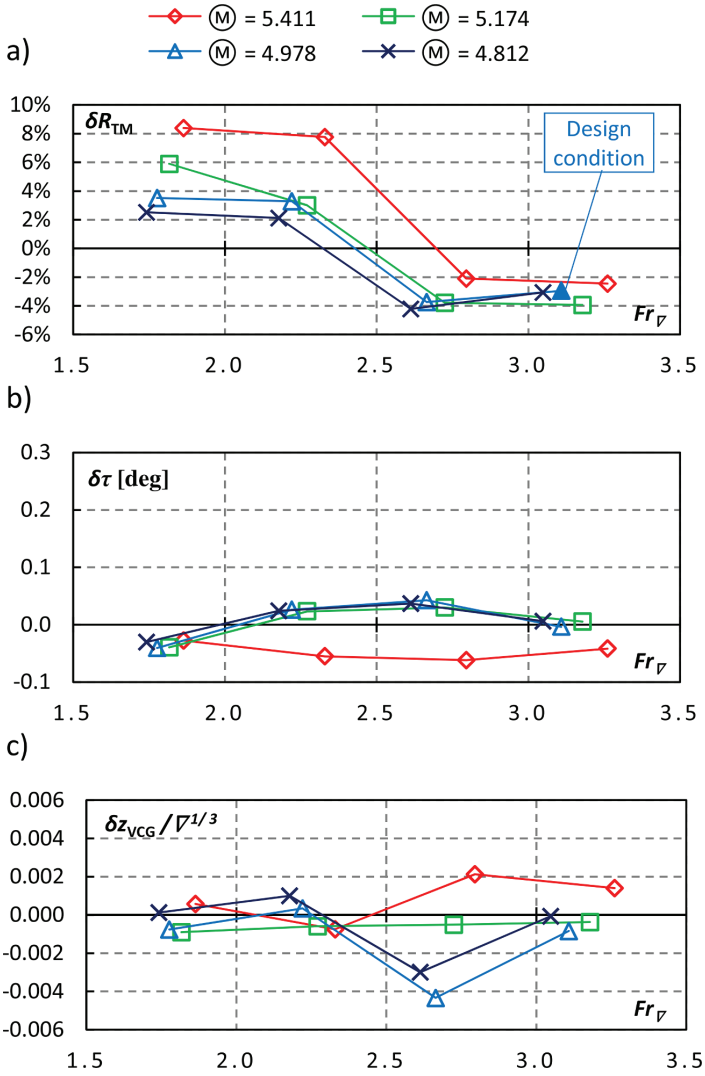

Fig. 13. Change in resistance (a), trim (b) and sinkage (c) of the VSI compared to the bare hull.

maximized. This also implies the need to identify a profile that does not deflect the spray. It is not known what the effect of various spray rail profiles on the running trim of a craft equipped with stern interceptors would be. Therefore, future investigations need to include the effect of different spray rails on the performance of a craft equipped with stern interceptors. Future studies should also investigate the influence of the width b_{SR} and bottom angle δ of the spray rails on the seakeeping and manoeuvring performance of the craft.

Further investigations are needed to establish the optimum position of the VSI for the design condition of the vessel. Currently, only VSIs with deflection surfaces normal to the hull have been experimentally investigated. Future studies should examine the effect of the height and the bottom angle of the VSI on the performance of the hull. Since high-speed craft operate most of the time in waves, the effect of the VSIs on the accelerations should be studied. Additional tests are needed to establish whether the ventilation observed in previous studies (Castaldi et al., 2021) would occur again and reduce the resistance at $Fr_{\nabla} \approx 2.5$.

At planing speeds in calm water, chine strips significantly reduce the running trim and the total resistance by shifting the center of pressure aftward. However, it is unknown how the chine strips affect the running position of the craft in waves when the position of the intersection of the stagnation line and of the chine oscillates. Further investigations are required to establish whether the chine strips can cause dynamic pitch-heave oscillation, i.e. porpoising.

CRediT authorship contribution statement

Mikloš Lakatoš: Conceptualization, Investigation, Validation, Formal analysis, Visualization, Writing – original draft. **Tarmo Sahk:** Methodology, Investigation, Software, Data curation. **Henrik Andreasson:** Conceptualization, Methodology, Writing – review & editing. **Kristjan Tabri:** Supervision, Project administration, Funding acquisition, Writing – review & editing.

Declaration of Competing Interest

The authors declare that they have no known competing financial interests or personal relationships that could have appeared to influence the work reported in this paper.

Acknowledgments

This research work was financed by the Estonian Research Council via grant PRG83 (Numerical simulation of the FSI for the dynamic loads and response of ships) and by the European Regional Development Fund via grant 2014-2020.5.04.19-0385 (Small Craft Competence Centre–analysis of the impact of external construction elements on the performance of a vessel, transfer of know-how and information). This help is gratefully appreciated. We also thank Associate Professor Ermina Begovic (University of Naples Federico II) and Contract Professor Simone Mancini (Giustino Fortunato University) for their comments on the manuscript.

Appendix A. Laboratory instrumentation and measurements

The calm water towing tests were conducted in the towing tank of SCC (see Table A.1) following the ITTC guidelines 7.5-02-02-01 (28th ITTC, 2017). The models were tested in semi-captive conditions (Fig. A.1), i.e. the models were free to pitch and heave. During the tests, total resistance R_{TM} and running sinkage at the aft and fore perpendiculars z_{VF} and z_{VA} were measured at sampling frequency of 200 Hz . The numbers of repeated runs and the data acquisition times are shown in Table A.2.

The running trim angle τ of the craft was evaluated from the readings of running sinkage at the aft (z_{VA}) and the bow (z_{VF}) perpendiculars that were measured with a linear measuring wire and a draw-wire encoder with the bias of 0.05% in a range of ±1250 mm Fig. A.2.b shows an example time history of data acquisition (DA) of readings of the draught change in the aft (z_{VA}) and the bow (z_{VF}). The uncertainty analysis was carried out following the ITTC guidelines 7.5-02-02-02 and 7.5-02-02-02.1 (27th ITTC 2014a, 2014b) Table A.3. shows the uncertainties of resistance, trim and sinkage in the design condition of the craft.

The bias of the dynamometer was 0.2% in the range of 0–0.2 kN. The dynamometer was calibrated before the model test according to the ITTC Procedure 7.5-01-03-01 (28th ITTC, 2017). Five loads were implemented by weights and randomly applied three times for each load. The fitting curve for predicting the force was obtained by linear regression with a standard deviation of SEE = 0.077 N Fig. A.2.a shows an example time history of data acquisition (DA) of readings of R_{TM} from the dynamometer.

Table A.1
Main dimensions of the towing tank.

Parameter		
Maximum tank length	l	60 m
Maximum tank breadth	b	5 m
Maximum tank depth	h	3 m
Maximum carriage speed	V	5.5 m/s

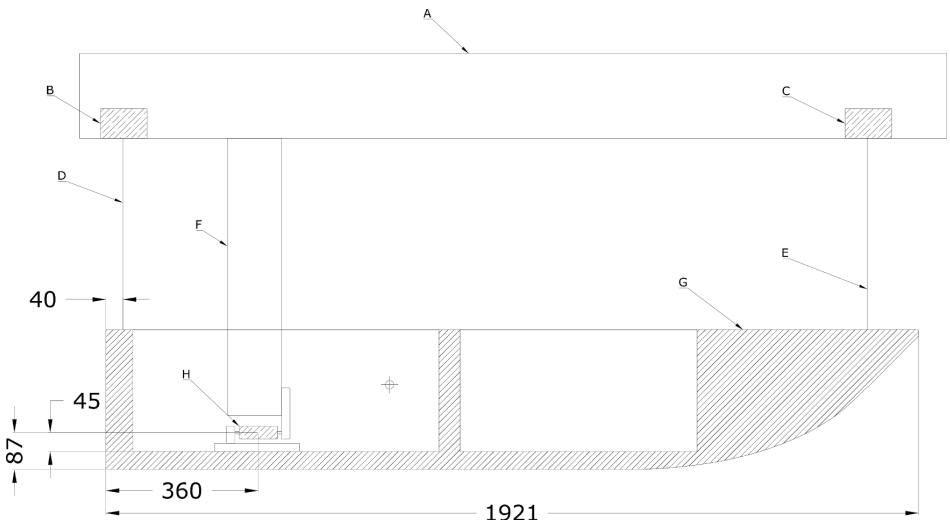

Fig. A.1. Semi-captive model test setup: A–carriage, B & C–wire encoder, D & E–linear measuring wire, F–carriage arm, G–test model, H–force gauge.

Table A.2
Numbers of repeated runs and data acquisition times.

V_M [m/s]	No. of Repeated Runs	Data Acquisition Time [s]
3.254	2-4	9
4.067	2-4	6
4.880	2-5	4
5.694	2-6	3

The tachometer was calibrated at 1, 2, 3, 4 and 5 m/s, four runs for each speed except for the speed 1 m/s, which was run 6 times. The fitting curve for predicting the speed was obtained by linear regression with a standard deviation of SEE = 0.0011 m/s Fig. A.2.a,b shows an example time history of data acquisition (DA) of readings of the model speed V_M from the tachometer. The temperature of the water in the tank was measured once a day with a K-type thermo-couple the bias of which is 1 °C in a range of −40 °C to 1372°.

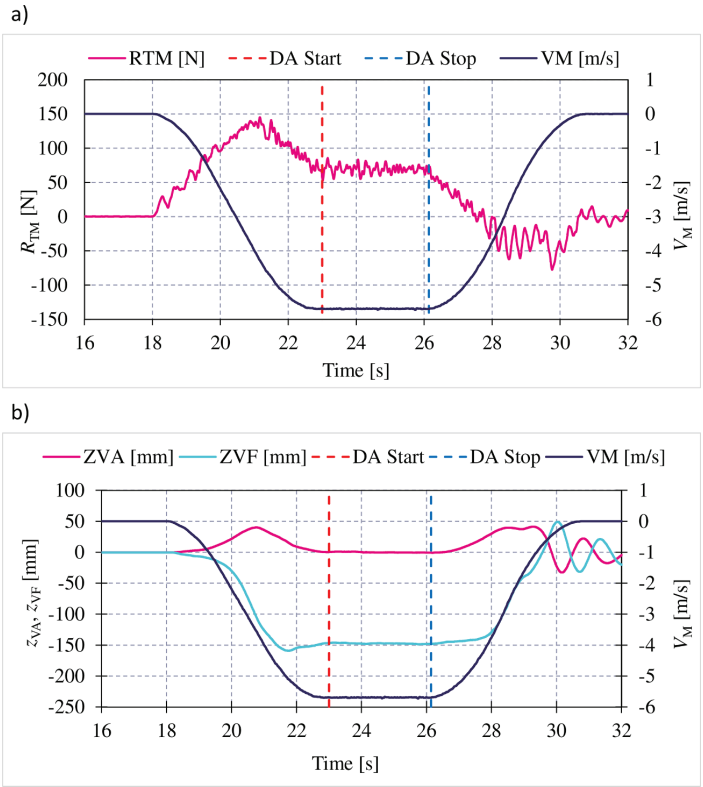

Fig. A.2. Time histories of data acquisition of measured quantities (Ⓜ = 4.978, Fr = 1.393 and Fr_∇ = 3.108): (a) resistance R_{TM} and speed V_M of the model, (b) sinkage at the aft and the fore perpendiculars z_{VA} and z_{VF} and speed V_M of the model.

Table A.3
Uncertainty components of resistance, trim and sinkage of the bare hull (BH) in the design condition Ⓜ = 4.978.

Uncertainty component Number of repeated runs N	Type	Fr_∇ =1.816 4		Fr_∇ = 2.220 4		Fr_∇ = 2.664 4		Fr_∇ = 3.108 5	
Resistance R_{TM} (t=16.4°C)									
Wetted area	B	0.02%	negligible	0.02%	negligible	0.02%	negligible	0.02%	negligible
Speed	B	0.02%	negligible	0.02%	negligible	0.02%	negligible	0.01%	negligible
Water temp.	B	0.04%	minor	0.04%	minor	0.04%	minor	0.05%	minor
Dynamometer (ν = 15)	A	0.14%	dominant	0.12%	dominant	0.11%	minor	0.11%	dominant
Repeat test, Deviation of mean	A	0.05%	minor	0.04%	minor	0.17%	dominant	0.10%	minor
Combined for repeat mean	u'_C (R_{TM})	0.15%		0.13%		0.21%		0.16%	
Expanded for repeat mean	U'_p (R_{TM})	0.31%		0.27%		0.42%		0.32%	
Trim τ [deg]									
Potentiometer	B	0.014	dominant	0.014	dominant	0.014	dominant	0.014	dominant
Repeat test, Deviation of mean	A	0.003	minor	0.012	minor	0.009	minor	0.005	minor
Combined for repeat mean	u_c (τ)	0.014		0.018		0.016		0.015	
Expanded for repeat mean	U_p (τ)	0.028		0.036		0.033		0.029	
Sinkage zVCG [mm]									
Potentiometer	B	0.29	dominant	0.29	dominant	0.29	dominant	0.29	dominant
Repeat test, Deviation of mean	A	0.07	minor	0.26	minor	0.20	minor	0.11	minor
Combined for repeat mean	u_c (z_{VCG})	0.30		0.39		0.36		0.31	
Expanded for repeat mean	U_p (z_{VCG})	0.61		0.78		0.71		0.63	

Appendix B. Model test results

Table B.1
Total resistance R_{TM}/Δ and corresponding relative expanded uncertainty U_p (R_{TM}/Δ) of tested spray rail variations.

Hull		R_{TM}/Δ [-]				U_p (R_{TM}/Δ) = $k_p u_c$ (R_{TM}/Δ)			
	C_V	Ⓜ = $L_{WL}/\nabla^{1/3}$				Ⓜ = $L_{WL}/\nabla^{1/3}$			
	[-]	5.411	5.174	4.978	4.812	5.411	5.174	4.978	4.812
BH	1.469	0.133	0.138	0.143	0.150	0.001	0.001	0.000	0.000
	1.837	0.159	0.162	0.167	0.174	0.001	0.001	0.000	0.001
	2.204	0.173	0.173	0.174	0.177	0.001	0.001	0.001	0.000
	2.571	0.190	0.184	0.179	0.179	0.001	0.001	0.001	0.001
SR-Con-3×8	1.469	0.141	0.146	0.150	0.156	0.001	0.001	0.001	0.000
	1.837	0.161	0.165	0.169	0.176	0.001	0.001	0.001	0.001
	2.204	0.174	0.174	0.175	0.179	0.001	0.001	0.000	0.000
	2.571	0.188	0.182	0.180	0.181	0.001	0.001	0.001	0.000
SR1-Rec-2×2	1.469	0.141	0.144	0.147	0.153	0.001	0.001	0.001	0.000
	1.837	0.161	0.165	0.168	0.176	0.001	0.001	0.001	0.001
	2.204	0.174	0.173	0.174	0.179	0.001	0.001	0.001	0.001
	2.571	0.187	0.181	0.179	0.179	0.001	0.001	0.000	0.001
SR1-Rec-5×5	1.469	0.142	0.147	0.152	0.158	0.001	0.001	0.001	0.000
	1.837	0.163	0.168	0.171	0.178	0.001	0.001	0.001	0.001
	2.204	0.176	0.176	0.178	0.182	0.001	0.001	0.000	0.001
	2.571	0.190	0.185	0.183	0.183	0.001	0.001	0.000	0.001
SR1-Tri-2×2	1.469	0.139	0.143	0.146	0.155	0.001	0.001	0.000	0.001
	1.837	0.160	0.164	0.168	0.177	0.001	0.000	0.000	0.000
	2.204	0.173	0.172	0.174	0.179	0.001	0.001	0.001	0.001
	2.571	0.186	0.180	0.178	0.180	0.001	0.001	0.001	0.000
SR1-Tri-5×5	1.469	0.141	0.145	0.150	0.155	0.001	0.001	0.001	0.001
	1.837	0.162	0.165	0.170	0.178	0.001	0.001	0.001	0.001
	2.204	0.174	0.174	0.176	0.180	0.001	0.001	0.001	0.000
	2.571	0.188	0.182	0.181	0.181	0.001	0.002	0.001	0.000
SR2-Rec-2×2	1.469	0.141	0.145	0.149	0.155	0.001	0.001	0.001	0.001
	1.837	0.162	0.166	0.169	0.177	0.001	0.001	0.001	0.000
	2.204	0.174	0.173	0.175	0.179	0.001	0.001	0.001	0.001
	2.571	0.189	0.182	0.180	0.180	0.001	0.001	0.001	0.000
SR2-Rec-5×5	1.469	0.144	0.149	0.154	0.160	0.001	0.000	0.001	0.001
	1.837	0.166	0.169	0.173	0.180	0.001	0.001	0.001	0.000
	2.204	0.180	0.178	0.180	0.184	0.001	0.001	0.000	0.001
	2.571	0.194	0.188	0.187	0.186	0.001	0.001	0.001	0.001
BH-C.INC	1.469	0.137	0.141	0.147	0.151	0.001	0.001	0.001	0.000
	1.837	0.158	0.161	0.168	0.174	0.001	0.001	0.001	0.001
	2.204	0.171	0.169	0.172	0.176	0.001	0.001	0.001	0.001
	2.571	0.186	0.179	0.176	0.177	0.001	0.001	0.001	0.001
BH-CSI1	1.469	0.138	0.142	0.147	0.153	0.001	0.000	0.001	0.000
	1.837	0.157	0.161	0.168	0.176	0.001	0.001	0.000	0.001
	2.204	0.169	0.169	0.171	0.176	0.001	0.001	0.001	0.000
	2.571	0.184	0.178	0.174	0.174	0.001	0.001	0.000	0.001
SR1-Rec-5×5-CSI	1.469	0.147	0.152	0.155	0.161	0.001	0.000	0.001	0.001
	1.837	0.166	0.170	0.172	0.180	0.001	0.001	0.001	0.000
	2.204	0.178	0.178	0.176	0.180	0.001	0.001	0.001	0.001
	2.571	0.192	0.186	0.181	0.181	0.001	0.001	0.001	0.001
SR1-Rec-5×5-CSR	1.469	0.144	0.149	0.154	0.161	0.001	0.001	0.001	0.000
	1.837	0.162	0.165	0.171	0.179	0.001	0.001	0.000	0.000
	2.204	0.172	0.171	0.174	0.177	0.001	0.001	0.001	0.001
	2.571	0.186	0.181	0.178	0.177	0.001	0.001	0.001	0.000
VSI-Tri-5×5	1.469	0.145	0.146	0.148	0.153	0.001	0.003	0.000	0.001
	1.837	0.171	0.167	0.172	0.178	0.001	0.001	0.000	0.001
	2.204	0.169	0.166	0.168	0.170	0.001	0.001	0.001	0.001
	2.571	0.186	0.177	0.174	0.174	0.001	0.001	0.001	0.001

Table B.2
Running trim τ and corresponding expanded uncertainty $U_p(\tau)$ of the tested spray rail configurations.

Hull		τ [deg] $Ⓜ = L_{WL}/\nabla^{1/3}$				$U_p(\tau) = k_p u_c(\tau)$ [deg] $Ⓜ = L_{WL}/\nabla^{1/3}$			
	C_V								
	[-]	5.411	5.174	4.978	4.812	5.411	5.174	4.978	4.812
BH	1.469	3.533	3.949	4.337	4.762	0.028	0.032	0.028	0.030
	1.837	4.297	4.864	5.409	6.022	0.030	0.031	0.036	0.040
	2.204	4.255	4.785	5.360	5.851	0.029	0.030	0.033	0.030
	2.571	3.852	4.267	4.776	5.165	0.029	0.029	0.029	0.041
SR-Con-3×8	1.469	3.680	4.092	4.459	4.877	0.029	0.032	0.031	0.027
	1.837	4.310	4.924	5.451	6.079	0.037	0.030	0.039	0.047
	2.204	4.284	4.815	5.349	5.857	0.030	0.032	0.031	0.029
	2.571	3.880	4.307	4.770	5.157	0.030	0.029	0.030	0.030
SR1-Rec-2×2	1.469	3.639	4.082	4.451	4.833	0.029	0.034	0.030	0.036
	1.837	4.312	4.919	5.440	6.064	0.037	0.033	0.033	0.037
	2.204	4.216	4.777	5.361	5.853	0.031	0.030	0.031	0.037
	2.571	3.809	4.277	4.755	5.147	0.029	0.032	0.034	0.036
SR1-Rec-5×5	1.469	3.706	4.122	4.522	4.984	0.032	0.032	0.055	0.033
	1.837	4.340	4.968	5.497	6.124	0.031	0.037	0.054	0.064
	2.204	4.304	4.865	5.448	5.962	0.031	0.035	0.033	0.038
	2.571	3.896	4.353	4.852	5.257	0.032	0.030	0.030	0.030
SR1-Tri-2×2	1.469	3.599	4.042	4.401	4.872	0.029	0.032	0.028	0.030
	1.837	4.306	4.955	5.493	6.080	0.045	0.033	0.028	0.047
	2.204	4.242	4.812	5.396	5.860	0.032	0.036	0.031	0.033
	2.571	3.820	4.284	4.789	5.169	0.031	0.035	0.032	0.032
SR1-Tri-5×5	1.469	3.720	4.086	4.502	4.915	0.036	0.043	0.034	0.085
	1.837	4.320	4.884	5.461	6.147	0.027	0.052	0.049	0.035
	2.204	4.259	4.825	5.388	5.908	0.041	0.029	0.029	0.037
	2.571	3.857	4.306	4.804	5.217	0.032	0.032	0.029	0.031
SR2-Rec-2×2	1.469	3.581	4.043	4.450	4.872	0.032	0.030	0.034	0.030
	1.837	4.253	4.910	5.433	6.080	0.040	0.028	0.050	0.047
	2.204	4.196	4.781	5.362	5.860	0.033	0.027	0.032	0.033
	2.571	3.798	4.263	4.773	5.169	0.031	0.028	0.029	0.032
SR2-Rec-5×5	1.469	3.699	4.128	4.542	4.953	0.041	0.033	0.030	0.044
	1.837	4.341	4.991	5.519	6.163	0.029	0.030	0.035	0.030
	2.204	4.283	4.830	5.433	5.939	0.031	0.034	0.030	0.033
	2.571	3.848	4.308	4.829	5.221	0.028	0.032	0.032	0.038
BH-C.INC	1.469	3.663	4.110	4.548	4.878	0.034	0.033	0.034	0.037
	1.837	4.339	4.993	5.621	6.154	0.036	0.031	0.037	0.037
	2.204	4.173	4.720	5.277	5.807	0.031	0.029	0.031	0.034
	2.571	3.693	4.160	4.621	5.065	0.036	0.038	0.032	0.038
BH-CSI1	1.469	3.807	4.238	4.602	4.998	0.033	0.027	0.037	0.037
	1.837	4.457	5.107	5.727	6.342	0.030	0.031	0.031	0.048
	2.204	4.107	4.690	5.290	5.821	0.049	0.047	0.032	0.037
	2.571	3.600	4.072	4.586	4.990	0.041	0.038	0.030	0.044
SR1-Rec-5×5-CSI	1.469	3.807	4.289	4.740	5.154	0.029	0.036	0.029	0.037
	1.837	4.466	5.097	5.682	6.308	0.068	0.037	0.035	0.043
	2.204	4.225	4.758	5.328	5.856	0.031	0.040	0.032	0.032
	2.571	3.759	4.181	4.679	5.060	0.030	0.031	0.032	0.034
SR1-Rec-5×5-CSR	1.469	3.938	4.385	4.843	5.326	0.033	0.032	0.033	0.040
	1.837	4.521	5.149	5.773	6.409	0.030	0.034	0.031	0.028
	2.204	4.153	4.675	5.271	5.746	0.029	0.030	0.032	0.036
	2.571	3.639	4.078	4.568	4.931	0.032	0.030	0.035	0.031
VSI-Tri-5×5	1.469	3.505	3.910	4.296	4.732	0.038	0.034	0.028	0.032
	1.837	4.241	4.887	5.435	6.046	0.028	0.037	0.030	0.042
	2.204	4.193	4.815	5.402	5.887	0.039	0.057	0.034	0.032
	2.571	3.811	4.273	4.773	5.171	0.030	0.032	0.030	0.039

Table B.3
Running sinkage $z_{VCG}/\nabla^{1/3}$ and expanded uncertainty U_p ($z_{VCG}/\nabla^{1/3}$) of the tested spray rail configurations.

Hull	C_V	$z_{VCG}/\nabla^{1/3}$ Ⓜ = $L_{WL}/\nabla^{1/3}$				U_p ($z_{VCG}/\nabla^{1/3}$) = $k_p u_c$ ($z_{VCG}/\nabla^{1/3}$) Ⓜ = $L_{WL}/\nabla^{1/3}$			
	[-]	5.411	5.174	4.978	4.812	5.411	5.174	4.978	4.812
BH	1.469	-0.030	-0.030	-0.028	-0.029	0.001	0.001	0.001	0.001
	1.837	-0.076	-0.081	-0.083	-0.090	0.001	0.001	0.001	0.002
	2.204	-0.117	-0.124	-0.128	-0.138	0.001	0.001	0.001	0.001
	2.571	-0.140	-0.148	-0.154	-0.165	0.001	0.001	0.001	0.002
SR-Con-3×8	1.469	-0.031	-0.030	-0.029	-0.030	0.001	0.001	0.001	0.001
	1.837	-0.077	-0.081	-0.083	-0.089	0.002	0.001	0.002	0.002
	2.204	-0.116	-0.124	-0.127	-0.137	0.001	0.002	0.001	0.001
	2.571	-0.140	-0.149	-0.154	-0.163	0.001	0.001	0.001	0.001
SR1-Rec-2×2	1.469	-0.031	-0.031	-0.028	-0.029	0.001	0.002	0.001	0.002
	1.837	-0.076	-0.080	-0.080	-0.086	0.002	0.001	0.002	0.002
	2.204	-0.114	-0.122	-0.126	-0.136	0.001	0.001	0.001	0.002
	2.571	-0.137	-0.146	-0.152	-0.163	0.001	0.001	0.001	0.001
SR1-Rec-5×5	1.469	-0.034	-0.035	-0.031	-0.031	0.002	0.001	0.002	0.001
	1.837	-0.081	-0.085	-0.085	-0.090	0.001	0.002	0.002	0.003
	2.204	-0.118	-0.127	-0.132	-0.141	0.002	0.002	0.001	0.002
	2.571	-0.142	-0.152	-0.158	-0.168	0.002	0.001	0.001	0.001
SR1-Tri-2×2	1.469	-0.033	-0.033	-0.031	-0.032	0.001	0.001	0.001	0.001
	1.837	-0.079	-0.084	-0.086	-0.091	0.002	0.001	0.001	0.002
	2.204	-0.116	-0.125	-0.131	-0.139	0.002	0.002	0.001	0.001
	2.571	-0.138	-0.148	-0.155	-0.166	0.001	0.002	0.001	0.001
SR1-Tri-5×5	1.469	-0.034	-0.035	-0.031	-0.031	0.002	0.002	0.002	0.004
	1.837	-0.078	-0.083	-0.085	-0.090	0.001	0.002	0.002	0.001
	2.204	-0.117	-0.125	-0.130	-0.140	0.002	0.001	0.001	0.002
	2.571	-0.140	-0.149	-0.157	-0.165	0.002	0.001	0.001	0.001
SR2-Rec-2×2	1.469	-0.031	-0.033	-0.030	-0.032	0.002	0.001	0.002	0.001
	1.837	-0.076	-0.083	-0.084	-0.091	0.002	0.001	0.002	0.002
	2.204	-0.115	-0.125	-0.129	-0.139	0.002	0.001	0.001	0.001
	2.571	-0.138	-0.147	-0.154	-0.166	0.002	0.001	0.001	0.001
SR2-Rec-5×5	1.469	-0.028	-0.028	-0.026	-0.027	0.002	0.002	0.001	0.002
	1.837	-0.076	-0.080	-0.080	-0.087	0.001	0.001	0.001	0.001
	2.204	-0.117	-0.124	-0.128	-0.139	0.002	0.002	0.001	0.001
	2.571	-0.142	-0.151	-0.157	-0.167	0.001	0.001	0.001	0.002
BH-C.INC	1.469	-0.032	-0.032	-0.033	-0.031	0.002	0.002	0.001	0.002
	1.837	-0.080	-0.085	-0.091	-0.093	0.002	0.001	0.002	0.001
	2.204	-0.117	-0.126	-0.134	-0.140	0.002	0.001	0.001	0.001
	2.571	-0.139	-0.149	-0.157	-0.166	0.002	0.002	0.001	0.002
BH-CSI1	1.469	-0.035	-0.034	-0.033	-0.032	0.002	0.001	0.002	0.002
	1.837	-0.087	-0.092	-0.096	-0.103	0.002	0.001	0.001	0.002
	2.204	-0.123	-0.133	-0.139	-0.149	0.002	0.002	0.001	0.002
	2.571	-0.144	-0.154	-0.163	-0.174	0.002	0.002	0.001	0.002
SR1-Rec-5×5-CSI	1.469	-0.029	-0.029	-0.028	-0.028	0.001	0.002	0.001	0.002
	1.837	-0.079	-0.085	-0.086	-0.093	0.003	0.002	0.001	0.002
	2.204	-0.120	-0.128	-0.132	-0.142	0.001	0.002	0.001	0.001
	2.571	-0.143	-0.153	-0.160	-0.170	0.001	0.001	0.001	0.001
SR1-Rec-5×5-CSR	1.469	-0.030	-0.031	-0.030	-0.031	0.002	0.001	0.002	0.002
	1.837	-0.085	-0.089	-0.092	-0.099	0.001	0.002	0.001	0.001
	2.204	-0.123	-0.131	-0.135	-0.146	0.001	0.001	0.001	0.002
	2.571	-0.144	-0.154	-0.162	-0.173	0.002	0.001	0.002	0.001
VSI-Tri-5×5	1.469	-0.029	-0.031	-0.029	-0.029	0.002	0.002	0.001	0.001
	1.837	-0.077	-0.082	-0.082	-0.089	0.001	0.002	0.001	0.002
	2.204	-0.115	-0.124	-0.133	-0.141	0.002	0.002	0.001	0.001
	2.571	-0.138	-0.148	-0.155	-0.165	0.001	0.001	0.001	0.002

Table B.4
Resistance, trim and sinkage of the bare hull equipped with different chine strips at the end of the experimental campaign.

Fr_∇	R_{TM}/Δ [-]					U_p (R_{TM}/Δ) = $k_p u_c$ (R_{TM}/Δ)				
[-]	BH2	CSI1	CSI2	CSR1	CSR2	BH2	CSI1	CSI2	CSR1	CSR2
1.776	0.149	0.154	0.156	0.158	0.162	0.001	0.001	0.000	0.001	0.001
2.220	0.175	0.178	0.179	0.181	0.181	0.001	0.001	0.001	0.000	0.001
2.664	0.182	0.178	0.180	0.182	0.181	0.001	0.001	0.001	0.001	0.001
3.108	0.187	0.185	0.183	0.187	0.185	0.001	0.001	0.001	0.001	0.001
Fr_∇	τ [deg]					U_p (τ) = $k_p u_c(\tau)$ [deg]				
[-]	BH2	CSI1	CSI2	CSR1	CSR2	BH2	CSI1	CSI2	CSR1	CSR2
1.776	4.576	4.863	4.996	5.050	5.173	0.029	0.031	0.029	0.035	0.032
2.220	5.691	6.026	6.145	6.085	6.081	0.036	0.030	0.032	0.036	0.035
2.664	5.577	5.485	5.573	5.460	5.389	0.031	0.029	0.041	0.032	0.035
3.108	4.965	4.741	4.775	4.681	4.599	0.032	0.039	0.035	0.039	0.029
Fr_∇	$z_{VCG}/\nabla^{1/3}$					U_p ($z_{VCG}/\nabla^{1/3}$) = $k_p u_c$ ($z_{VCG}/\nabla^{1/3}$)				
[-]	BH2	CSI1	CSI2	CSR1	CSR2	BH2	CSI1	CSI2	CSR1	CSR2
1.776	-0.033	-0.037	-0.036	-0.033	-0.041	0.001	0.001	0.001	0.001	0.001
2.220	-0.088	-0.104	-0.107	-0.102	-0.112	0.001	0.001	0.001	0.002	0.002
2.664	-0.135	-0.147	-0.152	-0.145	-0.151	0.001	0.001	0.002	0.001	0.002
3.108	-0.160	-0.169	-0.175	-0.169	-0.172	0.001	0.002	0.002	0.002	0.001

References

Savitsky, D., Morabito, M., 2011. Origin and characteristics of the spray patterns generated by planing hulls. J. Ship. Prod. Des. 27, 63–83.

Savitsky, D., 1964. Hydrodynamic design of planing hulls. Mar. Technol. 1, 71–94.

Savitsky, D., DeLorme, M.F., Datla, R., 2007. Inclusion of whisker spray drag in performance prediction method for high-speed planing hulls. Mar. Technol. 44, 35–56.

Begovic, E., Bertorello, C., 2012. Resistance assessment of warped hull form. Ocean Eng. 56, 28–42. https://doi.org/10.1016/j.oceaneng.2012.08.004.

Clement, E. P. 1964a. Effects of Longitudinal Bottom Spray Strips on Planing Boat Resistance. David Taylor Model Basin, Department of The Navy, Report No. 1818, February. Retrieved from https://dome.mit.edu/handle/1721.3/49089?show=full.

Clement, E. P. 1964b. Reduction of Planing Boat Resistance by Deflection of the Whisker Spray. David Taylor Model Basin, Department of The Navy, Report No. 1929, November. Retrieved from https://dome.mit.edu/handle/1721.3/49020?show=full.

Grigoropoulos, G., Loukakis, T., 1995. Effect of spray rails on the resistance of planing hulls. In: Proceedings of the 3rd International Conference on Fast Sea Transportation, FAST' 95. Travenmuende, Germany.

Kapryan, Walter J., Boyd Jr., George M., 1953. The Effect of Vertical Chine Strips on the Planing Characteristics of V-Shaped Prismatic Surfaces Having Angles of Dead Rise of 20 Degrees and 40 Degrees. Technical Note 3052, October. Langley Aeronautical Laboratory, NACA, Langley Field, Va. https://ntrs.nasa.gov/citations/19930083704.

Chambliss, Derrill B, Boyd Jr., George M, 1953. The Planing Characteristics of Two V-shaped Prismatic Surfaces Having Angles of Dead Rise of 20 Degrees and 40 Degrees. Technical Note 2876, January. Langley Aeronautical Laboratory, NACA, Langley Field, Va. https://ntrs.nasa.gov/citations/19930083757.

Kapryan, Walter J, Weinstein, Irving, 1952. The Planing Characteristics of a Surface Having a Basic Angle of Dead Rise of 20 Degrees and Horizontal Chine Flare. Technical Note 2804, October. Langley Aeronautical Laboratory, NACA, Langley Field, Va. Va. https://ntrs.nasa.gov/citations/19930083524.

Blanchard, Ulysse J, 1952. The Planing Characteristics of a Surface Having a Basic Angle of Dead Rise of 40 Degrees and Horizontal Chine Flare. Technical Note 2842, December. Langley Aeronautical Laboratory, NACA, Langley Field, Va. https://ntrs.nasa.gov/citations/19930083590.

De Luca, F., Pensa, C., 2012. Experimental investigation on conventional and unconventional interceptors. RINA Trans. Part B Int. J. Small Craft Technol. 154, 65–72. https://doi.org/10.3940/rina.ijsct.2012.b2.129.

Karimi, M.H., Seif, M.S., Abbaspoor, M., 2013. An experimental study of interceptor's effectiveness on hydrodynamic performance of high-speed planing crafts. Polish Marit. Res. 20, 21–29. https://doi.org/10.2478/pomr-2013-0013.

Mansoori, M., Fernandes, A.C., 2017. Interceptor and trim tab combination to prevent interceptor's unfit effects. Ocean Eng. 134, 140–156. https://doi.org/10.1016/j.oceaneng.2017.02.024.

Avci, A.G., Barlas, B., 2019. An experimental investigation of interceptors for a high speed hull. Int. J. Nav. Archit. Ocean Eng. 11, 256–273. https://doi.org/10.1016/j.ijnaoe.2018.05.001.

Park, J.Y., Choi, H., Lee, J., Choi, H., Woo, J., Kim, S., Kim, D.J., Kim, S.Y., Kim, N., 2019. An experimental study on vertical motion control of a high-speed planing vessel using a controllable interceptor in waves. Ocean Eng. 173, 841–850. https://doi.org/10.1016/j.oceaneng.2019.01.019.

Seok, W., Park, S.Y., Rhee, S.H., 2020. An experimental study on the stern bottom pressure distribution of a high-speed planing vessel with and without interceptors. Int. J. Nav. Archit. Ocean Eng. 12, 691–698. https://doi.org/10.1016/j.ijnaoe.2020.08.003.

Mansoori, M., Fernandes, A.C., Ghassemi, H., 2017. Interceptor design for optimum trim control and minimum resistance of planing boats. Appl. Ocean Res. 69, 100–115. https://doi.org/10.1016/j.apor.2017.10.006.

Olin, L., Altimira, M., Danielsson, J., Rosén, A., 2016. Numerical modelling of spray sheet deflection on planing hulls. Proc. Inst. Mech. Eng. Part M J. Eng. Marit. Environ. 811–817. https://doi.org/10.1177/1475090216682838.

Molchanov, B., Lundmark, S., Fürth, M., Green, M., 2019. Experimental validation of spray deflectors for high speed craft. Ocean Eng. 191, 106482 https://doi.org/10.1016/j.oceaneng.2019.106482.

Castaldi, L., Osmak, F., Green, M., Fürth, M., Bonoli, J., 2021. The effect of spray deflection on the performance of high speed craft in calm water. Ocean Eng. 229, 108892 https://doi.org/10.1016/j.oceaneng.2021.108892.

Taunton, D.J., Hudson, D.A., Shenoi, R.A., 2010. Characteristics of a series of high speed hard chine planing hulls - Part 1: performance in calm water. Int. J. Small Craft Technol. 152, 55–75. https://doi.org/10.3940/rina.ijsct.2010.b2.96.

Cucinotta, F., Guglielmino, E., Sfravara, F., 2019. A critical CAE analysis of the bottom shape of a multi stepped air cavity planing hull. Appl. Ocean Res. 82, 130–142. https://doi.org/10.1016/j.apor.2018.11.003.

De Marco, A., Mancini, S., Miranda, S., Scognamiglio, R., Vitiello, L., 2017. Experimental and numerical hydrodynamic analysis of a stepped planing hull. Appl. Ocean Res. 64, 135–154. https://doi.org/10.1016/j.apor.2017.02.004.

Bilandi, R.N., Mancini, S., Dashtimanesh, A., Tavakoli, S., De Carlini, M., Bensow, R., Ringsberg, J., 2019. A numerical and analytical way for double-stepped planing hull in regular wave. In: Proceedings of the 8th International Conference on Computational Methods in Marine Engineering, MARINE 2019.

Bilandi, R.N., Vitiello, L., Mancini, S., Nappo, V., Roshan, F., Tavakoli, S., Dashtimanesh, A., 2020. Calm-water performance of a boat with two swept steps at high-speeds: Laboratory measurements and mathematical modeling. Procedia Manuf. 42, 467–474. https://doi.org/10.1016/j.promfg.2020.02.046.

Wielgosz, C., Fürth, M., Datla, R., Chung, U., Rosén, A., Danielsson, J., 2018. Experimental validation of numerical drag prediction of novel spray deflector design. In: Proceedings of the 13th International Marine Design Conference, pp. 491–497.

Lakatoš, M., Tabri, K., Dashtimanesh, A., Andreasson, H., Begovic, E., 2020. Numerical Modelling of a Planing Craft with a V-Shaped Spray Interceptor Arrangement in Calm Water. IOS Press, pp. 33–42. https://doi.org/10.3233/PMST200024, 12th Symp. High Speed Mar. Veh. HSMV 2020.

ITTC. (2014a). Example for Uncertainty Analysis of Resistance Tests, in: Towing Tank. In 27th International Towing Tank Conference, Recommended Procedures and Guidelines, Procedure 7.5-02-02-02.1. Retrieved from https://www.ittc.info/media/8003/75-02-02-021.pdf.

ITTC. (2014b). General Guideline for Uncertainty Analysis in Resistance Tests, In: 27th International Towing Tank Conference, Recommended Procedures and Guidelines, Procedure 7.5-02-02-02. Retrieved from https://www.ittc.info/media/8007/75-02-02-02.pdf.

ITTC. (2017a). Resistance Test, In: 28th International Towing Tank Conference, Recommended Procedures and Guidelines, Procedure 7.5-02-02-01. Retrieved from https://www.ittc.info/media/8001/75-02-02-01.pdf.

ITTC. (2017b). Uncertainty Analysis Instrument Calibration, In: 28th International Towing Tank Conference, Recommended Procedures and Guidelines, Procedure 7.5-01-03-01. Retrieved from https://www.ittc.info/media/7979/75-01-03-01.pdf.

Larsson, L., Eliasson, R.E., Orych, M., 2014. Principles of Yacht Design, 4th Revise. Adlard Coles Nautical.

Müller-Graf, B., Holden, K.O., Faltinsen, O.M., Moan, T., 1991. The Effect of an Advanced Spray Rail System on Resistance and Development of Spray of Semi-Displacement Round Bilge Hulls. Tapir Publishers, Trondheim, Norway, pp. 125–141. FAST '91, 1st Intl Conf Fast Sea Transp.

Wagner, H., 1932. Über Stoß- und gleitvorgänge an der oberfläche von flüssigkeiten. ZAMM J. Appl. Math. Mech. 12, 193–215. https://doi.org/10.1002/zamm.19320120402. Zeitschrift Für Angew. Math. Und Mech.

Appendix 3

Publication P3

Lakatoš, M., Mancini, S., Niazmand Bilandi, R., & Tabri, K. (2025). Verification and validation of hard-chine hull performance in calm water: Effects of numerical setups and hull configurations. *Ocean Engineering*, *329*, 121056. https://doi.org/10.1016/j.oceaneng.2025.121056

Ocean Engineering 329 (2025) 121056

Contents lists available at ScienceDirect

Ocean Engineering

journal homepage: www.elsevier.com/locate/oceaneng

Research paper

Verification and validation of hard-chine hull performance in calm water: Effects of numerical setups and hull configurations

Mikloš Lakatoš [a,*], Simone Mancini [b,c], Rasul Niazmand Bilandi [c], Kristjan Tabri [a]

[a] Department of Civil Engineering and Architecture, Tallinn University of Technology, Tallinn, Estonia
[b] Department of Industrial Engineering, University of Naples "Federico II", Naples, Italy
[c] Hydro & Aerodynamics Department, FORCE Technology, Kgs. Lyngby, Denmark

ARTICLE INFO

Keywords:
Planing hull
Spray rails
Chine strips
CFD
Model tests data

ABSTRACT

Recent studies show that the numerical estimations of resistance of planing hulls differ from experimental results by 10 %–20 %, mainly due to the absence of a towing force in the conventional 2DOF numerical model and the geometric differences between the 3D model in the simulations and the physical model in experiments.

This study investigates the effect of a towing force on the performance of a conventional 2DOF setup with overset grid, and compares it with a 3DOF setup, typically used for manoeuvring simulations. Additionally, different wall treatment approaches ($y+ < 5$ and $y+ > 30$) are compared. Verification and validation analysis is conducted for the bare hull and the validated numerical models are used to compare hulls equipped with spray rails, chine strips and V-shaped spray interceptors.

Models directly solving the viscous sub-layer ($y+ < 5$) were invalidated since their comparison errors in running position and resistance exceeded the validation uncertainty. Conversely, numerical models employing wall functions for wall treatment ($y+ > 30$) accurately predicted both the running position and the resistance of the bare hull within the validation uncertainty. Introducing a towing force in the 2DOF model improved the prediction of the running position, while the 3DOF setup demonstrated better overall accuracy.

Nomenclature

b	Wetted half-width (m)	β_T	Deadrise angle at the transom (deg)
b_1	Actual wetted half-width (m)	$\beta_{0.5}$	Deadrise angle at 50 % L_{DWL} (deg)
b_{SR}	Width of the spray rail (m)	$\beta_{0.75}$	Deadrise angle at 75 % L_{DWL} (deg)
b_{CS}	Width of the chine strip (m)	δ	Bottom angle of the spray rail (deg)
			the thickness of the spray sheet (m)
B_{CT}	Chine beam at the transom	δ_{SM}	Modelling error
B_{OA}	Beam overall (m)	δ_{SN}	Simulation error
B_{WL}	Beam waterline (m)	Δt	Time step (s)
BS	Base Size (m)	Δx	Cell size (m)
d	Parallel normal distance from stagnation line to VSI (m)	ε	Solution change
Fr	Froude number (−)	τ	Dynamic trim (deg)
Fr_∇	Froude displacement number (−)	∇	Displacement Volume (m^3)

(*continued on next column*)

(*continued*)

E	Comparison error (%)	Ⓜ	Length-displacement ratio $\frac{L_{WL}}{\sqrt[3]{\nabla}}$
KG	Vertical Centre of Gravity (m)	BH	Bare Hull
L_{CG}	Longitudinal Centre of Gravity (m)	CFD	Computational Fluid Dynamics
L_{OA}	Length overall (m)	CFL	Courant-Friedrichs-Lewy number
L_{PP}	Length between perpendiculars (m)	CF	Correction Factor method
L_{WL}	Length waterline (m)	CG	Centre of Gravity
p_k	Estimated order of accuracy (−)	C. INC	Chine inclination
p_{kth}	Theoretical order of accuracy (−)	Con	Conventional spray rail profile
R_k	Convergence ratio (−)	CSR	Chine spray rail
R_{TM}	Total resistance in model scale (N)	CSI	Chine spray interceptor
S_{WB}	Wetted bottom area, underway (m^2)	DFBI	Dynamic Fluid Body Interaction
S_{WHE}	Wetted hull area, underway (m^2)	EFD	Experimental Fluid Dynamics

(*continued on next page*)

* Corresponding author.
E-mail address: miklos.lakatos@taltech.ee (M. Lakatoš).

https://doi.org/10.1016/j.oceaneng.2025.121056
Received 16 January 2025; Received in revised form 4 March 2025; Accepted 22 March 2025
Available online 11 April 2025
0029-8018/© 2025 The Authors. Published by Elsevier Ltd. This is an open access article under the CC BY-NC license (http://creativecommons.org/licenses/by-nc/4.0/).

(*continued*)

S_{WS}	Area wetted by Spray (m^2)	GCI	Grid Convergence Index Method
S_U	Maximum value for simulation result	HRIC	High-Resolution Interface Capturing
S_L	Minimum value for simulation result	LSR	Least Squares Root
T	Draught (m)	MMP	Mixture Multiphase
U	Uncertainty	NV	Numerical Ventilation
U_{SN}	Simulation uncertainty	PMM	Planar Motion Mechanism
U_D	Experimental data uncertainty	RE	Richardson Extrapolation
U_V	Validation uncertainty	Rec	Rectangular Spray rail profile
U_G	Grid uncertainty	SR	Spray rail arrangement
U_I	Iteration uncertainty	Tri	Triangular Spray Rail profile
U_{TS}	Time-step uncertainty	VOF	Volume of Fluid
V_{Hull}	Hull velocity (m/s)	VSI	V-Shaped Spray Interceptor
z_{VCG}	Dynamic sinkage at CG (m)	V&V	Verification and Validation

1. Introduction

Hard-chine hulls, widely used in high-speed marine vessels, are favoured for their efficiency and manoeuvrability but come with distinctive hydrodynamic challenges. To optimize their performance—especially considering resistance, stability, and spray control—designers often incorporate features such as steps, tunnels, spray rails, chine strips, and V-shaped interceptors. Many of these elements can be retrofitted after manufacturing, allowing for performance enhancements even in existing hulls. These modifications are particularly beneficial in calm water and moderate wave conditions, where they help reduce drag, increase lift, and improve overall efficiency. Of particular importance is drag reduction, as it directly affects speed and fuel efficiency. The total resistance of a high-speed craft (HSC) comprises various components, including induced drag, appendage resistance, frictional resistance, aerodynamic resistance, and spray resistance (Larsson and Raven, 2010). Notably, spray resistance alone can contribute over 15 % of total resistance at planing speeds (Müller-Graf, 1991; Savitsky et al., 2007), underscoring the significance of controlling and minimizing this resistance for planing hulls.

To assess the hydrodynamic impact of these modifications, researchers employ three primary methods: towing tank experiments, mathematical modelling, and numerical simulations. Each approach offers unique insights, and together they facilitate a comprehensive understanding of how retrofitted features influence high-speed hull performance.

Traditionally, towing tank experiments have been fundamental to planing hull research, especially for retrofitting purposes, as they provide highly accurate data on physical interactions, resistance, and trim measurements. Numerous studies have examined hull modifications using experimental towing tank tests to validate performance improvements. For instance, some researchers have retrofitted hulls with spray rails, chine strips, and spray deflectors, aiming to minimize resistance. Clement (1964a, 1964b) investigated the effects of longitudinal spray strips extending 70 % aft from the bow, finding they reduced resistance at high speeds but increased it at low speeds. Additionally, he observed that sharper edges on the strips yielded better performance, while strips positioned only forward of the high-speed stagnation line achieved a 6 % resistance reduction at high speeds without impacting resistance at low speeds.

More recently, Molchanov et al. (2019) conducted towing tank tests comparing the effects of spray rails and spray deflectors in calm water and irregular waves. Although results are most applicable to the specific hull shapes tested, they also provide insights for other prismatic and warped hull forms. Their findings showed that spray rails reduced drag by up to 9 % and primarily influenced heave motion, while deflectors achieved even higher drag reductions of 10–25 % but significantly altered the hull's dynamic trim. Lakatoš et al. (2022) tested a low-planing craft (Fr_∇ = 1.742–3.261) equipped with various spray rails, chine strips, and a V-shaped spray interceptor (VSI). At planing speeds ($Fr_\nabla > 3$), spray rails reduced resistance by up to 2.4 % with minimal effect on trim. Narrow, sharp-angled spray rails were as effective, or even more so, than wider, horizontal rails, while overly long rails contributed to increased resistance. The VSI, positioned ahead of the stagnation line, helped deflect spray and lowered resistance by up to 4.2 %. Conversely, when placed behind the stagnation line, it led to an 8.4 % increase in resistance.

Testing high-speed planing hulls in towing tanks also introduces the challenge of replicating real-world hull geometry accurately, as minor modifications—like the addition of steps—can drastically influence hydrodynamic lift, drag, and stability. Taunton et al. (2010) tested four deep-vee monohulls with one or two steps in various positions and observed that adding steps to a stepless hull resulted in significant resistance reduction, with decreases of 26.5 % and 25.4 % for single- and double-stepped hulls, respectively, at maximum speed. Lee et al. (2014) explored the calm-water performance of two-stepped configurations on the NSWC15E hull, varying step positions and heights. They discovered that all double-stepped configurations offered lower resistance than the non-stepped design at planing speeds, with optimal resistance reduction achieved using a front step height of 0.7 % of the beam and a rear step height of 2.1 % of the beam. Further studies by Vitiello et al. (2022) highlighted that the number, position, and height of forward swept steps significantly affect hull performance, with optimized designs reducing drag and improving dynamic stability at high speeds. This foundational experimental work informs the development of mathematical and numerical models, which aim to replicate and refine these physical findings under varied operating conditions.

In addition to physical experiments, mathematical models present a less resource-intensive alternative, providing predictive equations to estimate parameters like resistance, trim, and stability. These models are grounded in principles of fluid mechanics and empirical data, making them particularly useful for initial design assessments. The Savitsky method (Savitsky, 1964) stands out as one of the most renowned mathematical approaches for the hydrodynamic design of planing hulls, relying on analytical and semi-empirical equations. Since its inception, researchers have widely adopted the Savitsky model to develop mathematical frameworks for assessing hull performance under various conditions. Building on this foundational work, Savitsky et al. (2007) introduced an important extension, focusing on the whisker spray drag—an additional viscous drag component in the spray area ahead of the stagnation line. This study provided a detailed method to quantify the whisker spray drag based on parameters such as deadrise angle, trim angle, and speed, filling a gap left by the original 1964 model. The findings highlighted that whisker spray drag could constitute up to 15 % of the total resistance at high planing speeds, underscoring the importance of precise spray resistance calculations for performance prediction.

Further advancements were made by Savitsky and Morabito (2010), who conducted wave profile tests on planing hulls to derive equations that describe the water surface profile behind hull steps, a modification not included in earlier models. This effort was motivated by the need to account for the hydrodynamic impact of hull steps, which are commonly added to enhance planing efficiency. Recognizing the influence of these steps, some researchers combined 2D + t theory with Savitsky's formulations to assess stepped hulls in calm water, advancing the mathematical modelling landscape for hull configurations. The first dedicated mathematical model for stepped hulls was developed by Niazmand Bilandi et al. (2019), which successfully predicted the hydrodynamic behaviour of a two-stepped hull with straight steps. Niazmand Bilandi et al. (2020) further refined this model in 2020, introducing the ability to simulate asymmetric motion in double-stepped planing boats. These contributions underscore the potential of Savitsky's 1964 formulations and their combinations with additional modifications in refining

performance predictions. However, developing mathematical models to account for the effects of spray rails, chine strips, and other retrofitting elements remains an area for future study.

While mathematical models provide significant insight, they often rely on simplifying assumptions that limit their applicability to more intricate or unconventional hull shapes. Retrofitting, involving the addition of elements like spray rails and interceptors to existing hulls, remains challenging to predict through mathematical models alone due to the substantial changes these elements introduce to hull dynamics.

Numerical simulations using Computational Fluid Dynamics (CFD) have become a powerful tool to bridge the gap between the precision of towing tank experiments and the simplicity of mathematical models. CFD enables detailed analysis of parameters like pressure distribution, shear stress, and wetted surface area—quantities often challenging to capture experimentally (Niazmand Bilandi et al., 2023; Roshan et al., 2020). Additionally, it allows flexible testing of various configurations, including retrofitted hulls, significantly reducing both time and cost compared to physical experiments. However, the accuracy of CFD for planing hulls can vary. Recent studies report that CFD simulations underestimate resistance by 10–20 % relative to towing tank data (Cui et al., 2021; Tavakoli et al., 2024), with discrepancies often arising from idealized geometries (Judge et al., 2020), uncertainties in model ballasting, and the lack of a towing force's trimming effect (De Luca et al., 2014). Table A. 1 displays a summary of numerical setups in recent CFD studies on calm water performance of planing hulls.

Simulating the complex hydrodynamic environment of planing hulls introduces further computational challenges. First, the high velocities associated with planing generate turbulent flows that require advanced turbulence models. Popular options, such as k-ω SST and DES models, each come with trade-offs: k-ω SST provides stability in boundary layer regions, while DES models capture large eddies behind the transom, which are essential for accurate drag prediction (De Marco et al., 2017). Additionally, numerical ventilation, or air entrainment in high-speed flows, can distort resistance values and is particularly sensitive to mesh configurations. Achieving adequate resolution near hull surfaces often requires tailored wall treatments — either refined wall models ($y+ < 5$) or wall functions ($y+ > 30$), each balancing accuracy with computational cost. Recent findings by Niazmand Bilandi et al. (2024a) suggest that at very high speeds, using $y+ > 30$, the k-ω SST model outperforms k-ε in terms of lower error, while for $y+ < 5$, k-ε offers lower error in resistance prediction with overset techniques. Overall, both models are widely adopted in recent hydrodynamics projects, with k-ω SST emerging as the most popular option, as shown by Terziev et al. (2020). Finally, mesh motion techniques, such as morphing or overset grids, must accommodate significant hull movements during planing, further complicating the setup. Niazmand Bilandi et al. (2024b) demonstrated that the overset technique is highly effective in validating complex planing hull simulations.

The present study aims to address these challenges by conducting simulations to examine the hydrodynamic effects of spray rails, chine strips, and V-shaped interceptors on hard-chine hulls in calm water. Specifically, this research aims to.

- Compare wall-treatment approaches by implementing $y+<5$ and $y+>30$ configurations to evaluate their influence on numerical accuracy.
- Compare the accuracy 2DOF model with and without an applied trimming moment from the towing force to that of a 3DOF setup.
- Analyse uncertainties in model ballasting and towing point placement using quasi-static simulations.
- Evaluate the effects of geometry differences by simulating sharp and rounded hull edges under design conditions.
- Assess the ability numerical simulations to predict the effect of different appendages on the performance of planing hull.

The structure of this article is outlined in Fig. 1 to guide the reader through the study's key components. Ch. 1 provides an overview of spray rail, chine strip, and interceptor designs. Ch. 2 presents an overview of the experimental data used for the verification and validation of numerical models. Ch. 3 gives a detailed account of the numerical setups, including the computational domain, boundary conditions, and numerical models. Ch. 4 details the verification and validation methodology. Ch. 5 is divided into two sections: Sec. 5.1 presents the results of the verification and validation process, while Sec. 5.2 discusses the simulation results for spray rails, chine strips, and V-shaped spray interceptors, comparing numerical predictions with experimental data. Finally, Ch. 6 summarizes the key findings and conclusions of the study.

2. Experimental reference data (MARTE spray rail test series)

The numerical approaches proposed in this study are validated against model test results from an experimental study (Lakatoš et al., 2022) of a planing hull equipped with spray rails and chine strips. The test case vessel (Fig. 2), designed by the Marine Technology Competence Centre (MARTE) of Tallinn University of Technology (TalTech), was used to compare conventional and novel spray rail configurations

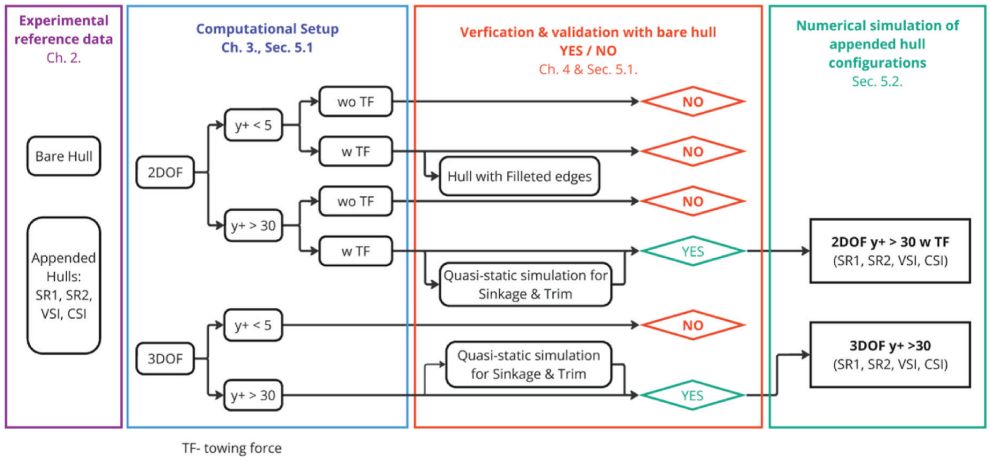

Fig. 1. Outline and numerical models used in the investigation.

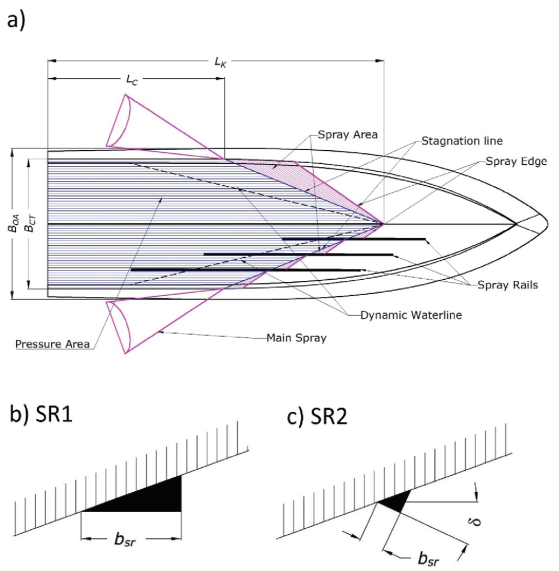

Fig. 2. a) Planing hull with and without spray rails, b) conventional 8 × 3 mm spray rail SR1, c) triangular 2 × 2 mm spray rail SR2.

(Lakatoš et al., 2022). The calm water resistance tests were conducted in the towing tank (see Table B. 1) of MARTE following the ITTC guidline 7.5-02-02-01 (ITTC, 2017b). The hull dimensions (Table 1) are representative of a high-speed patrol, Search-And-Rescue (SAR) vessel, or a large pleasure boat, designed for operation at a Froude number of $Fr = 1.355$ and a volumetric Froude number of $Fr_\nabla = 3.108$, corresponding to a displacement of 40 t and a speed of 35 knots. The experimental study tested the bare hull with various configurations, including spray rails, chine strips, and V-shaped spray interceptors (VSI) in a speed range of $Fr_\nabla = 1.742 - 3.261$.

The numerical model was validated using the bare hull experimental results. CFD predictions were then compared with experimental data using a selection of previously tested hulls equipped with conventional spray rails (Fig. 2), chine strips (Fig. 3) and VSI (Fig. 4), all under design conditions, $Fr = 1.355$ and $Fr_\nabla = 3.108$. The dimensions of these appendages are presented in Table 2. Fig. 5 displays the spray formation on the model SR2 under experimental conditions.

Table 1
Main Dimensions of the test case hull.

Parameter		Model	Full-scale
Scale factor	λ	10	1
Length overall	L_{OA}	1.921 m	19.210 m
Length between perpendiculars	L_{PP}	1.800 m	18.000 m
Length waterline	L_{WL}	1.703 m	17.030 m
Beam overall	B_{OA}	0.581 m	5.810 m
Beam waterline	B_{WL}	0.581 m	5.810 m
Draught	T	0.108 m	1.080 m
Displacement mass	Δ_m	40 kg	40 t
Displacement volume	∇	0.040 m3	40.00 m3
Longitudinal Centre of Gravity	L_{CG}	0.669 m	6.690 m
Vertical Centre of Gravity	KG	0.200 m	2.00 m
Length beam ratio	L_{WL}/B_{WL}	3.338	3.338
Beam draught ratio	B_{WL}/T	4.737	4.737
Length-displacement ratio	$L_{WL}/\nabla^{1/3}$	4.978	4.978
Horizontal position of the towing point (from transom)	TPH	0.36 m	N.A.
Vertical position of the towing point (from keel)	TPV	0.09 m	N.A.

3. Computational setup

The hydrodynamics of planing hulls were modelled using Siemens PLM STAR-CCM+ 2210 Build 17.06.007 (SIEMENS PLM, 2022). An implicit unsteady solver was chosen to implement the Reynolds-Averaged Navier-Stokes (RANS) equations, coupled with the Realizable k-ε turbulence model for turbulence prediction. The Volume of Fluid (VOF) approach with the High-Resolution Interface Capturing (HRIC) scheme was employed to track the free surface between air and water, and the Dynamic Fluid-Body Interaction (DFBI) model enabled analysis of hull motions in pitch and heave. This setup was supported by the overset grid technique, a reliable method for high-speed hull simulations that efficiently handles complex hull movements and reduces grid deformation errors (De Luca et al., 2016; Niazmand Bilandi et al., 2023, 2024a). Table 3 provides a comprehensive overview of the solver settings employed, including the time step, turbulence model, wall treatment, and other critical parameters necessary for the hydrodynamic simulations.

3.1. Governing equations

The fundamental RANS and continuity equations form the core of the numerical model. For incompressible flow, the RANS equations are expressed as:

$$\frac{\partial u_i}{\partial t} + u_j\frac{\partial u_i}{\partial x_j} = -\frac{1}{\rho}\frac{\partial p}{\partial x_i} + \vartheta\frac{\partial^2 u_i}{\partial x_j^2} - \frac{\partial}{\partial x_j}\left(u_i' u_j'\right) \tag{1}$$

where u_i and u_j are the velocity components, p is the pressure, ρ is the fluid density, ϑ is the kinematic viscosity, and $u_i' u_j'$ are the Reynolds stresses, which are modelled by the Realizable $k - \epsilon$ turbulence model. The continuity equation for incompressible flow is:

$$\frac{\partial u_i}{\partial x_i} = 0. \tag{2}$$

The VOF method, used to capture the air-water interface, solves a volume fraction transport equation. This equation ensures that the two phases (air and water) are correctly captured within each cell of the computational domain, maintaining a sharp interface:

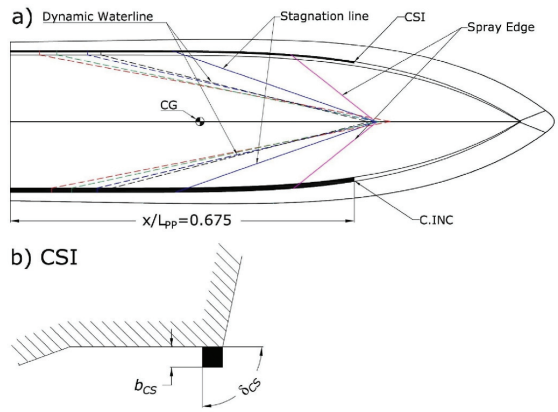

Fig. 3. Chine strips: a) Position of the chine strips, b) Cross-section of the chine strip (CSI).

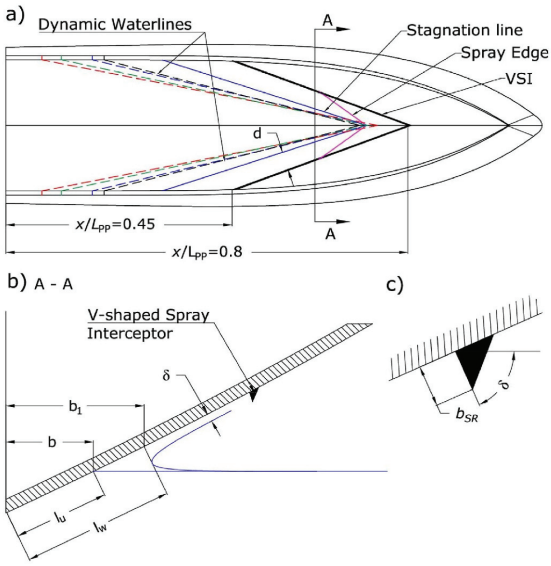

Fig. 4. V-shaped spray interceptors: a) layout, b) cross-section of the hull and dimensions of the spray sheet at $x/L_{WL} = 0.65$, c) Profile of the VSI at $x/L_{WL} = 0.65$.

$$\frac{\partial \alpha}{\partial t} + \nabla.(\alpha \mathbf{u}) + \nabla.\Big(\alpha(1-\alpha)\mathbf{u_r} = 0, \tag{3}$$

where α represents the volume fraction of water (with air being $1-\alpha$), and $\mathbf{u_r}$ is the relative velocity at the interface.

3.2. Turbulence model and wall treatment

The Realizable $k-\varepsilon$ model, known for its stability and robustness, was selected for all simulations, ensuring accurate predictions in high-speed flows (Niazmand Bilandi et al., 2024a). The two-layer. All y + wall treatment was applied to maintain consistent near-wall treatment across the hull. This treatment adapts between low-y + treatment ($y+ < 5$) for fine grids and high-y + treatment ($y+ > 30$) for coarser grids (ITTC 7.5-03-02-03 Rev 01, 2017a). Prism layers were applied with constant thickness near the hull to ensure accurate boundary layer representation. Two configurations of prism layers were used: 8 layers for $y^+ \cong 70$ and 15 layers for $y^+ \cong 3$ (see Fig. 6).

3.3. Time step control and CFL condition

The time step Δt was carefully controlled to maintain stability by following the Courant-Friedrichs-Lewy (CFL) condition:

$$\Delta t = \frac{CFL \bullet \Delta x}{V_{Hull}} = \frac{0.25 \bullet BS}{V_{Hull}} = \frac{0.008 \bullet L_{pp}}{V_{Hull}} \tag{4}$$

Where Δx is the cell size, set to 25 % of the base size in the first level of refinement in the overset region, BS is the base size (0.06 m), V_{Hull} is the hull velocity, and L_{pp} the length of the hull between perpendiculars. The time step was carefully selected to adhere to the International Towing Tank Conference (ITTC) guideline 7.5-03-02-03 Rev 01 (ITTC, 2017a) within the range of $\Delta t < 0.01\ L_{pp}/V_{Hull}$ across all Froude numbers in the study.

3.4. Numerical ventilation (NV) mitigation

Numerical ventilation (NV) is a recognized challenge in CFD simulations for planing hulls, often resulting from interface smearing in the Volume of Fluid (VOF) approach. This smearing can cause air entrainment in boundary layer cells, leading to inaccuracies in predicting frictional resistance and pressure distribution (De Luca et al., 2016; Gray-Stephens et al., 2019; Mancini et al., 2017). To address NV, a multi-faceted approach was adopted: mesh refinement was applied to critical regions like the bow and the upstream free surface to improve interface accuracy while adjustments in the prism layer alignment and cell sizing further sharpened the interface. High-Resolution Interface Capture (HRIC) was also utilized to enhance the representation of the air-water interface (Gray-Stephens et al., 2019). Additionally, artificial suppression methods were implemented by introducing source terms in cells adjacent to the hull boundary to replace entrapped air with water, minimizing ventilation effects (Viola et al., 2012). Wheeler et al. (2021) also suggested an alternative Slip Velocity approach, which enhances the VOF model by introducing slip velocity, effectively aligning VOF behaviour with that of the Mixture Multiphase (MMP) model and thereby achieving a sharper phase separation (SIEMENS PLM, 2022). Fig. 7 displays the air volume fraction across the hull surface, indicating minimal ventilation of the hull's wetted area at various simulated speeds. This confirms effective mitigation strategies, with negligible air entrainment impacting the accuracy of resistance and pressure predictions.

3.5. Towing force application and degrees of freedom (DOF)

The towing force T was applied at the same location as in model tests, positioned at *TPH* from the transom and at *TPV* from the baseline (see Table 1). Its magnitude was determined based on average resistance, with:

$$T = R_{TM}\cos(\tau), \tag{5}$$

Where R_{TM} is the model-scale resistance, and τ is the trim angle.

A three-degrees-of-freedom (3DOF) approach was used in the simulations, allowing heave, pitch, and surge motions to be considered. Unlike traditional 2DOF setups, this 3DOF approach considers a stationary water domain with an advancing hull, simplifying velocity prescription by avoiding challenges with progressive speed changes that can cause mass accumulation and wave generation (Wheeler et al., 2021).

3.6. Mesh configuration and Adaptive Mesh Refinement (AMR)

The computational domain (Fig. 8) was structured with hexahedral control volumes, incorporating prism layers near the hull to capture boundary layer effects accurately. The dimensions of the domain were

Table 2
Dimensions of the tested spray rails and chine strips.

Hull configuration	Description	b_{SR} [mm]	b_{SR}/L_{DWL}	δ [deg]	b_{CS} [mm]	b_{CS}/L_{DWL}	δ_{CS} [deg]	β' [deg]	EFD
BH	Bare hull								Yes
CSI	Bare hull with rectangular chine strip				2	0.1 %	−90	18.4	Yes
SR1	Conventional spray rails	7	0.5 %	0					Yes
SR2	Triangular 2 × 2mm spray rails	2	0.1 %	−25					Yes
VSI	V-shaped spray interceptor	5	0.3 %	−66					Yes

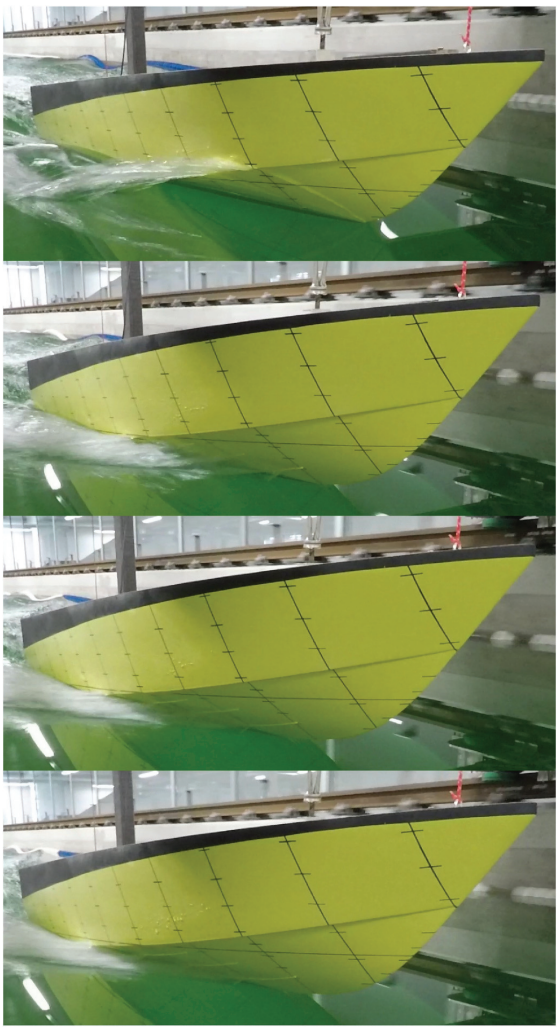

Fig. 5. Spray formation on the model SR2 at $Fr_{\nabla} = 1.776, 2.220, 2.664, 3.108$.

selected following the ITTC guideline 7.5-03-02-03 Rev 01 and recent studies (ITTC, 2017a; Niazmand Bilandi et al., 2024a; Wheeler et al., 2021). It was divided into two regions: a stationary far-field region with velocity inlet, pressure outlet, and symmetry boundaries, and a moving overset region, which includes wall, symmetry, and overset boundaries. The interpolation scheme between background and overset regions is the linear one, as suggested for similar applications by De Luca et al. (2016). Wave-forcing was applied at the inlet, outlet, and side boundaries, with a wave-forcing length of $2.5L_{PP}$, to prevent wave reflection and contain the domain dimensions (Lee et al., 2019; SIEMENS PLM, 2022; Wheeler et al., 2021).

Adaptive Mesh Refinement (AMR) was dynamically implemented, refining cells in two critical areas: overset AMR, ensuring accurate refinement around the vessel without over-refining the background mesh, and free surface AMR, refining cells near the water surface to capture wake waves precisely. This approach allowed the background mesh to be refined only in necessary locations, adapting dynamically as the hull moved, thereby optimizing computational efficiency. The AMR methodology reduced the overall mesh count and computational cost

Table 3
Solver settings for the planing hull CFD simulation.

Item	2DOF y+ < 5	2DOF y+ > 30	3DOF y+ < 5	3DOF y+ > 30
DOF	2DOF	2DOF	3DOF	3DOF
Convection Term	2nd order	2nd order	2nd order	2nd order
Temporal Discretization	1st order	1st order	1st order	1st order
Time-step [s]	Function of velocity and mesh size	Function of velocity and mesh size	Function of velocity and mesh size	Function of velocity and mesh size
Inner iterations per time step	5	5	5	5
Turbulence model	Realizable k-ε	Realizable k-ε	Realizable k-ε	Realizable k-ε
Overset interpolation scheme	Linear	Linear	Linear	Linear
Iterations of 6-DOF solver per inner iteration	3	3	3	3
Wall treatment	Two-Layer All y+	Two-Layer All y+	Two-Layer All y+	Two-Layer All y+
Number of prism layers	15	8	15	8
Prism Layer Thickness	0.012 m	0.012 m	0.012 m	0.012 m
NV treatment	Air Suction	Air Suction	Air Suction	Slip velocity
AMR	No	No	Yes	Yes
DFBI	Free motion	Free motion	General Planar motion	General Planar motion
DOF	Pitch and heave	Pitch and heave	Surge, Pitch, and heave	Surge, Pitch, and heave

while achieving high accuracy in essential flow regions. The resulting domain mesh is depicted in Figs. 9 and 10.

4. Numerical verification and validation: introduction

Verification evaluates simulation uncertainty (U_{SN}) caused by numerical errors from iterative methods and parameter specifications (e.g., spatial and temporal discretization) (Stern et al., 2001). Simulation error (δ_{SN}) and uncertainty (U_{SN}) are divided into components for iteration (δ_I), grid (δ_G), timestep (δ_{TS}) and other parameters (δ_P):

$$\delta_{SN} = \delta_I + \delta_G + \delta_{TS} + \delta_P \tag{6}$$

$$U_{SN}^2 = U_I^2 + U_G^2 + U_{TS}^2 + U_P^2 \tag{7}$$

Grid uncertainty is often the main source of uncertainty (De Luca et al., 2016; Wilson et al., 2006), approximating simulation uncertainty:

$$U_G^2 \approx U_{SN}^2 \tag{8}$$

To estimate grid uncertainty, at least three different grids (fine, medium, and coarse) must be created. Methods such as the Correction Factor (CF) or Grid Convergence Index (GCI) (Celik et al., 2008) assess convergence by evaluating the convergence ratio (R_G) through solution changes (ε) across different grid levels:

$$\varepsilon_{21} = S_2 - S_1, \varepsilon_{32} = S_3 - S_2, R_G = \varepsilon_{21}/\varepsilon_{32} \tag{9}$$

Convergence types (ITTC 7.5-03-01-01 Rev. 04, 2021; Stern et al., 2006) include monotonic ($0 < R_G < 1$) or oscillatory convergence ($R_G < 0, |R_G| < 1$) and divergence ($R_G > 1$ or $R_G < 0, |R_G| > 1$). However, for the monotonic convergence only, the grid uncertainty (U_G) and accuracy order (p_G) can be evaluated and are calculated based on the following formulas:

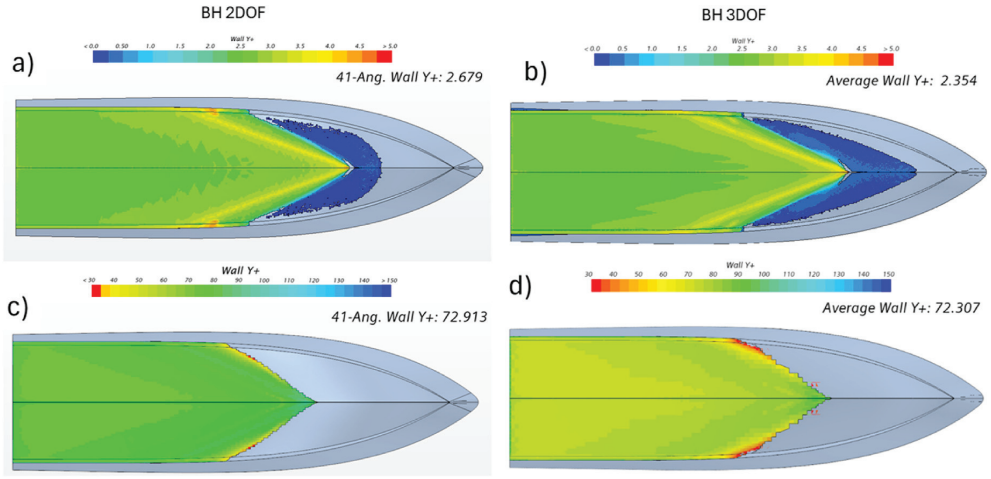

Fig. 6. Wall y + Distribution — The upper region (a, b) shows y + values below 5, indicating a fine mesh near the wall, while the lower region (c, d) exhibits y + values above 30, suggesting a coarser boundary layer resolution.

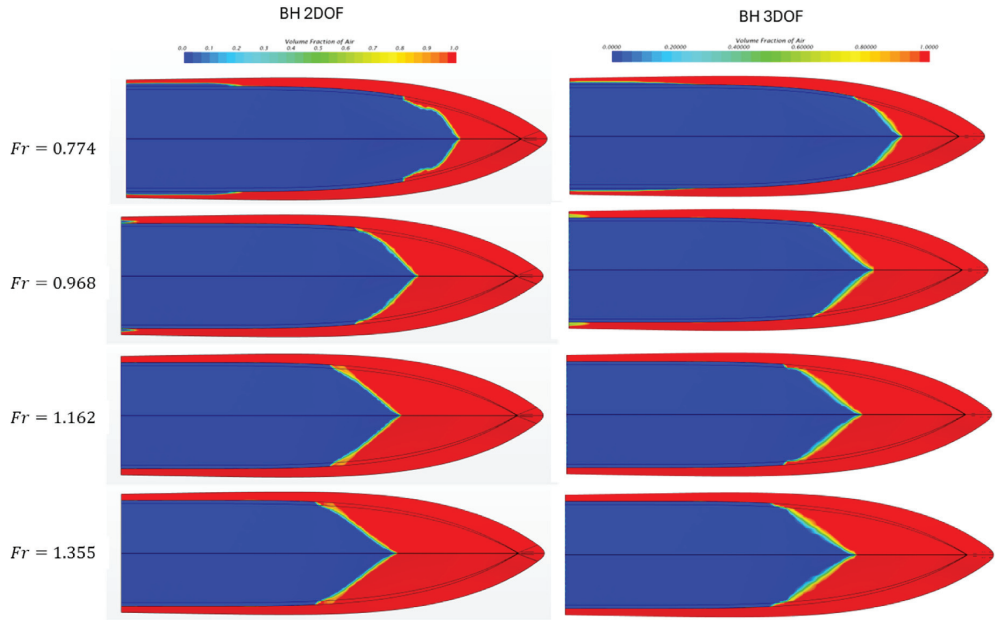

Fig. 7. Air volume fraction on the hull surface, showing minimal ventilation across all simulated speeds.

$$p_G = \frac{ln\left(\frac{\varepsilon_{32}}{\varepsilon_{21}}\right)}{ln(r_G)} \tag{10}$$

$$U_G = F_S \delta_{RE}, \text{where } \delta_{RE} = \frac{\varepsilon_{21}}{r_G^{p_G} - 1} \tag{11}$$

Where r_G is the grid refinement ratio, assumed to be constant over the generated grids.

Another method, such as the GCI-LSR method (Eça and Hoekstra, 2014) can overcome the limitation of the monotonic convergence required through Least Squares Root (LSR) minimization:

$$S_{RE}(S_0, q, p_G) = \sqrt{\sum_i^{n_g} \left(S_i - (S_0 + q r_G^{p_G})\right)^2} \tag{12}$$

$$U_S = \sqrt{\frac{\sum_i^{n_g} \left(S_i - (S_0 + q r_G^{p_G})\right)^2}{n_g - 3}} \tag{13}$$

Validation compares simulation results (S) with experimental data (D) to quantify modelling uncertainty (U_{SM}) and error (E):

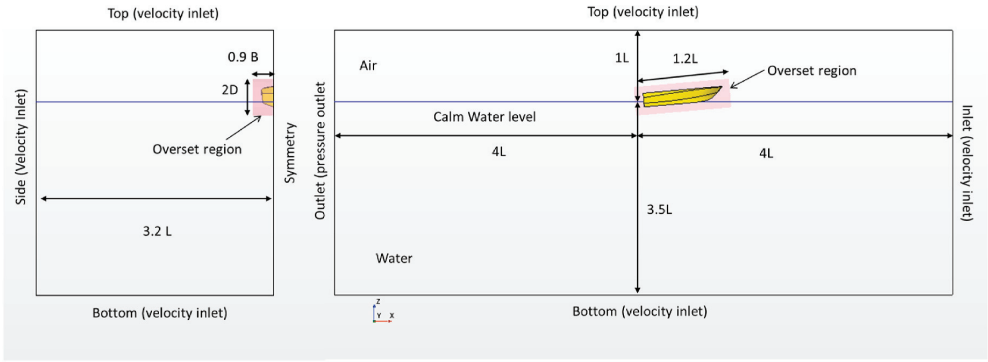

Fig. 8. The computational domain and boundary conditions for the planing hull simulation. The stationary far-field region, outlined by a rectangular black line, includes velocity inlet, pressure outlet, and symmetry boundaries. The moving overset region, filled with pink, surrounds the hull and features wall, symmetry, and overset boundaries to capture hull dynamics effectively. (For interpretation of the references to colour in this figure legend, the reader is referred to the Web version of this article.)

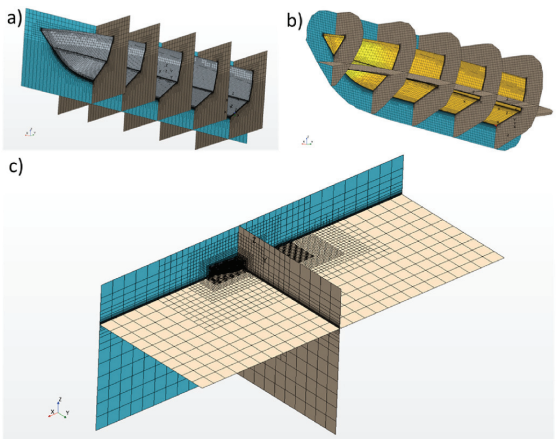

Fig. 9. Domain mesh configuration: (a, b) Overset region mesh surrounding the hull, designed to move with the vessel and capture fine flow details, and (c) far-field region mesh, which remains stationary to simulate ambient flow conditions efficiently.

$$E = D - S = \delta_D - (\delta_{SM} + \delta_{SN}) \tag{14}$$

$$U_V^2 = U_D^2 + U_{SN}^2 \tag{15}$$

Validation succeeds if $|E| \leq U_V$, otherwise, models or data accuracy needs improvement. Detailed methods are discussed in Eça and Hoekstra (2006), and Niazmand Bilandi et al. (2024a).

5. Results & discussions

5.1. Verification and validation on the bare hull

In this section, the verification and validation analysis of the bare hull case is presented. As specified Sec 3, various setup configurations were examined and compared, as well as different sources of numerical uncertainty that were investigated to determine potential strategies for reducing simulation uncertainty. The results of all simulations, including resistance, dynamic trim, and sinkage, are shown in Fig. 11. Further details on the impact of the different setup configurations and

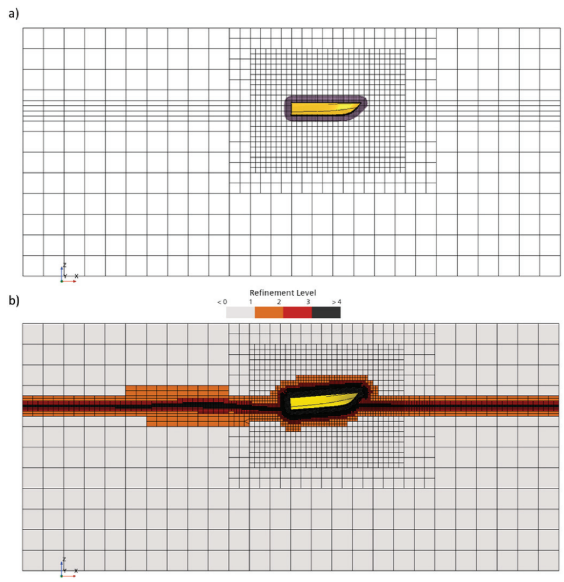

Fig. 10. Computational domain of the 3DOF numerical model before (a) and after (b) the activation of the AMR.

sources of error/uncertainty are discussed in the following subsections.

5.1.1. Influence of wall treatment

As mentioned above, the verification analysis was performed following the GCI, CF, and GCI-LSR approaches. Four different grid structures have been generated with a grid refinement ratio equal to $\sqrt{2}$ around the hull (Wilson et al., 2004, 2006). The four generated meshes are referred to as A (coarse), B (medium), C (fine), and D (very fine). The properties of the meshes used for the verification analysis of the four numerical setups are presented in Tables C. 1 to C. 8. Fig. 11 displays the comparison of resistance, sinkage, and trim obtained from the 2DOF and 3DOF models using $y+ < 5$ and $y+ > 30$ wall treatment approaches.

The influence of the wall treatment approach can be assessed by observing the results of simulations using the various near-wall resolutions and approaches. Specifically, the model that directly solved for the

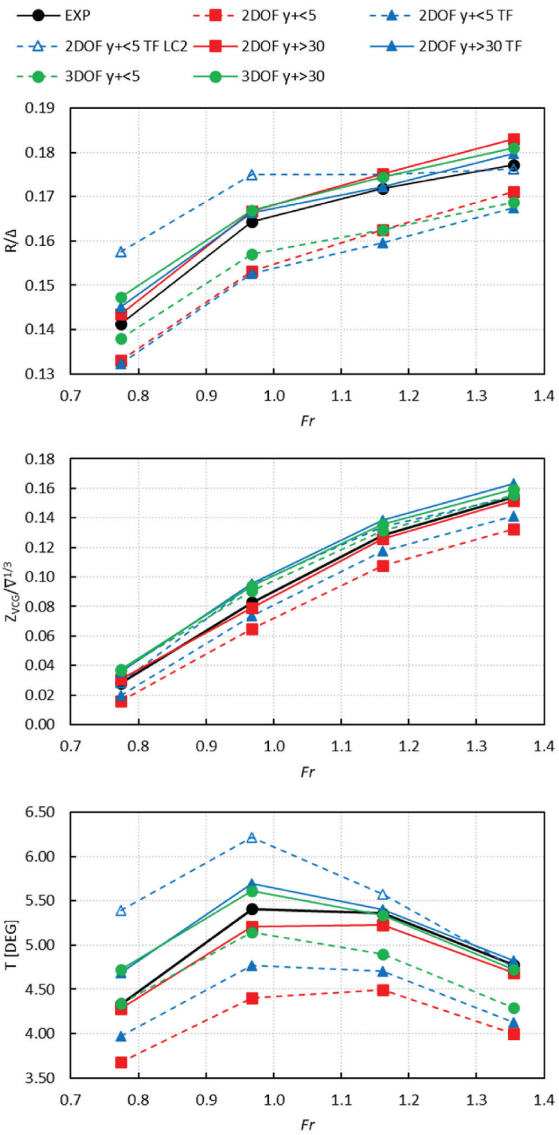

Fig. 11. Bare hull resistance, sinkage, and trim.

viscous sub-layer (y+ < 5) underestimated the running trim of the craft by 10 %–15 %, resulting in a 2 %–6 % increase in resistance. Since the comparison error was significantly larger than the validation uncertainty (0.6 % for 2DOF and 1.1 % for the 3DOF setup), the models were not validated (see Table C. 2 and C. 4).

On the other hand, the numerical models that utilized wall functions for wall treatment (y+ > 30) accurately predicted the resistance and running position of the bare hull. The 2DOF model was validated within the validation uncertainty for resistance, sinkage, and trim using the B (medium) mesh, as reported in Table C. 6. The 3DOF model was validated within the validation uncertainty for resistance, sinkage, and trim using the A (coarse) mesh, as reported in Table C. 8.

Fig. 12 shows the comparison of the accumulated pressure forces in z-direction over the hull length. It is observed that in the case with 15 prism layers (i.e. y+ < 5), there is significantly more pressure at the transom, and less pressure in the foreship ($x/L_{PP} > 0.4$). The centroid of the surfaces below these curves is the longitudinal centre of pressure. Based on the shape of the curves, one can deduce that in the case with 15 prism layers (i.e. y+ < 5), the centre of pressure is further aft. This increases the trimming moment, which pushes the bow down, ending up with a lower trim angle compared to the case with 8 prism layers (i.e. y+ > 30). Furthermore, compared to the 2DOF setup in the 3DOF setup, this difference is more pronounced.

5.1.2. *Influence of the initial bias in sinkage and trim*

In order to investigate possible sources of error or uncertainty, the position of the Centre of Gravity (CG) and Displacement could be two of them. The generation of grids may introduce discrepancies between the hull's CAD geometry and the discretized one in the simulation. Therefore, a quasi-static simulation was performed to assess the static trim angle and the sinkage of the hull. The quasi-static simulation means a simulation based on the setup detailed in Sec. 3 at a very low speed to check the hydrostatic details of the hull. Following the results of the verification and validation analysis in Sec. 5.1.1, the simulations were done at the A (coarse) mesh level.

The simulation that utilized the 2DOF approach yielded a static sinkage of 0.001 m and a static trim angle of -0.05°, bow up. This initial bias is equivalent from 8.0 % to 2.0 % of the dynamic rise/sinkage and 1 % of the dynamic trim in the studied speed range of $Fr = 0.774 - 0.968$ and $Fr_{\nabla} = 1.776 - 2.220$.

The simulation that utilized the 3DOF approach yielded a static sinkage of 0.001 m and a static trim angle of 0.013°, bow down. This initial bias is equivalent from 9.0 % to 2.0 % of the dynamic rise/sinkage and 0.3 % of the dynamic trim in the studied speed range of $Fr = 0.774 - 0.968$ and $Fr_{\nabla} = 1.776 - 2.220$.

The initial bias in sinkage and trim is rather small both for the 2DOF and the 3DOF simulations. However, since the validation uncertainties are small as well, these can influence the validation of the simulation,

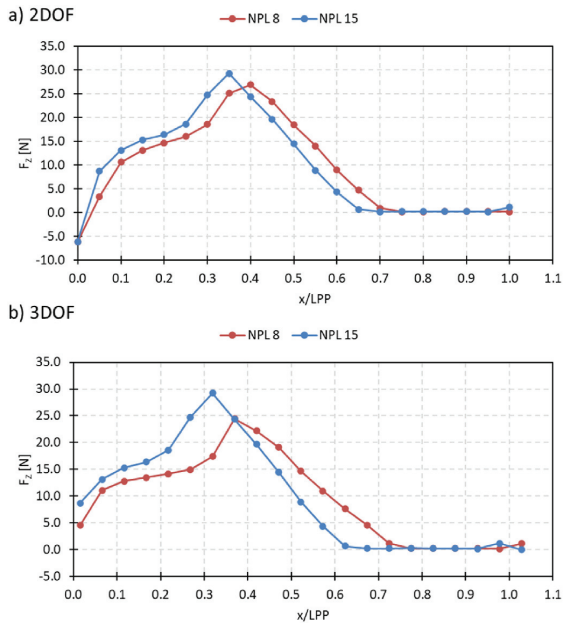

Fig. 12. Accumulated pressure forces in the z-direction on the hull blue (y+ < 5) red (y+ > 30). (For interpretation of the references to colour in this figure legend, the reader is referred to the Web version of this article.)

thus they are not negligible.

5.1.3. Influence of the trimming moment due to the towing force

The current study has identified the missing towing force as a significant cause of the large discrepancies between experimental and numerical results. However, the towing force increased the rise and running trim of the craft, which further reduced the resistance (Fig. 13). This means that the towing force only improved the running position (Fig. 11). Additionally, the towing force increased the running trim by 0.1–0.4°, with the highest increases occurring in the semi-displacement regime.

5.1.4. Influence of the position of CG

When simulating the hull in captive condition, A mesh (coarse mesh) and at a running position obtained from the model test the difference in the resistance was less than 0.14 %. Assuming that the validation uncertainty of captive simulations would be the same or even smaller i.e. ($U_V \leq 0.5\%$) the numerical model would be validated. While the captive simulation yielded a value of resistance close enough for the numerical model to be validated, it also produced an excess lift force and a trimming moment. This suggested that to plane in the given running position the model would have to be about 1.5 kg (7 %) heavier, and that the CG would have to be shifted afterwards. Applying these changes to the model, it was observed that the comparison error in resistance, sinkage, and trim was small enough for the model to be validated at the top speed (Fig. 11, 2DOF y+<5 TF LC2). However, at lower speeds large discrepancies were observed. Therefore, this approach was not further investigated.

5.1.5. Influence of the geometry of the hull

To test the hypothesis that the discrepancies in resistance and trim between the model test and numerical simulations are caused by differences in the geometry of the edges of the used models (Judge et al., 2020a), a new 3D model with rounded edges was prepared and simulated (Fig. 14). The simulation of a hull with rounded edges is significantly more resource intensive as the rounded edges require a denser mesh. The edges of the hull's 3D model were rounded with 2.0–3.0 mm fillets. The simulation was done with the 2DOF y+<5 setup with towing force at the A (coarse) mesh level.

Table 4 compares the resistance, sinkage, trim and wetted bottom surface of the hull with sharp edges to those of the hull with filleted edges. Fig. 15 compares the pressure distribution on the hulls with sharp and filleted edges. The resistance of the hull with rounded edges was only 0.1 % lower compared to the hull with sharp edges. The differences in the running position were significant. The sinkage of the hull with rounded edges was about 10 % lower, indicating less lift compared to the hull with sharp edges. The running trim of the hull with rounded edges is about 1 % higher compared to the hull with sharp edges.

5.2. Application of the numerical models to appended hull configurations

The 2DOF and 3DOF numerical setups using wall treatment functions (y+ > 30), that were validated in the previous section using the bare hull, were then applied to analyse hulls equipped with different

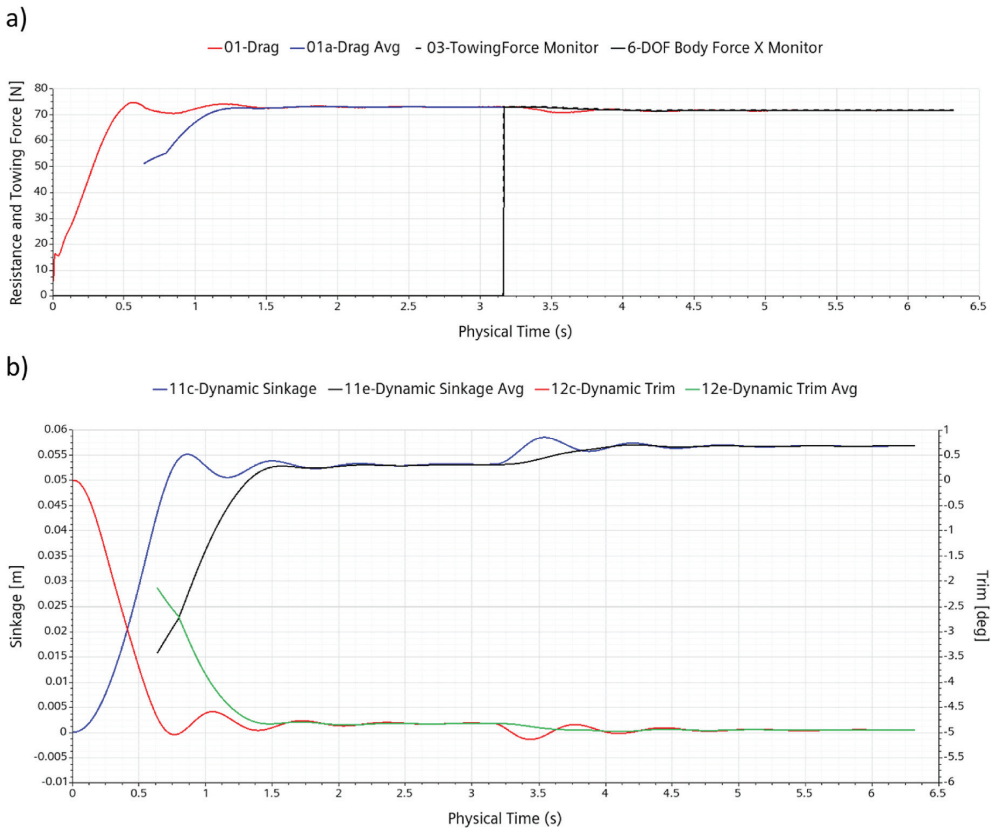

Fig. 13. Influence of the towing force on the resistance (a) and the running position of the hull (b) at $Fr = 1.355$.

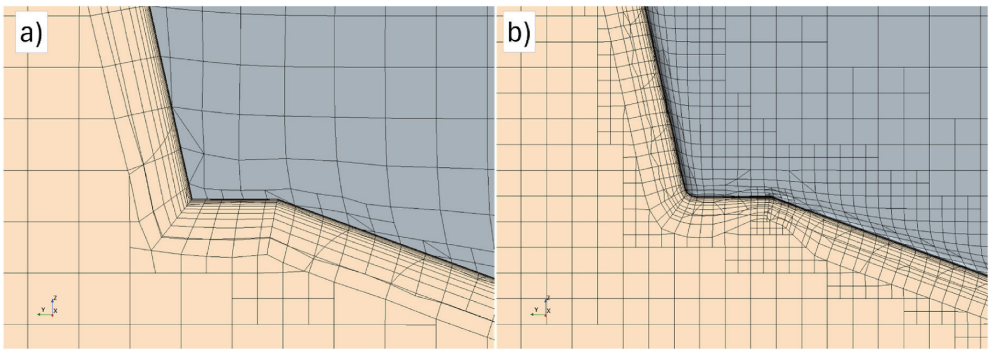

Fig. 14. Prism layers at the transom: a) without fillets, b) with fillets.

Table 4
Comparison of the hull with sharp edges to the hull with rounded edges.

Item	Unit	Without fillets	With fillets	Difference
R_{TM}	N	69.171	69.133	−0.1 %
z_{VCG}	m	−0.056	−0.050	−10.7 %
τ	deg	4.771	4.823	1.1 %
S_{WB}	m2	0.398	0.432	8.5 %

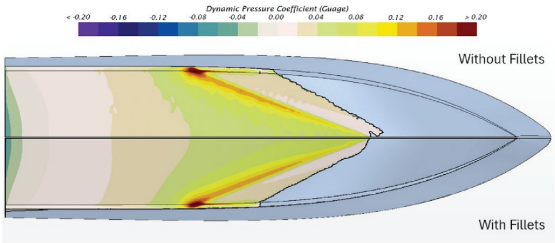

Fig. 15. Hull pressure coefficient: (top) without fillets, (bottom) with fillets $Fr = 1.355$.

appendages including spray rails (SR1 and SR2), chine strips (CSI), and V-shaped spray interceptors (VSI).

Figs. 16 and 17 display the distributions of pressure and the shear stress on the tested hull and spray rail configurations respectively. Figs. 18 and 19, and Table D. 1 compare the numerical results with the model test data in terms of total resistance, running trim and running sinkage. It is assumed that the validation errors that were evaluated for the bare hull at top speed in Sec. 5.1.2 (see Table C. 6 and C. 8) are of the same magnitude for other geometries and velocities. The appended hulls were simulated using the A (coarse) mesh.

Fig. 18 and Table D. 1 show that for the 2DOF setup, the comparison error E ranges from −5.6 % to 5 % for resistance, −17.5 %–.32.7 % for sinkage and −7.1 %–5.9 % for trim. The largest discrepancies were found in the semi-displacement region $Fr = 0.774 - 0.968$ and $Fr_{\nabla} = 1.776 - 2.220$. Similar observations were made in (Wheeler et al., 2021).

It can also be observed that the 3DOF yields results remarkably closer to experimental data than those given by the 2DOF approach. Since the comparison error of the 3DOF setup was mostly less than the validation error, the setup was mostly validated. That is most likely since the 3DOF constantly evaluates the equilibrium of forces, while the 2DOF model averages the average resistance of the previous 500 time-steps as the input for the towing force.

5.2.1. Spray rails

The 2DOF simulations underpredicted the resistance of the hull with conventional spray rails (SR1) by 1.9 %–5.0 %, with the largest discrepancies occurring at the lower velocities. Only at the top speed, the resistance deviates from the experimental data less than the validation uncertainty. However, trim was validated at the two higher speeds, while sinkage was validated at the two lower speeds. The 3DOF numerical model predicted the resistance, sinkage, and trim within the validation uncertainty through the whole speed range, except for sinkage at the lowest speed.

In the case of the narrow spray rails with a sharp bottom angle (SR2), both numerical models predicted the resistance within a 1.1 % difference from the model. Assuming the validation uncertainty for the 2DOF and the 3DOF setups is 2.3 % and 3.6 % respectively, these results can be considered validated. The 2DOF model predicted the sinkage with 3.3 %–5.5 % accuracy, which is less than the validation uncertainty of 5.7 %, hence the sinkage is validated at all speeds. However, the 2DOF model overestimated the trim by 4.2 %–7.1 %, and with the validation uncertainty being 4 %, these results are not validated.

The 3DOF model performed significantly better, it predicted the resistance and trim within the respective validation uncertainties. Furthermore, the resistance was predicted within 0.1 %–0.4 % difference from the experimental data. The trim was predicted with 0.9 %–4.7 % accuracy, with the larger discrepancies occurring at the lower speeds. The sinkage was mostly validated except for $Fr = 0.968$ where the discrepancy was larger than the validation uncertainty.

Fig. 16 shows that compared to narrow spray rails, wider spray rails increase the pressure on the hull visibly more. Therefore, it is reasonable to assume that for this hull operating at low planing speed, the differences in resistance were mostly due to the friction and pressure of the spray rails.

Fig. 19 displays the relative change in resistance, sinkage, and trim normalized by the corresponding values of the bare hull. It compares the predictions made with the numerical simulations to those made based on the experimental results. Both the 2DOF and 3DOF numerical models overestimate the reduction in resistance. While the experimental results show that the spray rails either increase the resistance or the change is negligible, the numerical simulations suggest a 2 % reduction in resistance. However, the predictions of the 3DOF model are closer to the experimental results, particularly those of the trim and sinkage.

However, one must keep in mind the simulation uncertainties, which were larger or of the same magnitude compared to the changes in resistance, sinkage and trim. This means that the predictions of the numerical simulations are negligible or inconclusive at best. Thus, the accuracy of the numerical simulations needs to be improved. Nonetheless, judging on Figs. 16 and 19 one can see that the narrow spray rails (SR2) deflect the spray and reduce the resistance without increasing the trim just as the conventional spray rails (SR1).

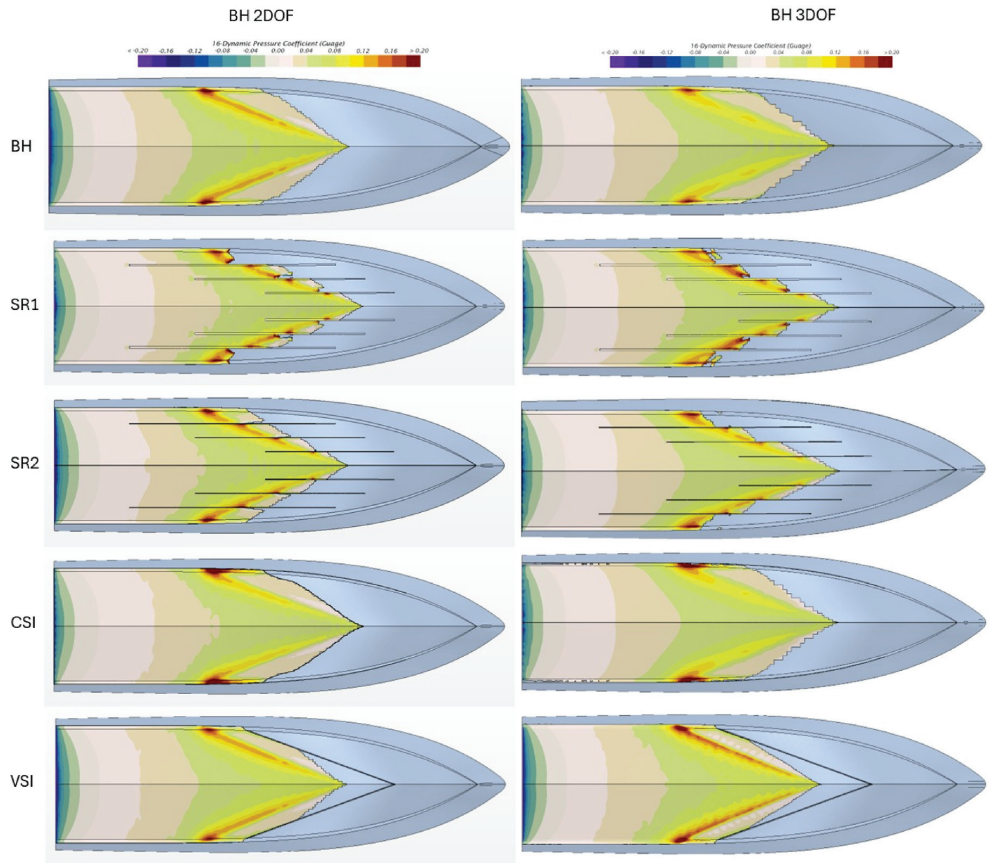

Fig. 16. Pressure distribution on the tested hull configurations at $Fr = 1.355$.

5.2.2. Chine strips

The numerical simulations of the bare hull with a chine strip (CSI) were mostly validated using both 2DOF and 3DOF numerical setups. However, the 3DOF performed better, since it's results for resistance, sinkage and trim were validated within the validation uncertainty at all velocities, except for sinkage at the lowest speed. The 2DOF setup predicted accurately the resistance at the three higher $Fr = 0.968$–1.355. It also predicted the trim at the top speed within the validation uncertainty. However, the results of sinkage and trim were invalidated since validated since the discrepancies from the experimental data were larger than the validation uncertainty. In Figs. 18 and 19, one can observe that the predictions of change in resistance, sinkage and trim made with the 3DOF model are significantly closer to the experimental data compared to those done with the 2DOF model.

5.2.3. V-shaped spray interceptor

The 2DOF model overestimated the resistance by 5.6 % at the top speed and by 3.5 % at the $Fr = 1.162$, which is more than the validation uncertainty of 2.3 %. However, at the two lower velocities the discrepancies in resistance were less than the validation uncertainty. Sinkage and trim were mostly validated, except for the sinkage at the lowest speed and trim at $Fr = 0.968$.

The 3DOF provided significantly better results, with most of the discrepancies in resistance, sinkage and trim being less than the validation uncertainty. The exceptions were the resistance at top speed of $Fr = 1.355$ and sinkage at $Fr = 0.774$–0.968.

In Fig. 19 one can observe that the predictions of change in resistance, sinkage and trim made with the 3DOF model are significantly closer to the experimental data compared to those done with the 2DOF model. Also, the numerical predictions of reductions in resistance provided by the 3DOF model were more pessimistic compared to the experimental data.

The V-shaped spray interceptors VSI1 accounted for a negative resistance of 1.6 % of total resistance (R_{TM}). This is because the V-shaped spray interceptor was in the spray area forward of the stagnation line, thus deflecting the oncoming spray and producing a reaction force that reduced the total resistance. It is important to note that since the VSI only produced a comparatively small reaction force (1.6 % R_{TM}) in the direction of the hull's motion, the rest of the difference in resistance was due to the absence of pressure and frictional resistance of the absent spray rails as seen in Figs. 16 and 17.

6. Conclusions

This article presents a verification and validation study of various numerical models of a planing hard chine hull in calm water. The numerical models were validated against the experimental results of a bare hull. The best-performing numerical models were used to investigate the effect of spray rails, chine strips and V-shaped spray interceptors on the resistance and running position of the planing hard-chine hull. The verification and validation analysis and the consequent comparative study yielded the following conclusions.

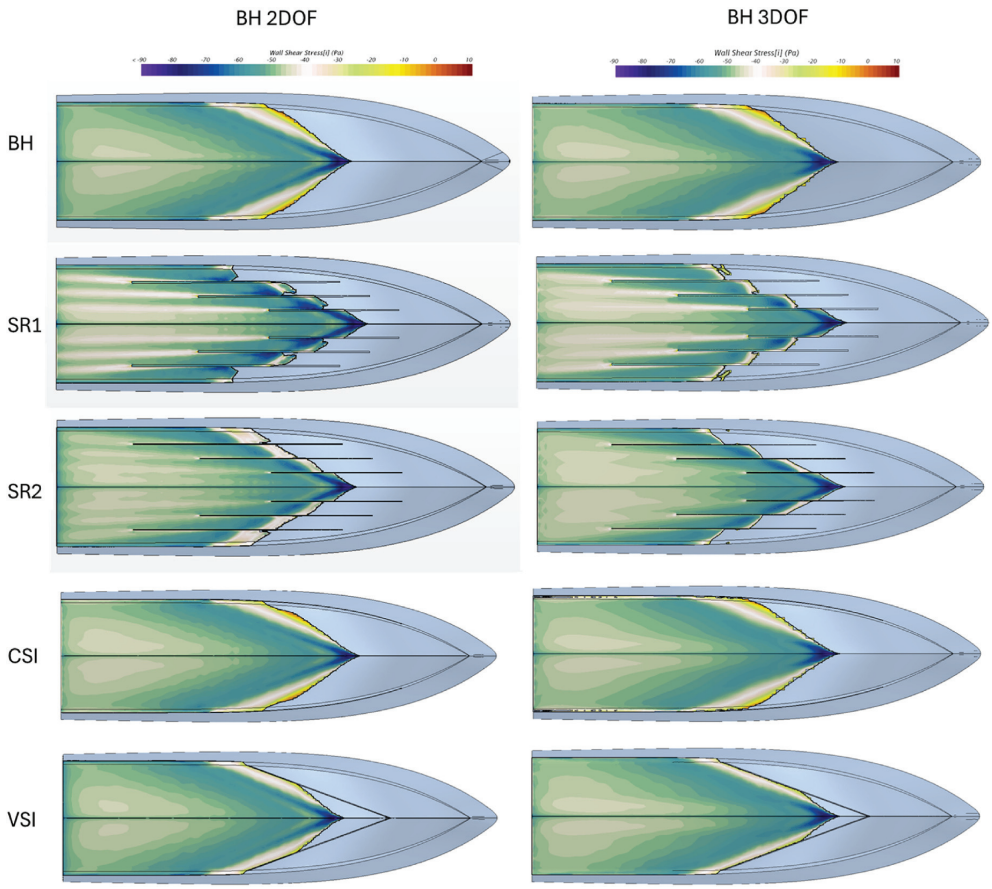

Fig. 17. Shear stress distribution on the tested hull configuration at $Fr = 1.355$.

The influence of wall treatment. The models that solved the viscous sub-layer directly ($y+ < 5$) underestimated the running trim of the craft by 10 %–15 % and therefore its resistance by 2 %–6 %. Since the comparison error was much larger than the validation uncertainty, these models were not validated. On the other hand, the numerical models that used wall functions for wall treatment ($y+ > 30$) predicted the resistance and the running position of the bare hull within the validation uncertainty, hence they were validated.

Influence of the trimming moment due to the towing force. The current study has identified the missing towing force as a significant cause of the large discrepancies between experimental and numerical results. However, the towing force increased the rise and running trim of the craft, which further reduced the resistance. That is the towing force only improved the running position. Furthermore, the towing force increased the running trim by 0.1°–0.4°, with the highest increases occurring in the semi-displacement regimes.

Influence of the geometry of the hull. The simulation of a hull with rounded edges is significantly more resource-intensive since the rounded edges require a denser mesh. The resistance of the hull with rounded edges was only 0.1 % lower compared to the hull with sharp edges. The differences in the running position were significant. The sinkage of the hull with rounded edges was about 10 % lower which indicates less lift compared to the hull with sharp edges. The running trim of the hull with rounded edges is about 1 % higher compared to the hull with sharp edges.

Influence of the initial bias in sinkage and trim. The uncertainty in the position of the Centre of Gravity (CG) could be a factor. Therefore, a quasi-static simulation was performed to assess the static trim angle and the sinkage of the hull. In the case of a 2DOF setup, the simulation yielded a static sinkage of 0.001 m and a static trim angle of −0.05° (bow up). The 3DOF setup yielded a static sinkage of 0.001 m and a static trim angle of 0.01° (bow down). Since the validation uncertainties are small, these biases can influence the validation of the simulation, thus they are not negligible.

Towing test vs CFD. The comparative study of hulls with spray rails, chine strips and V-shape spray interceptors, showed that numerical simulations tend to be too optimistic compared to model test results. In this study, the changes in resistance were either less than the validation uncertainties i.e. negligible or they were slightly larger than the validation uncertainty. The differences in resistance between different spray rail setups observed in experimental results were small, ranging from 2 % to 3 %. Hence, the numerical model needs to be further improved to reduce the simulation uncertainty. On the other hand, this numerical model is most likely to predict accurately the influence of different spray rails at much higher planing speeds, where the differences in resistance are known to be much higher.

7. Future work

The future work activities can be summarized with the works that

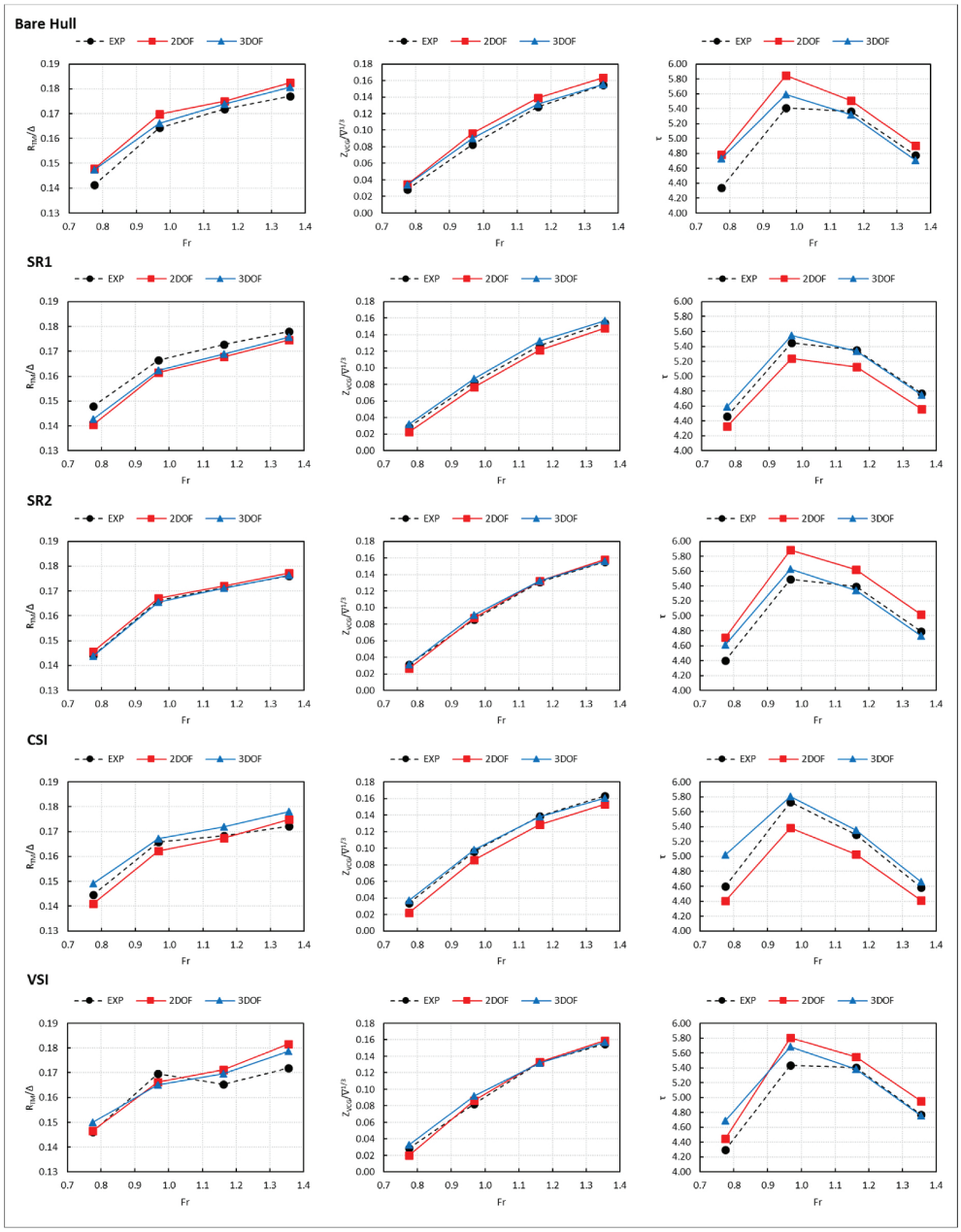

Fig. 18. EFD vs CDF: resistance, sinkage, and trim.

has to be carried out to answer the following bullets.

1. Is it only relevant to the model test (scale simulation) or can it be used for ship scale? The present study was conducted on a model scale to verify and validate the numerical models. It is not known whether the same differences due to wall treatment would manifest in ship scale.
2. Is the 2DOF setup with a towing force and the 3DOF setup only relevant for planing and semi-displacement? The numerical results show that the towing force has a more pronounced effect on the running position at semi-displacement speeds. This indicates that the towing force could improve the CFD predictions at even slower speeds. It is not known how the towing force would affect the displacement vessels.
3. In this study, AMR was only applied in the tank region while the overset region was not refined. There are two ways to implement AMR. The overset offset from the hull could be made smaller and the mesh in it finer. Alternatively, AMR could be enabled both in the

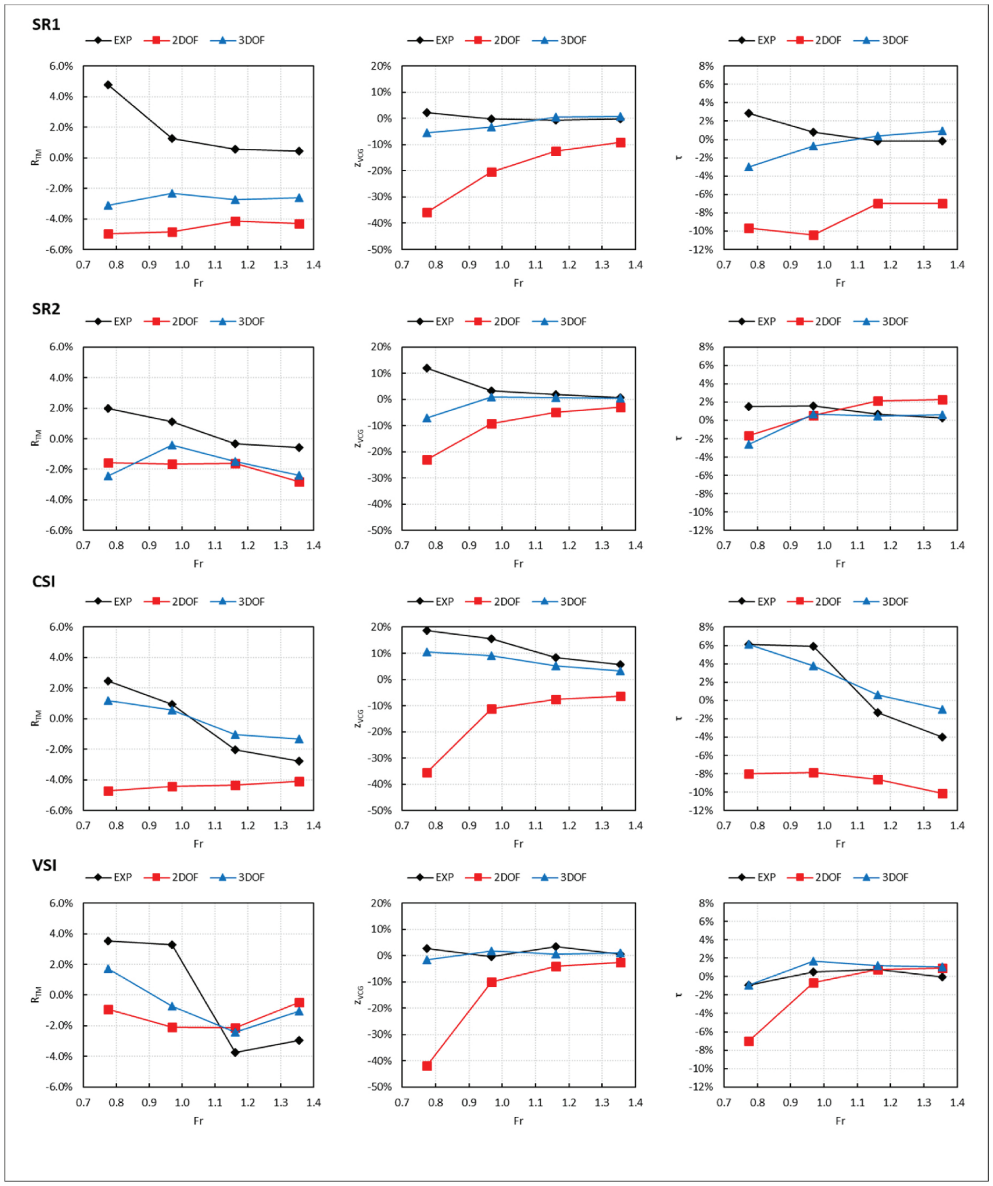

Fig. 19. Comparison of EXP, 2DOF and 3DOF simulations: resistance, sinkage, and trim normalized by the bare hull.

tank and in the overset regions. Whether that would improve the accuracy of the simulation is yet to be investigated.

4. The bare hull with filleted edges was only simulated using the $y+ < 5$ setup. It is unknown whether the effect of the filleted edges would be the same if simulated using the $y+ > 30$ approach.

CRediT authorship contribution statement

Mikloš Lakatoš: Writing – original draft, Visualization, Validation, Methodology, Investigation, Formal analysis, Conceptualization. **Simone Mancini:** Writing – review & editing, Writing – original draft, Validation, Methodology, Formal analysis. **Rasul Niazmand Bilandi:** Writing – review & editing, Writing – original draft. **Kristjan Tabri:** Writing – review & editing, Supervision, Project administration, Funding acquisition, Conceptualization.

Declaration of competing interest

The authors declare that they have no known competing financial interests or personal relationships that could have appeared to influence the work reported in this paper.

Acknowledgements

This work was supported by the Estonian Research Council grant (PRG1820). This help is greatly appreciated.

Appendix A. Summary of recent CFD studies on calm water performance of planing hulls

Table A. 1
Summary of recent CFD studies on calm water performance of planing hulls.

Data	Mesh techniques		Wall Treatment		Turbulence models							CFD codes	Experimental data
	Overset	Morphing/ Integrated	y+ < 5	y+ > 30	k - ω SST	k - ω	k-ε	Realizable k - ε	DES	Blended k - ω/k - ε	Spalart – AIImaıas		
Caponnetto et al. (2003)	✓	✓		✓			✓					Comet	NA
O'Shea et al. (2012) and Fu et al. (2013)		✓	N. A.	N.A.								Euler Code NFA	Fridsma (1969)
Mousaviraad et al. (2015)	✓		✓							✓		CFDShip-Iowa V4.5	Fridsma (1969)
Sukas et al. (2017)	✓	✓	N. A.	N.A.			✓					Star-CCM+	Fridsma (1969) and Bal (2014)
De Luca et al. (2016)	✓	✓					✓					Star-CCM+	De Luca and Pensa (2017)
Mancini et al. (2017)	✓	✓		✓	✓		✓					FINE™/ Marine Star-CCM+	De Luca and Pensa (2017)
Broglia and Durante (2018)	✓			✓							✓	CNR-INSEAN	Provided by the company
Avci and Barlas (2018)	✓			✓			✓					Star-CCM+	Avci and Barlas (2018)
Li et al. (2019)	✓			✓			✓					OpenFOAM	Weil et al. (Not published)
Wei et al. (2019)	✓			✓						✓		Star-CCM+	Taunton et al. (2010)
Judge et al. (2020)	✓			✓						✓		CFDShip-Iowa V4.5 Star-CCM+	Judge et al. (2020)
Behara et al. (2020)	✓			✓								REX	Behara et al. (2020)
Nimmagadda et al. (2020)	✓	✓		✓			✓					Star-CCM+	Nimmagadda et al. (2020)
Lee et al. (2021)	✓			✓						✓		CFDShip-Iowa V4.5 Star-CCM+	Lee et al. (2021)
Hosseini et al. (2021)	✓	✓		✓			✓		✓			Star-CCM+	De Luca and Pensa (2017)
Gray-Stephens et al. (2021)	✓			✓			✓					Star-CCM+	Taunton et al. (2010)
Jin et al. (2023)	✓			✓	✓	✓	✓	✓				Star-CCM+	Fridsma (1969)
Niazmand Bilandi et al. (2024a)	✓	✓	✓	✓	✓			✓				Star-CCM+	De Luca and Pensa (2017) and Vitiello et al. (2022)
Wheeler et al. (2021)	✓			✓				✓				Star-CCM+	Lee et al. (2017)

Appendix B. Laboratory instrumentation and measurement

The calm water resistance tests were conducted in the towing tank of the Marine Technology Competence Centre (MARTE) of Tallinn University of Technology (see Table B. 1) following the ITTC guideline 7.5-02-02-01 (ITTC, 2017b). The models were tested in semi-captive conditions, i.e. the models were free to pitch and heave. During the tests, total resistance R_{TM} and running sinkage at the aft and fore perpendiculars z_{VF} and z_{VA} were measured at 200 Hz sampling frequency. The numbers of repeated runs and the data acquisition times are shown in Table B. 2.

The running trim angle τ of the craft was evaluated from the readings of running sinkage at the aft (z_{VA}) and the bow (z_{VF}) perpendiculars that were measured with a linear measuring wire and a draw-wire encoder with the bias of 0.05 % in a range of $\pm$1250 mm. The uncertainty analysis was carried out following the ITTC guidelines 7.5-02-02-02 and 7.5-02-02-02.1 (ITTC, 2017b, 2014). Table B. 3 shows the uncertainties of resistance, trim and sinkage in the design condition of the craft.

The bias of the dynamometer was 0.2 % in the range of 0–0.2 kN. The dynamometer was calibrated before the model test according to the ITTC Procedure 7.5-01-03-01 (ITTC, 2017c). Five loads were implemented by weights and randomly applied three times for each load. The fitting curve for predicting the force was obtained by linear regression with a standard deviation of SEE = 0.077 N. The tachometer was calibrated at 1 m/s, 2 m/s, 3 m/s, 4, m/s and 5 m/s, four runs for each speed except for the speed 1 m/s, which was run 6 times. The fitting curve for predicting the speed was obtained by linear regression with a standard deviation of SEE = 0.0011 m/s.

The median uncertainty of resistance, sinkage and trim was 0.4 %, 1.5 % and 0.7 % respectively. Table B. 3 gives an overview of the uncertainty of measured items through the test campaign.

Table B. 1
Main dimensions of the towing tank.

Parameter		
Maximum tank length	l	60 m
Maximum tank breadth	b	5 m
Maximum tank depth	h	3 m
Maximum carriage speed	V	5.5 m/s

Table B. 2
Numbers of repeated runs and data acquisition times.

V_M [m/s]	No. of Repeated Runs	Data Acquisition Time [s]
3.254	2–4	9
4.067	2–4	6
4.880	2–5	4
5.694	2–6	3

Table B. 3
Uncertainties of parameters measured through the test campaign.

	U_p' (R_{TM}/Δ)	U_p ($z_{VCG}/\nabla^{1/3}$)	U_p (τ) [deg]
Min	0.2 %	0.001	0.027
Max	1.7 %	0.004	0.085
Average	0.4 %	0.002	0.035
Median	0.4 %	0.001	0.032

Appendix C. Validation and verification on the bare hull

Table C. 1
Main parameters of the four tested grid configurations 2DOF Y+ < 5 with towing force.

Grid	Base size [m]	BS/L_{PP}	Tank	Overset	Total	Average Wall Y+
A	0.0712	0.040	102,240	410,125	512,365	2.635
B	0.0600	0.033	163,986	549,615	713,601	2.635
C	0.0514	0.029	241,866	733,779	975,645	2.630
D	0.0450	0.025	341,226	942,996	1,284,222	2.631

Table C. 2
Results of the verification and validation analysis 2DOF Y+ < 5 with towing force.

	Grids	R_G	p_G (RE)	p_G (LSR)	$\|1 - C_G\|$	$\%U_G$ GCI	$\%U_G$ CF	$\%U_G$ GCI-LSR	$\%U_{SN}$	$\%U_D$	$\%U_V$	$\%\|E\|$	Validation (Yes/No)
R_{TM}	A-B-C	1.00	0.01	$\sqrt{2}$	1.00	144.39	0.75	1.5	1.5	0.3	1.5	4.7	No
	B-C-D	0.43	2.46		0.35	0.15	0.61						
z_{VCG}	A-B-C	3.89	−3.92	$\sqrt{2}$	1.74	N.A.	N.A.	4.0	4.0	0.8	4.1	8.3	No
	B-C-D	0.24	4.13		2.18	0.14	0.60						
τ	A-B-C	4.17	−4.12	$\sqrt{2}$	1.76	N.A.	N.A.	1.3	1.3	0.6	1.4	13.6	No
	B-C-D	−2.47	N.A.		N.A.	N.A.	N.A.						
S_{WB}	A-B-C	8.88	−6.30	$\sqrt{2}$	1.89	N.A.	N.A.	2.1	2.1	1.0	2.6	2.2	Yes
	B-C-D	649	−5.40		1.85	N.A.	N.A.						

Table C. 3
Main parameters of the four tested grid configurations 3DOF Y+ < 5.

Grid	Base size [m]	BS/L_{PP}	Tank	Overset	Total	Average Wall Y+
A	0.0712	0.040	299,765	357,656	657,421	2.358
B	0.0600	0.033	432,999	455,209	888,208	2.363
C	0.0514	0.029	588,331	594,736	1,183,067	2.360
D	0.0450	0.025	748,117	749,544	1,497,661	2.299

Table C. 4
Results of the verification and validation analysis of the numerical model 3DOF Y+ < 5.

	Grids	R_G	p_G (RE)	p_G (LSR)	$\|1 - C_G\|$	$\%U_G$ GCI	$\%U_G$ CF	$\%U_G$ GCI-LSR	$\%U_{SN}$	$\%U_D$	$\%U_V$	$\%\|E\|$	Validation (Yes/No)
R_{TM}	A-B-C	−4.48	N.A.	$\sqrt{2}$	N.A.	N.A.	N.A.	0.8	0.8	0.3	0.9	4.4	No
	B-C-D	0.16	5.25		4.18	0.01	0.11						
z_{VCG}	A-B-C	0.26	3.83	$\sqrt{2}$	1.78	0.32	1.18	1.2	1.2	0.8	1.4	0.5	Yes
	B-C-D	0.45	2.33		0.24	0.09	0.10						
τ	A-B-C	−1.17	N.A.	$\sqrt{2}$	N.A.	N.A.	N.A.	0.2	0.2	0.6	0.6	10.9	No
	B-C-D	−0.95	N.A.		N.A.	0.06	0.06						
S_{WB}	A-B-C	−0.56	N.A.	$\sqrt{2}$	N.A.	0.51	0.51	7.7	7.7	1.0	7.8	7.1	Yes
	B-C-D	9.60	−6.53		1.90	N.A.	N.A.						

Table C. 5
Main parameters of the four tested grid configurations 2DOF Y+ > 30 with towing force.

Grid	Base size [m]	BS/L_{PP}	Tank	Overset	Total	Average Wall Y+
A	0.0712	0.040	102,615	262,539	365,154	72.912
B	0.0600	0.033	164,467	353,186	517,653	72.920
C	0.0514	0.029	242,900	474,773	717,673	73.263
D	0.0450	0.025	342,530	618,104	960,634	73.371

Table C. 6
Results of the verification and validation analysis of the numerical model 2DOF Y+ >30 with towing force.

	Grids	R_G	p_G (RE)	p_G (LSR)	$\|1 - C_G\|$	$\%U_G$ GCI	$\%U_G$ CF	$\%U_G$ GCI-LSR	$\%U_{SN}$	$\%U_D$	$\%U_V$	$\%\|E\|$	Validation (Yes/No)
R_{TM}	A-B-C	−0.81	N.A.	$\sqrt{2}$	N.A.	0.75	0.75	2.3	2.3	0.3	1.9	1.9	Yes
	B-C-D	−0.85	N.A.		N.A.	0.61	0.61						
z_{VCG}	A-B-C	−3.23	N.A.	$\sqrt{2}$	N.A.	N.A.	N.A.	5.4	5.4	0.8	5.7	0.4	Yes
	B-C-D	0.11	6.26		6.74	0.05	0.59						
τ	A-B-C	−1.22	N.A.	$\sqrt{2}$	N.A.	N.A.	N.A.	3.9	3.9	0.6	4.0	0.5	Yes
	B-C-D	−0.19	N.A.		N.A.	1.61	1.61						
S_{WB}	A-B-C	−2.17	N.A.	$\sqrt{2}$	N.A.	N.A.	N.A.	3.7	2.7	1.0	2.9	10.7	No
	B-C-D	0.34	3.12		0.95	0.35	0.82						

Table C. 7
Main parameters of the four tested grid configurations 3DOF Y+ > 30.

Grid	Base size [m]	BS/L_{PP}	Tank	Overset	Total	Average Wall Y+
A	0.0712	0.040	322,445	194,497	516,942	72.307
B	0.0600	0.033	461,853	280,921	742,774	72.091
C	0.0514	0.029	626,030	396,977	1,023,007	72.568
D	0.0450	0.025	796,509	526,138	1,322,647	72.845

Table C. 8
Results of the verification and validation analysis of the numerical model 3DOF Y+ > 30.

	Grids	R_G	p_G (RE)	p_G (LSR)	$\|1 - C_G\|$	$\%U_G$ GCI	$\%U_G$ CF	$\%U_G$ GCI-LSR	$\%U_{SN}$	$\%U_D$	$\%U_V$	$\%\|E\|$	Validation (Yes/No)
R_{TM}	A-B-C	−0.49	N.A.	$\sqrt{2}$	N.A.	0.88	0.88	3.2	3.2	0.3	3.2	2.2	Yes
	B-C-D	1.97	−1.96		1.49	N.A.	N.A.						
z_{VCG}	A-B-C	−0.42	N.A.	$\sqrt{2}$	N.A.	1.83	1.83	4.9	4.9	0.8	5.0	1.1	Yes
	B-C-D	1.58	−1.33		1.37	N.A.	N.A.						
τ	A-B-C	−0.64	N.A.	$\sqrt{2}$	N.A.	2.35	2.35	7.3	7.3	0.6	7.3	0.9	Yes
	B-C-D	0.94	−0.17		0.94	N.A.	N.A.						
S_{WB}	A-B-C	−0.45	N.A.	$\sqrt{2}$	N.A.	1.72	1.72	7.1	7.1	1.0	7.2	10.5	No
	B-C-D	2.18	−2.25		1.54	N.A.	N.A.						

Appendix D. Comparison of the numerical results with the experimental data

Table D. 1
Comparison of the numerical results with the experimental data.

Fr	Fr_∇	2DOF			3DOF				2DOF			3DOF		
		R_{TM}/Δ	$z_{VCG}/\nabla^{1/3}$	τ [deg]	R_{TM}/Δ	$z_{VCG}/\nabla^{1/3}$	τ [deg]		E (R_{TM})	E (z_{VCG})	E (τ)	E (R_{TM})	E (z_{VCG})	E (τ)
BH														
0.774	1.776	0.145	0.033	4.636	0.147	0.034	4.741		−2.8 %	−17.5 %	−6.9 %	−4.4 %	−20.0 %	−9.3 %
0.968	2.220	0.166	0.093	5.641	0.167	0.090	5.623		−1.2 %	−11.8 %	−4.3 %	−1.5 %	−8.9 %	−4.0 %
1.162	2.664	0.172	0.136	5.355	0.174	0.132	5.354		−0.2 %	−5.7 %	0.1 %	−1.5 %	−2.9 %	0.1 %
1.355	3.109	0.181	0.155	4.799	0.181	0.156	4.734		−1.9 %	−0.4 %	−0.5 %	−2.2 %	−1.1 %	0.9 %
								Average	−1.5 %	−8.9 %	−2.9 %	−2.4 %	−8.2 %	−3.1 %
SR1														
0.774	1.776	0.141	0.022	4.325	0.143	0.032	4.591		5.0 %	22.3 %	3.0 %	3.5 %	−10.6 %	−3.0 %
0.968	2.220	0.162	0.077	5.240	0.162	0.087	5.551		2.9 %	7.3 %	3.9 %	2.4 %	−5.1 %	−1.8 %
1.162	2.664	0.168	0.122	5.122	0.169	0.132	5.339		3.0 %	4.4 %	4.3 %	2.2 %	−3.8 %	0.2 %
1.355	3.109	0.175	0.148	4.562	0.176	0.157	4.752		1.9 %	3.8 %	4.4 %	1.2 %	−1.8 %	0.4 %
								Average	3.2 %	9.5 %	3.9 %	2.3 %	−5.3 %	−1.1 %
SR2														
0.774	1.776	0.146	0.027	4.708	0.144	0.031	4.609		−1.1 %	14.7 %	−7.0 %	0.2 %	0.6 %	−4.7 %
0.968	2.220	0.167	0.088	5.881	0.166	0.091	5.631		−0.5 %	−2.2 %	−7.1 %	0.4 %	−5.8 %	−2.5 %
1.162	2.664	0.172	0.132	5.623	0.171	0.132	5.346		−0.5 %	−1.1 %	−4.2 %	0.1 %	−1.2 %	0.9 %
1.355	3.109	0.177	0.158	5.016	0.176	0.156	4.735		−0.7 %	−1.8 %	−4.7 %	−0.1 %	−0.5 %	1.1 %
								Average	−0.7 %	2.4 %	−5.7 %	0.1 %	−1.7 %	−1.3 %
CSI														
0.774	1.776	0.141	0.022	4.404	0.149	0.037	5.020		2.6 %	32.7 %	4.3 %	−3.1 %	−11.6 %	−9.1 %
0.968	2.220	0.162	0.086	5.387	0.167	0.098	5.803		2.2 %	10.4 %	5.9 %	−0.8 %	−2.4 %	−1.3 %
1.162	2.664	0.167	0.129	5.030	0.172	0.138	5.352		0.6 %	7.4 %	4.9 %	−2.1 %	0.5 %	−1.2 %
1.355	3.109	0.175	0.153	4.409	0.178	0.161	4.662		−1.6 %	6.4 %	3.9 %	−3.4 %	1.5 %	−1.7 %
								Average	0.9 %	14.2 %	4.8 %	−2.4 %	−3.0 %	−3.3 %
VSI														
0.774	1.776	0.147	0.020	4.450	0.150	0.033	4.686		−0.3 %	30.0 %	−3.6 %	−2.6 %	−14.8 %	−9.1 %
0.968	2.220	0.166	0.087	5.808	0.165	0.092	5.685		2.0 %	−5.0 %	−6.9 %	2.8 %	−10.9 %	−4.6 %
1.162	2.664	0.171	0.133	5.549	0.170	0.132	5.383		−3.5 %	−0.5 %	−2.7 %	−2.5 %	0.5 %	0.4 %
1.355	3.109	0.182	0.159	4.950	0.179	0.157	4.755		−5.6 %	−2.4 %	−3.7 %	−4.0 %	−1.1 %	0.4 %
								Average	−1.9 %	5.5 %	−4.2 %	−1.6 %	−6.6 %	−3.2 %

References

Avci, A.G., Barlas, B., 2018. An experimental and numerical study of a high speed planing craft with full-scale validation. J. Mar. Sci. Technol. 26, 617–628. https://doi.org/10.6119/JMST.201810_26(5).0001.

Bal, S., et al., 2014. 30 Knot Motorboat Model Experiments and Analyses. Report No. 2014- Gozuyilmaz-P05-M393.

Behara, S., Arnold, A., Martin, J.E., Harwood, C.M., Carrica, P.M., 2020. Experimental and computational study of operation of an amphibious craft in calm water. Ocean Engineering 209, 107460. https://doi.org/10.1016/J.OCEANENG.2020.107460.

Broglia, R., Durante, D., 2018. Accurate prediction of complex free surface flow around a high speed craft using a single-phase level set method. Comput. Mech. 62, 421–437. https://doi.org/10.1007/s00466-017-1505-1.

Caponnetto, M., Söding, H., Azcueta, R., 2003. Motion simulations for planing boats in waves. Ship Technol. Res. 50, 182–198. https://doi.org/10.1179/str.2003.50.4.006.

Celik, I.B., Ghia, U., Roache, P.J., Freitas, C.J., Coleman, H., Raad, P.E., 2008. Procedure for estimation and reporting of uncertainty due to discretization in CFD applications. Journal of Fluids Engineering, Transactions of the ASME 130, 780011–780014. https://doi.org/10.1115/1.2960953.

Clement, E.P., 1964a. Effects of Longitudinal Bottom Spray Strips on Planing Boat Resistance (No. 1818), Report. David Taylor Model Basin, Department of The Navy, Washington, DC.

Clement, E.P., 1964b. Reduction of Planing Boat Resistance by Deflection of the Whisker Spray (No. 1929), Report. David Taylor Model Basin, Department of The Navy, Washington, DC.

Cui, L., Chen, Z., Feng, Y., Li, G., Liu, J., 2021. An improved VOF method with anti-ventilation techniques for the hydrodynamic assessment of planing hulls-Part 2: applications. Ocean Engineering 237, 109505. https://doi.org/10.1016/j.oceaneng.2021.109505.

De Luca, F., Mancini, S., Miranda, S., Pensa, C., 2016. An extended verification and validation study of CFD simulations for planing hulls. J. Ship Res. 60, 101–118. https://doi.org/10.5957/JOSR.60.2.160010.

De Luca, F., Mancini, S., Pensa, C., Staiano, G., 2014. Numerical evaluation (CFD) of wake and thrust deduction fraction of a warped hard chine hulls systematic series. In: 10th RINA High Speed Marine Vehicles Symposium, pp. 1–8.

De Luca, F., Pensa, C., 2017. The Naples warped hard chine hulls systematic series. Ocean Engineering 139. https://doi.org/10.1016/j.oceaneng.2017.04.038.

De Marco, A., Mancini, S., Miranda, S., Scognamiglio, R., Vitiello, L., 2017. Experimental and numerical hydrodynamic analysis of a stepped planing hull. Appl. Ocean Res. 64, 135–154. https://doi.org/10.1016/j.apor.2017.02.004.

Eça, L., Hoekstra, M., 2014. A procedure for the estimation of the numerical uncertainty of CFD calculations based on grid refinement studies. J. Comput. Phys. 262, 104–130. https://doi.org/10.1016/j.jcp.2014.01.006.

Eça, Luis, Hoekstra, M., 2006. Discretization uncertainty estimation based on a least Squares version of the grid convergence Index. In: Proceedings of the Second Workshop on CFD Uncertainty Analysis, pp. 1–27. Lisbon.

Fridsma, G., 1969. A systematic study of the rough-water performance of planning boats. Tech. Rep. 1275. Davidson Laboratory, Stevens Institue of Technology, Hoboken, NJ, USA. Hoboken, New Jersey.

Fu, T.C., O'Shea, T.T., Judge, C.Q., Dommermuth, D., Brucker, K., Wyatt, D.C., 2013. A detailed assessment of numerical flow analysis (NFA) to predict the hydrodynamics of a deep-V planing hull. Int. Shipbuild. Prog. 60, 145–169. https://doi.org/10.3233/ISP-130087.

Gray-Stephens, A., Tezdogan, T., Day, S., 2021. Minimizing numerical ventilation in computational fluid dynamics simulations of high-speed planning hulls. J. Offshore Mech. Arctic Eng. 143. https://doi.org/10.1115/1.4050085.

Gray-Stephens, A., Tezdogan, T., Day, S., 2019. Strategies to minimise numerical ventilation in CFD simulations of high-speed planing hulls. In: Proceedings of the International Conference on Offshore Mechanics and Arctic Engineering - OMAE, pp. 1–10. https://doi.org/10.1115/OMAE2019-95784.

Hosseini, A., Tavakoli, S., Dashtimanesh, A., Sahoo, P.K., Körgesaar, M., 2021. Performance prediction of a hard-chine planing hull by employing different CFD models. J. Mar. Sci. Eng. 9, 481. https://doi.org/10.3390/JMSE9050481, 2021, Vol. 9, Page 481.

ITTC, 2021. 7.5-03-01-01 uncertainty analysis in CFD verification and validation, methodology and procedures. In: 29th International Towing Tank Conference, Recommended Procedures and Guidelines, pp. 1–15.

ITTC, 2017a. 7.5-03-02-03 practical guidelines for ship CFD applications. In: 28th International Towing Tank Conference, Recommended Procedures and Guidelines, pp. 1–15.

ITTC, 2017b. 7.5-02-02-01 resistance test. In: 28th International Towing Tank Conference, Recommended Procedures and Guidelines, Procedure 7.5-02-02-01.

ITTC, 2017c. 7.5-01-03-01 uncertainty analysis instrument calibration. In: 28th International Towing Tank Conference, Recommended Procedures and Guidelines, Procedure 7.5-01-03-01.

ITTC, 2014. 7.5-02-02-02.1 example for uncertainty analysis of resistance tests in towing tank. In: 27th International Towing Tank Conference, Recommended Procedures and Guidelines, Procedure 7.5-02-02-02.1.

Jin, S., Peng, H., Heather, Qiu, W., Hunter, R., Thompson, S., 2023. Numerical simulation of planing hull motions in calm water and waves with overset grid. Ocean Engineering 287, 115858. https://doi.org/10.1016/j.oceaneng.2023.115858.

Judge, C., Mousaviraad, M., Stern, F., Lee, E., Fullerton, A., Geiser, J., Schleicher, C., Merrill, C., Weil, C., Morin, J., Jiang, M., Ikeda, C., 2020. Experiments and CFD of a high-speed deep-V planing hull—Part I: calm water. Appl. Ocean Res. 96, 102060. https://doi.org/10.1016/j.apor.2020.102060.

Lakatoš, M., Sahk, T., Andreasson, H., Tabri, K., 2022. The effect of spray rails, chine strips and V-shaped spray interceptors on the performance of low planing high-speed craft in calm water. Appl. Ocean Res. 122, 103131. https://doi.org/10.1016/j.apor.2022.103131.

Larsson, L., Raven, H.C., 2010. The Principles of Naval Architecture Series Ship Resistance and Flow. The Society of Naval Architects and Marine Engineers.

Lee, E., Pavkov, M., McCue-Weil, L., 2014. The systematic variation of step configuration and displacement for a double-step planing craft. Journal of Ship Production and Design 30. https://doi.org/10.5957/jspd.2014.30.2.89.

Lee, E., Weil, C.R., Fullerton, A., NSWCCD, 2017. Experimental Results for the Calm Water Resistance of the Generic Prismatic Planing Hull (GPPH), NSWCCD-80-TR-2017/015, pp. 20817–25700. West Bethesda, MD.

Lee, E.J., Mousaviraad, M., Weil, C.R., Jiang, M.J., Fullerton, A.M., Stern, F., 2021. Assessment of experiments and CFD for the semi-planing R/V Athena Model in calm water. Ocean Engineering 236. https://doi.org/10.1016/j.oceaneng.2021.109254.

Lee, Y.G., Kim, C., Park, J.H., Kim, H., Lee, I., Jin, B., 2019. Numerical simulations of added resistance in regular head waves on a container ship. Brodogradnja 70. https://doi.org/10.21278/BROD70204.

Li, J., Bonfiglio, L., Brizzolara, S., 2019. Verification and validation study of OpenFOAM on the generic prismatic planing hull form. In: 8th International Conference on Computational Methods in Marine Engineering. MARINE 2019.

Mancini, S., De Luca, F., Ramolini, A., 2017. Towards CFD guidelines for planing hull simulations based on the Naples Systematic Series. In: 7th International Conference on Computational Methods in Marine Engineering. MARINE 2017.

Molchanov, B., Lundmark, S., Fürth, M., Green, M., 2019. Experimental validation of spray deflectors for high speed craft. Ocean Engineering 191, 106482. https://doi.org/10.1016/j.oceaneng.2019.106482.

Mousaviraad, S.M., Wang, Z., Stern, F., 2015. URANS studies of hydrodynamic performance and slamming loads on high-speed planing hulls in calm water and waves for deep and shallow conditions. Appl. Ocean Res. 51, 222–240. https://doi.org/10.1016/j.apor.2015.04.007.

Müller-Graf, B., 1991. The effect of an advanced spray rail system on resistance and development of spray of semi-displacement round bilge hulls. In: Holden, K.O., Faltinsen, O.M., Moan, T. (Eds.), FAST '91, 1st Intl Conf on Fast Sea Transportation. Tapir Publishers, Trondheim, Norway, pp. 125–141.

Niazmand Bilandi, R., Dashtimanesh, A., Mancini, S., Vitiello, L., 2023. Comparative study of experimental and CFD results for stepped planing hulls. Ocean Engineering 280. https://doi.org/10.1016/j.oceaneng.2023.114887.

Niazmand Bilandi, R., Dashtimanesh, A., Tavakoli, S., 2020. Hydrodynamic study of heeled double-stepped planing hulls using CFD and 2D+T method. Ocean Engineering 196, 106813. https://doi.org/10.1016/j.oceaneng.2019.106813.

Niazmand Bilandi, R., Dashtimanesh, A., Tavakoli, S., 2019. Development of a 2D+T theory for performance prediction of double-stepped planing hulls in calm water. Proc. IME M J. Eng. Marit. Environ. 233, 886–904. https://doi.org/10.1177/1475090218797784.

Niazmand Bilandi, R., Mancini, S., Dashtimanesh, A., Tavakoli, S., 2024a. A revisited verification and validation analysis for URANS simulation of planing hulls in calm water. Ocean Engineering 293, 116589. https://doi.org/10.1016/J.OCEANENG.2023.116589.

Niazmand Bilandi, R., Tavakoli, S., Mancini, S., Dashtimanesh, A., 2024b. Dynamic motion analysis of stepless and stepped planing hulls in random waves: a CFD model perspective. Appl. Ocean Res. 149, 104046. https://doi.org/10.1016/J.APOR.2024.104046.

Nimmagadda, N.V.R., Polisetty, L.R., Vaidyanatha Iyer, A.S., 2020. Simulation of air–water interface effects for high-speed planing hull. J. Mar. Sci. Appl. 19. https://doi.org/10.1007/s11804-020-00172-0.

O'Shea, T.T., Brucker, K.A., Wyatt, D., Fu, T.C., Dommermuth, D.G., 2012. A detailed validation of numerical flow analysis (NFA) to predict the hydrodynamics of a deep-v planing hull. In: Paper Presented at the SNAME Chesapeake Power Boat Symposium, Annapolis. https://doi.org/10.5957/cpbs-2012-016. Maryland, June 2012.

Roshan, F., Dashtimanesh, A., Niazmand Bilandi, R., 2020. Hydrodynamic characteristics of tunneled planing hulls in calm water. Brodogradnja 71, 19–38. https://doi.org/10.21278/brod71102.

Savitsky, Daniel, 1964. Hydrodynamic Design of Planing Hulls. Mar Technol SNAME N 1 1 (04), 71–95. https://doi.org/10.5957/mt1.1964.1.4.71.

Savitsky, D., DeLorme, M.F., Datla, R., 2007. Inclusion of whisker spray drag in performance prediction method for high-speed planing hulls. Mar. Technol. 44, 35–56.

Savitsky, D., Morabito, M., 2010. Surface wave contours associated with the forebody wake of stepped planing hulls. Mar. Technol. 47. https://doi.org/10.5957/mtsn.2010.47.1.1.

Siemens, P.L.M., 2022. Simcenter STAR-CCM+ 2210 Build 17.06.007 User Guide.

Stern, F., Wilson, R.V., Coleman, H.W., Paterson, E.G., 2001. Comprehensive approach to verification and validation of CFD simulations—Part 1: Methodology and procedures. J. Fluid Eng., Trans. ASME 123, 793–802. https://doi.org/10.1115/1.1412235.

Stern, F., Wilson, R., Shao, J., 2006. Quantitative V&V of CFD simulations and certification of CFD codes. Int J Numer Methods Fluids 50, 1335–1355. https://doi.org/10.1002/fld.1090.

Sukas, O.F., Kinaci, O.K., Cakici, F., Gokce, M.K., 2017. Hydrodynamic assessment of planing hulls using overset grids. Appl. Ocean Res. 65, 35–46. https://doi.org/10.1016/j.apor.2017.03.015.

Taunton, D.J., Hudson, D.A., Shenoi, R.A., 2010. Characteristics of A series of high speed hard chine planing hulls - Part 1: performance in calm water. International Journal

of Small Craft Technology 152, 55–75. https://doi.org/10.3940/rina.ijsct.2010.b2.96.

Tavakoli, S., Zhang, M., Kondratenko, A.A., Hirdaris, S., 2024. A review on the hydrodynamics of planing hulls. Ocean Engineering. https://doi.org/10.1016/j.oceaneng.2024.117046.

Terziev, M., Tezdogan, T., Incecik, A., 2020. Application of eddy-viscosity turbulence models to problems in ship hydrodynamics. Ships Offshore Struct. 15. https://doi.org/10.1080/17445302.2019.1661625.

Viola, I.M., Flay, R.G.J., Ponzini, R., 2012. CFD Analysis of the Hydrodynamic Performance of Two Candidate America's Cup AC33 Hulls, vol. 154. Transactions of the Royal Institution of Naval Architects Part B: International Journal of Small Craft Technology. https://doi.org/10.3940/rina.ijsct.2012.b1.113.

Vitiello, L., Mancini, S., Niazmand Bilandi, R., Dashtimanesh, A., De Luca, F., Nappo, V., 2022. A comprehensive stepped planing hull systematic series: Part 1 - resistance test. Ocean Engineering 266, 112242. https://doi.org/10.1016/J.OCEANENG.2022.112242.

Wei, C., Li, Y., Liang, X., Yi, H., 2019. Hull forms of small high-speed wave-piercing monohull crafts and hydrodynamics study. J. Hydrodyn. 31, 814–826. https://doi.org/10.1007/S42241-018-0173-8/METRICS.

Wheeler, M.P., Ryan, P., Cimolin, F., 2021. Using VOF slip velocity to improve productivity of planing hull CFD simulations. In: SNAME International Conference on Fast Sea Transportation 2021, pp. 26–27. https://doi.org/10.5957/FAST-2021-013. FAST 2021.

Wilson, R., Shao, J., Stern, F., 2004. Discussion: criticisms of the "correction factor" verification method [1]. Journal of Fluids Engineering, Transactions of the ASME 126, 704–706. https://doi.org/10.1115/1.1780171.

Wilson, R.V., Carrica, P.M., Stern, F., 2006. Unsteady RANS method for ship motions with application to roll for a surface combatant. Comput. Fluids 35, 501–524. https://doi.org/10.1016/j.compfluid.2004.12.005.

Curriculum vitae

Personal data

Name:	Mikloš Lakatoš ETIS, ORCID, Scopus
Date of birth:	10.09.1986
Place of birth:	Narva
Citizenship:	Estonian

Contact data

E-mail:	miklos.lakatos@taltech.ee

Education

2017–2026	Tallinn University of Technology, School of Engineering, Environmental and coastal engineering, PhD
2009–2013	Aalto University, School of Engineering, Mechanical engineering, MSc
2009–2013	Tallinn University of Technology, Faculty of Mechanical Engineering, Product development and Production Engineering, MSc
2006–2009	Tallinn University of Technology, Faculty of Mechanical Engineering, Product development and Production Engineering, BSc
2003–2006	Tallinn School No. 21, High school

Language competence

Estonian	Native
Russian	Native
Hungarian	Basic
English	Fluent
German	Fluent
Italian	Fluent
Spanish	Basic
Finnish	Basic

Professional employment

2026 –	Tallinn University of Technology, Kuressaare College, specialist
2024 – 2026	Hamburg Ship Model Basin (HSVA), project manager/ researcher ships
2022 – 2024	Tallinn University of Technology, Kuressaare College, engineer
2017 – 2021	Tallinn University of Technology, Kuressaare College, early stage researcher
2013 – 2017	Deltamarin Ltd, hydrodynamics, concept development
2012 – 2013	Deltamarin Ltd, master's thesis worker
2011	Deltamarin Ltd, trainee, hydrodynamics
2010	TKK Ship Laboratory, research assistant
2008	BLRT IK, trainee (designer/ draftsman)

Elulookirjeldus

Isikuandmed

Nimi:	Mikloš Lakatoš ETIS, ORCID, Scopus
Sünniaeg:	10.09.1986
Sünnikoht:	Narva
Kodakondsus:	Eesti

Kontaktandmed

E-post:	miklos.lakatos@taltech.ee

Hariduskäik

2017 – 2026	Tallinna Tehnikaülikool, Inseneriteaduskond, Keskkonna ja rannikutehnika, PhD
2009 – 2013	Aalto Ülikool, Inseneriteaduskond, Mehaanikatehnika, MSC
2009 – 2013	Tallinna Tehnikaülikool, Mehaanika teaduskond, Tootearendus ja Tootmistehnika, MSc
2006 – 2009	Tallinna Tehnikaülikool, Mehaanika teaduskond, Tootearendus ja Tootmistehnika, BSc
2003 – 2006	Tallinna 21. Kool, Keskharidus

Keelteoskus

Eesti keel	Kõrgtase
Vene keel	Kõrgtase
Ungari keel	Algtase
Inglise keel	Kõrgtase
Saksa keel	Kõrgtase
Itaalia keel	Kesktase
Hispaania keel	Algtase
Soome keel	Algtase

Teenistuskäik

2026 –	Tallinna Tehnikaülikool, Kuressaare kolledž, spetsialist
2024 – 2026	Hamburgi Laeva katsebassein (HSVA), projektijuht/ teadur
2022 – 2024	Tallinna Tehnikaülikool, Kuressaare kolledž, insener
2017 – 2021	Tallinna Tehnikaülikool, Kuressaare kolledž, doktorant-nooremteadur
2013 – 2017	Deltamarin Ltd, hüdrodünaamika spetsialist
2012 – 2013	Deltamarin Ltd, magistritöö kirjutaja, hüdrodünaamika
2011	Deltamarin Ltd, praktikant, hüdrodünaamika
2010	TKK Laeva labor, assistent
2008	BLRT IK, praktikant (projekteerija)

ISSN 2585-6901
ISBN 978-9916-80-586-2